Fabrication and characterisation of chemical vapour deposition grown branched carbon nanotube arrays.
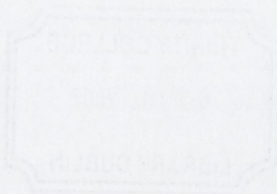
By

Rory Leahy

A thesis submitted for the degree of
Doctor of Philosophy
in the
University of Dublin

School of Physics
Trinity College Dublin

October 2006
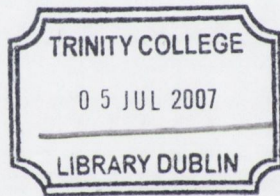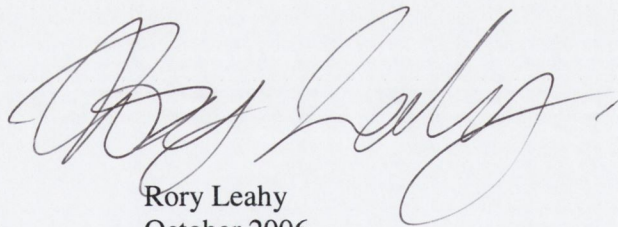
Declaration

I declare that the work in this thesis has not been previously submitted as an exercise for a degree to this or any other university.

The work described herein is entirely my own, except for the assistance mentioned in the acknowledgements and the collaborative work mentioned in the list of publications.

I agree that Trinity College Library may lend or copy this thesis on request.

Rory Leahy
October 2006

"Anyone who lives within their means suffers from a lack of imagination."

Oscar Wilde

"I am in blood
Stepp'd in so far that, should I wade no more,
Returning were as tedious as go o'er."

Macbeth.
ACT III, Scene IV.

Acknowledgements

Chris Murray for their advice and support and Matt Shaw, who provided me the test-chips which proved integral to my research.

Right, I believe that is all the official stuff out of the way. Now it is time to thank all those other eejits I have had the pleasure and/or misfortune of bumping into on my epic voyage to doctorhood (I hope).

My fellow Ramanites: Matt, Harmeet and Kaushik, the original four. I shall not soon forget our time together in the trenches. Once I get New York City back, I'll come and visit again. I guess I should also give a shout out to the Johns: Ward and Nugget, Mike (I hope you're still writing math on people's phone bills), Ray Dove (any dram of skill in microscopy I possess is mostly your fault), Nancy and all the other staff and students in the materials dept.

While I am still on America, I would like to thank Jennybird, Dan and Melissa "stress-bomb" Koonz: my co-inhabitants of the little yellow apartment. Though you were not strictly part of my PhD, you did keep me sane, which deserves at least a mention. Who wants to go to Wal*Mart?

Since my tour of duty is bested in longevity only by the mighty Strevens (and no better shoulders to support such an honour), I will undoubtedly miss out somebody during my roll-call of group BU members past and present. If I missed you out, please know it is because I never liked you and any niceties that passed between us were a hideous lie. The old guard first: Cats (who would have thought a girl in cow print trousers could go so far), Sandy, Rob, O'Flama, Bernd, Slipper, Manuel, Gavin, Bernd, Grace, Kevin (I'll meet you in the gym this Tuesday, honest), Take, Bernd, Gordon, Steffi (I loved you from afar), Anna, Margaret and Patrick, and of course, Bernd. The fresh faces: Ronan, Paula, Trevor (you know, I always sing the Bisto song in my head when I hear your name), Scurvy Bergin (Haaarrrr), Yenny (coffee and procrastination? Threeish?) Princess Fiona (I'll be coming after your oatlettes), Niall and Darren (group BU's answer to Ant and Dec, I think you guys were more help to me than I've been to you, so cheers), Helen Cathode, David Jean Claude van Blond, Éimhín (See! if I can do it, so can you), Sharon, Umar, Chris (your undentable optimism is contagious), Silvia, Les, Valeria (I'd make a joke about lemons, but I'm not that kind of guy), Richard, The Jango, and Emer. I also thank the assorted minions and underlings who passed through, especially the cute ones. Jimmy Doyle, I swear I will definitely hand this in probably sometime next weekish, most likely. Of course, my reputation within the group would not be what it is without thanking ⚲ℳ■⧓s!

Thank you to my proof-readers: Niall, Darren, Donal, Ciara, Emer, Éimhín, Yenny and Smidget.

My ordeal has been made more tolerable by the following institutions: coffee, www.phdcomics.com (you are not alone), the glorious interweb, my feisty little laptop (awesomeness in a box, with a wobbly screen and banjaxed DVD player as bonus features), NPR, Lexipro, podcasts, coffee, Metro café, coffee breaks, weasels, picnics, my green shoes, huppah, and did I mention coffee?

I would like to take this opportunity to specifically **not** thank a few things and people: Christian Nitschke (you and your little cactus too), stress, all things ursine, twitches, the blue screen of death, equipment lead times of more than two weeks, losing pens, the treacherous gods of science, and the seductive lure of procrastination. I also blow a very loud and wet raspberry at all those who believed that I would never actually get to this point but rather remain a student until the end of time. You know who you are!

I would like to thank my non-science friends for their support, and mostly for not taunting me too much for still being a student while ye are all out earning sacks of cash. You are too many to mention, but tH are too arrogant to leave out: Brian, Don, Leo, Mike and Alan (Word to my homeSlice), you have an been amazing help to me during some very difficult times. You guys are super-geil.

I would to thank Lorna with her very own dedicated paragraph. You have helped me more than any other person during the course of my PhD. You have kept me calm when I've been running deadlines, and my sanity to their very crust. You have given me hope when I was about to throw in the towel and go live in a box, and you've given me perspective when I've been lost in the woods. You are my best friend, and I trust your judgement when I do not trust my own. I guess what I am saying is: you're not too bad.

Finally mine kline folks: Deirdre (dearest Mudder your warbling rendition of "I'm nobody's child, shall forever haunt me), Dave (who him peeping in at me?), and Eoin (shrimpy?): you have always been there to support me and too look out for what is best for me.

XI

Abstract

The fabrication, optimisation and characterisation of arrays of straight and junction multiwall carbon nanotubes (MWNTs) is presented in this thesis. A detailed description of the design and fabrication of the chemical vapour deposition (CVD) system used for their production is presented. Various carbon nanotube (CNT) geometries produced during the optimisation of the CVD parameters, such as mats, vertically aligned forests and long CNTs are presented and discussed.

SEM, EDX and Raman spectroscopy analyses on CNTs grown on metal filled mesoporous alumina substrates are presented. These show that MWNTs tend to grow on the substrate where the metal rises and pools on the surface during heating in the CVD chamber. Similar analysis is used to demonstrate the successful growth of CNTs using an aqueous solution of Fe_2SO_4.

The central line of investigation of this thesis was the production of arrays of straight and branched CNTs. Alignment of the arrays arises from the self-positioning properties of the catalyst solution resulting in the deposition of iron catalyst at the trench edges. The arrays can be formed such that the CNTs bridge trenches etched into a Si substrate. In this manner, the alignment and length of the CNTs can be controlled through selection of trench geometry.

A systematic study of CVD conditions was undertaken in order to optimise the overall array density and proportion of junction-structure CNTs. The initial conditions: trench width, C_2H_2 flow rate, C_2H_2 flow time, catalyst solution concentration; and reaction temperature were each measured and changed sequentially over a number of experiments. The resulting CNT arrays were examined using SEM and Raman spectroscopy.

The study revealed that temperature and trench-width have the most profound affect on array density and makeup. Decreasing temperature leads to an increase both in the overall array density and the percentage of branched CNTs. Array density is seen to increase with decreasing trench width while the percentage of junction-structures remains unaffected. The study yielded arrays with densities of up to 1.6 interconnects per micron of trench with junction-structures accounting for up to 38 % of these interconnects.

Raman spectroscopy revealed that the relative amount of sp^3 bonding present in the array samples is greater the higher the proportion of junction-structures present. This finding supports a junction formation mechanism based on a tip growth model for tube growth in an environment conducive to the formation of kinks.

Junction-structures were removed from their original substrates and placed on substrates pre-patterned with gold contact pads. The CNTs were connected to the pads with gold lines deposited by e-beam lithography. Two individual junction-structure CNT devices were successfully isolated, contacted to conducting probes and electrically characterised.

Two- and four- probe measurements yielded resistances in the region 200 kΩ for straight sections of the stem and branches. Resistances across the junction were much larger, in the region of hundreds of MΩ. I-V plots across the junction in a variety of arrangements yield Ohmic responses. This suggests that all branches of the junction have metallic chirality.

The optimised production of branched Ohmic conductors in aligned arrays of controllable size and density opens up the possibility of integration into a nano-electronic system as interconnects between logic devices.

Table of Contents

Table of Figures

Chapter 1 Introduction

1.1 Scientific Background

The term, "nanotechnology" was first introduced by Professor Norio Taniguchi at the International Conference in Engineering held in Tokyo in 1974, in a paper called "The basic concepts of Nano-technology". He used the term to set a definite target-accuracy for fabrication processes, which involve ultra-precision surface finishing such as ultra-fine mirror turning, thin film evaporation and ultra-fine etching.

Nowadays the technologies that can be accompanied by the prefix "nano" can be split into at least 5 different groups:

1. Classical "top-down" technologies miniaturised to nanometer scale, used in the semiconductor industry, quantum devices and many communications technologies.
2. "Bottom-up" technologies involving manipulations at an atomic and molecular level.
3. Materials science using materials with nano scaled structure.
4. Micro machines or Micro Electronic Machine Systems (MEMS), that themselves are on a micron scale but have nm scale components.
5. Basic science and technology on nm scale, for example quantum theory and measurement technology.

However, some of the most exciting progress is being made in the juxtaposition of top-down and bottom-up technologies, and these are the technologies with which we will most concern ourselves here. Top-down fabrication is the miniaturisation of current technologies usually achieved by removing or etching material from larger features and components.

Nowadays nanometer precision is within the routine precision limits for many processes, notably in the semiconductor industry and this precision is being continually improved upon. The fabrication of nanoscale components from bulk materials (namely silicon) has been dubbed top-down manufacturing. Ion beam milling and photolithography are examples of top-down fabrication methods that can produce feature sizes in the order of a few nanometers. Though developments of this nature will increase precision and efficiency and help industry in its addictive obsession with adhering to Moore's law (Figure 1-1), it seems unlikely that any novel or break-through advances will arise from this approach. It is the advances being made from the other end of the scale that are causing much more excitement.
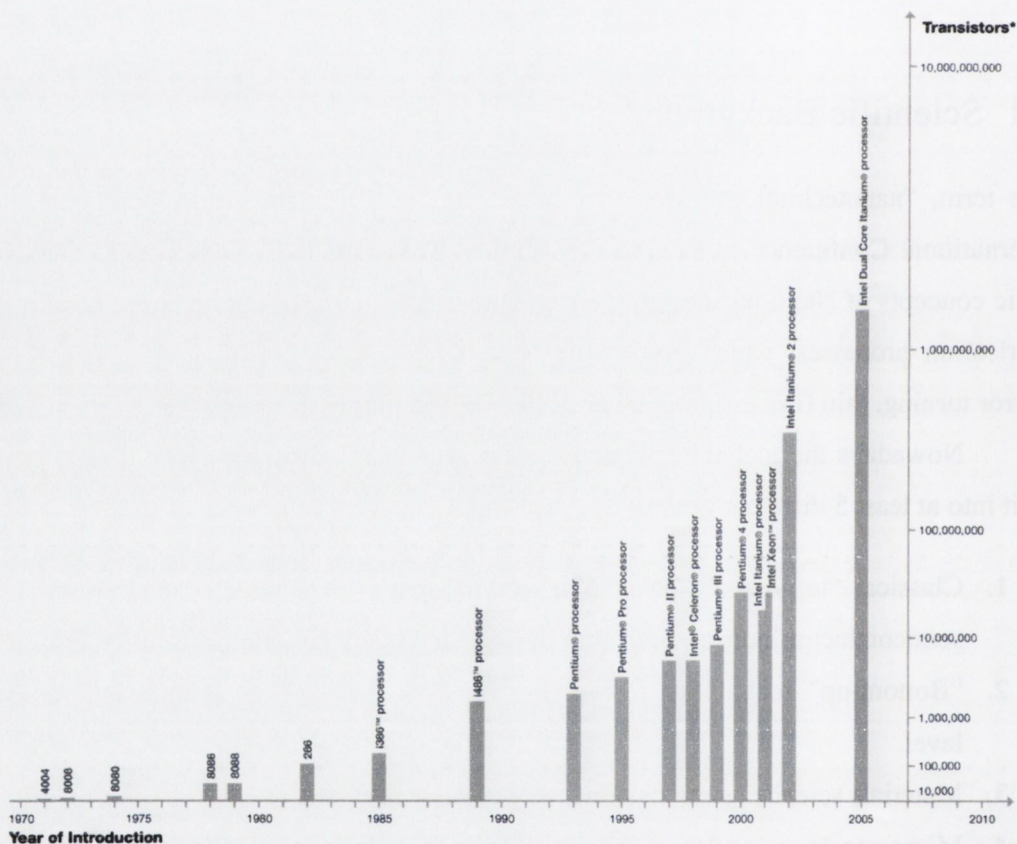
Figure 1-1 Moore's law shown in terms of number of transistors on an Intel chip. As the transistor number increases their size must similarly decrease.

The idea of bottom-up manufacturing was first proposed by physicist, Nobel laureate and bongo player Richard Feynman over 40 years ago. While top-down manufacturing requires the reduction in size of a larger component, bottom up fabrication, builds up from an atomic or molecular level to provide the new feature; literally creating devices atom by atom.

Bottom up techniques are based on principles such as self-assembly and self-organisation. One of the most common applications of these principles is to easily produce monolayers using techniques such as physical vapour deposition (PVD), atomic layer epitaxy (ALE) and chemical vapour deposition (CVD).

The idea of custom built materials and devices with novel functions and superior characteristics made possible by bottom-up techniques is very attractive, but as always in life, things are never that easy and several problems exist.

The first and most obvious hurdle is the sheer logistics of the complex chemistry involved in making a functional block; say something analogous to current silicon based logic circuits. This, coupled with other factors such as the problem that many quantum devices only work in very low temperature environments, makes the idea of mass production an engineering nightmare.

Reliability and reproducibility are still huge hurdles to overcome if nanotechnology is to reach the level of knowledge and controllability that exists in the semiconductor industry. There is hope however, that much can be borrowed from this more mature science such as the developed but mostly discarded techniques to increase defect tolerances in logic circuits.

The concept of nanotechnology has recently risen to the level of buzzword due to many factors including the discovery of new and novel materials such as fullerenes and carbon nanotubes. Already commercial chips have feature sizes of the order of tens of nanometers, soon quantum leaking and other scaling factors will prevent the further miniaturisation of current Si technology.

One possibility to enable CMOS architecture to continue its journey down the rabbit hole that is Moore's law is to incorporate new materials into it, one of the main prospects being carbon nanotubes (CNTs). CNTs have been suggested as being ideal candidates for integration into current CMOS circuitry due to their small diameter, high aspect ratio and novel conduction properties allowing them the possibility of functioning both as interconnects and devices such as diodes, transistors, and high frequency devices.

1.2 Thesis outline

This thesis will explore the fabrication of the integration of CNT arrays, specifically branched multiwalled carbon nanotube (MWNTs). Chapter 2 outlines the current state of research as published in the literature, with a focus on the growth of branched CNT structures.

Chapter 3 discusses the experimental methods employed in this thesis. This chapter is divided into two main sections. The first describes the methods used to synthesise the CNTs, covering choice of substrates, catalyst placement and CVD treatment. Section 3.2 section covers the various microscopic and spectroscopic methods used to characterise the CNTs.

Chapter 4 deals with the design and building of a CVD system. The basic concepts of CVD, as well as its specific advantages and uses in industry will be covered in Sections 4.2 – 4.4. Section 4.5 covers in detail the design of and individual components used to build the CVD.

Chapter 5 discusses the various CNT geometries grown in the custom made CVD. Section 5.1 covers long tubes and forests of CNTs. The next section describes experiments with growing CNTs on mesoporous silica. Growth with an alternative catalyst delivery system and treatment of pre-grown CNTs are covered in the subsequent sections.

Chapter 6 discusses the growth of arrays of junction structured CNTs covering initial growth of junctions. The systematic study of the effects of initial CVD growth conditions and possible growth mechanism for the formation of the arrays is presented.

Chapter 7 presents the electrical characterisation of Y-junction CNTs. Results of a conducting probe AFM study demonstrate conduction in all branches. Section 7.5 discusses the characterisation of two individual junction-structure CNTs via two and four probe resistance measurements.

Finally, Chapter 8 concludes this thesis, by reviewing the research presented here.

Chapter 2 Experimental background and literature review

2.1 Introduction

This chapter aims to provide an overview of the current state of research of the applications of carbon nanotubes (CNTs) with particular emphasis on junction-structure CNTs and suspended CNTs. Knowledge of the basic characteristics and properties of Carbon nanotubes is assumed for this chapter. These properties are covered in great detail in a variety of books,[1-3] publications [4-13] and websites.[14, 15]

While CNTs can be used for a wide variety of applications such as chemical sensors (see Appendix A), this chapter will cover topics relevant to the work done in this thesis. Section 2.2 will give an overview of CNTs used for nano-electronics applications. Section 2.3 will cover the various methods used to align CVD grown CNTs. The production and application of suspended and bridging CNTs are covered in Section 2.4. Branched CNTs shall be covered in detail in Section 2.5. This section is broken into three subsections covering: fabrication; growth mechanisms of branched CNTs, and finally their possible applications. Section 2.5 overviews the application of Raman spectroscopy to CNT research.

2.2 Basic conduction properties of CNTs

The electrical properties of CNTs are linked to those of graphite, or more specifically those of individual graphene sheets. The band structure of graphene has conducting states at the Fermi energy level, but only at specific points along certain directions in reciprocal space,

namely at the corners of the first Brillouin Zone. It is known as a zero band gap semiconductor that has an electronic structure near the Fermi energy consisting of an occupied π band and an empty π^* band. When this sheet is rolled into a tube the curvature of the matrix means that only a certain set of k states of a flat graphene sheet is allowed. At the K-point the density of states at the Fermi level is non-vanishing, therefore any CNT whose set of allowed k values includes the K-point will be metallic in nature. The set of allowed k values depends on the diameter and helicity of the tube. When the K-point is not included, the CNT is a semiconductor.

The states near the Fermi energy in both metallic and semiconducting CNTs are all from k values near the K-point, so their transport properties are related to the properties of the states on the allowed lines. For example, the conduction band and valence bands of a semiconducting tube come from states along the line closest to the K-point.

The different ways in which the graphene is rolled to form a CNT can be specified by its circumferential periodicity.[16] The geometry of a SWNT is completely specified by a pair of integers (n, m) denoting the relative position $c = na_1 + ma_2$ of the pair of atoms on a graphene strip which point into the tube.

Three types of single wall nanotube are possible: armchair, zigzag and chiral nanotubes, which differ in the angle at which the two-dimensional graphene sheet is rolled up and wrapped around onto itself.[17]

For zigzag CNTs, the rows of carbons in the lattice are perpendicular to its axis. Such CNTs are described by chiral vectors of the form (n, 0), and are semiconducting. Armchair CNTs, however, have (n, n) form chiral vectors so that the carbon rows lie parallel to its axis. Armchair CNTs are always metallic.

All other forms of wrapping are referred to as chiral nanotubes. CNTs described by (n, m) where n - m = 3j, where j is a nonzero integer, are very tiny-gap semiconductors; others are large gap semiconductors.

As the tube radius R increases, the band gaps of the large-gap and tiny-gap varieties decreases with a 1/R and $1/R^2$ dependence, respectively. Thus, for most experimentally observed carbon nanotube sizes, the gap in the tiny-gap variety which arises from curvature effects would be so small that, for most practical purposes, all the n - m = 3j tubes can be considered as metallic at room temperature.

2.3 Advances in CNT nano-electronics

As in previous years there has been much work towards fabrication of working CNT electronic devices[18-20] such as Schottky barrier transistors[21] and carbon nanotube-field effect transistors (CNT-FETs)[22, 23] (Figure 2-1).

One of the most exciting developments taking place is the push towards wafer scale production of devices led by Honjie Dai's group in Stanford.[22, 23] In 2001 the group succeeded in successfully growing high quality SWNTs evenly over an entire 4-inch wafer using chemical vapour deposition (CVD) with a carefully balanced mix of methane and hydrogen as the carbon feedstock.[24] The group have also managed to reproducibly mass fabricate CNT atomic force microscopy (AFM) tips on a 4-inch wafer by a similar CVD method. They report reproducible growth of SWNTs on approximately 90% of 375 Si AFM tips on a wafer.

The group have been at the forefront of the race to create viable and integratable CNT devices; recently it has reported building logic gates from CNT-FETs[23] with a yield of ~ 20 – 30 devices from 100 on a 4mm x 4mm chip. Unlike the majority of previous CNT-FET studies[22, 25] which have a common back gate (and hence all devices are switched on or off simultaneously) each device in this study can be operated individually.

Though all the devices grown in this method are p-type, devices can be selectively converted to n-type by applying a high local gate voltage combined with a large source-drain bias under vacuum. This drives off adsorbed oxygen resulting in increased n-channel conduction. However, once re-exposed to ambient conditions all devices return to p-type characteristics, so that all device measurements had to be carried out under ultra-high vacuum (UHV). Derycke et al coated the n-type devices in PMMA to prevent oxygen re-adsorption,[22] which was successful up to pressures of $\sim 10^{-2}$ Torr, but the devices still revert to p-type in ambient conditions. By linking these devices together by simple wire bonding techniques they have been able to create multi-stage logic gates such as NOT, AND, OR, NAND, and NOR gates[26] (Figure 2-1).

Wind et al[27, 28] have also successfully fabricated CN-FETs; however as opposed to a back-gate they have opted for the approach of using a buried CNT with a top gate. Embedding the n-type devices in the gate insulator protects them from readsorption. The fact that they are buried in the gate insulator also allows full advantage to be taken of the gate dielectric. In the case of exposed tube CNT-FETs the gate insulator capacitance is diluted by the lower dielectric constant of air. Also, unlike the back-gated devices which have too large an overlap capacitance between the gate, source and drain, top-gate devices

are suited to high frequency operation. These top-gate CNT-FETs show excellent turn on and saturation at gate voltages ~1V. The maximum transconductance is 3.25 μS, which is an extremely high value for a CN-FET device compared to previously reported CNT-FETs.[29] These CNT-FETs are capable of ~3 - 4 times higher drive current per unit width than the Si *p*-type metal-oxide field effect transistors (MOSFETs) at a gate overdrive of around 1V, with approximately 2 - 4 times higher transconductance.[29, 30] The authors note that the channel length and gate oxide thickness are significantly larger for the top-gate CNT-FET than for the Si devices. They feel that through tailoring the gate-channel capacitance by controlling the gate dielectric thickness and the raising the dielectric constant, coupled with reducing the gate length further improvements to device performance can be achieved.[31, 13, 32]
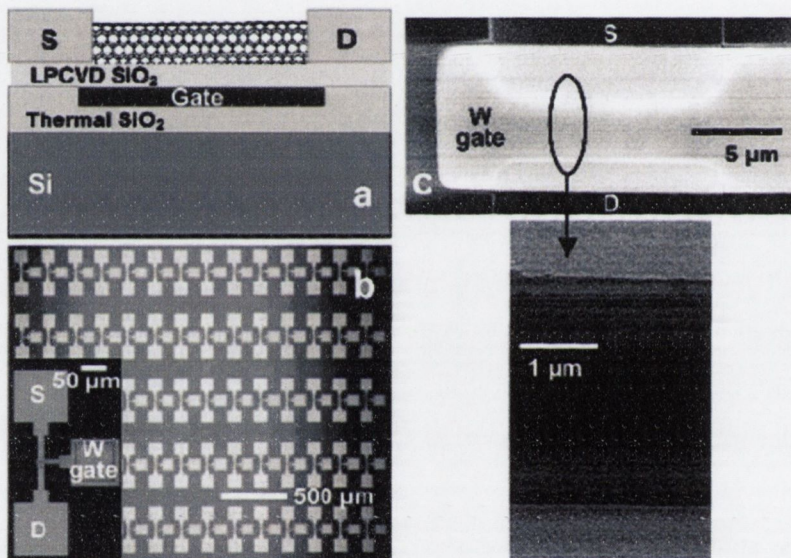
Figure 2-1 Set of SEM micrographs showing patterned growth and integration for arrays of nanotube transistors with local bottom gates. (a) Schematic side view of a SWNT-FET with a W local gate embedded in the SiO₂ substrate. The source (S) and drain (D) electrodes (distance between the edges of S and D = 3μm) are made of Mo, fabricated prior to catalyst patterning and CVD growth. The length of the embedded W gate is 7 μm, overlapping with S and D by ~2 μm. (b) an optical image of an array of locally gated SWNT-FETs. Inset: A zoom-in optical image showing details of a SWNT-FET with W bottom gate. (c) A scanning electron microscopy (SEM) image of a SWNT-FET with bottom W gate. The W gate area appears bright due to charging in the SEM (the gate electrode is buried underneath a 200 nm insulating SiO₂ layer).[22]

2.4 Alignment

Over the last few years one of most active research areas for CNTs has been aligned growth.[33-47] It is only in very recent times, that this area has given way to the more refined specialisation of in situ grown CNT devices.

Choi and colleges[41] have reported growth of vertically aligned CNTs with diameters up to 200 nm, using CVD of acetylene at temperatures of ~800-900°C for short run times (~5 – 20 minutes). They found that the diameters of the CNTs produced are directly related to the domain size of the catalyst particles.

Wei et al[42] have noted that cracks formed in a 15.3 nm nickel (Ni) layer allow the xylene/ferrocene during CVD to reach the SiO_2 layer below. Once the underlying SiO_2 layer has a constant supply of catalyst and carbon feedstock MWNTs can grow up from under the Ni layer pushing a circular cap of Ni out of the surface layer. These MWNT pillars have diameters that range from 10 to 100μm containing thousands of MWNTs. The heights of the pillars are of the order of several tens of microns. Pillars over 100μm long have been recorded, though most are seen to have toppled over, causing further cracking in the Ni layer. The authors are unsure as to the mechanism of the circular cracks in the Ni layer, though they feel that it may be related to the interaction of the Ni layer with the Fe catalyst. This suggestion is made in light of the discovery of a Ni depletion region around the cracks recorded with energy dispersive x-ray spectroscopy (EDS).

One method for growing in situ aligned CNTs is through the application of porous alumina membranes (PAMs).[48-66] Zhang et al report high density CNT arrays with densities up to $10^{12} cm^{-2}$ [63]. They produced MWNT in the pores of PAM substrates during CVD of 10% C_2H_2 in N_2 flowed at 80 sccm at temperatures between 600 and 700°C. The template before CVD had 22nm channels, though a TEM investigation after CVD gives MWNT diameter of ~25nm, this is possibly due to thermal expansion of the substrate during CVD. A Raman investigation of CNTs produced at 600°C gave a G-band at 1610 cm^{-1}, which suggests that the CNT may have an amorphous carbon coating. Raman on CNTs grown at 700°C has a down-shifted G-band at 1580 cm^{-1}, suggesting a much higher degree of crystallinity within the tubes.

Hornyak et al carried out CVD of propylene on PAM substrates[53] and found that the quality (i.e. the graphitic nature) of the produced CNTs improved with increasing temperature from 500 to 800°C. They report CNT diameters of ~30 nm with lengths up to ~200 μm.

Sui et al report that PAMs can act as both template and catalyst for CNT growth[50] during CVD of 9:1 nitrogen/acetylene mix at low flow rates and temperatures (100 sccm at 550 to 550°C). The group suggest that the template can act as catalyst due to metal anions incorporated during the PAM preparation. The walls of the PAM channels are made up of two layers, the inner layer being pure alumina while the outer layer contains large amounts of impurities.

While grown alignment of CNTs is predominantly achieved through substrate patterning, it has been shown that additional alignment can be achieved through the application of electric fields[67, 68] and increased flow rate.[69] Zhang et al[54] report growth of SWNTs across a trench arrangement. The tubes show directional enhancement with applied electric fields of ~0.5 to 2 V/μm (bias voltage of ~10 – 200 V). Fields above ~3 V/μm are seen to cause arcing between the metal contacts during the CVD procedure. Plasma enhanced CVD (PECVD) has been shown to generally give better alignment due to the inherent electrical field present during the growth of the CNTs.[46, 70]

Other novel methods of CNT alignment involve the use of laminar gas flow within the CVD chamber to grow straight ultralong tubes aligned with the direction of gas flow.[71-76]

2.5 Suspended nanotubes

One of the most exciting breakthroughs of the last few years has been the reliable fabrication of suspended CNT arrays.[68, 76-81] Dai and co-workers[69] published the first reports of such structures in June 2000. The growth conditions were an advancement of previously developed CVD techniques.[45, 82] The group report growth of elaborate SWNT networks across the tops of catalyst topped silicon pillars. The SWNTs only grow from the Fe enriched alumina catalyst that is carefully deposited on the caps of the Si pillars. The SWNTs do not stick to the "floor" of the substrate since the gas flow at the bottom of the pillars is substantially less than that at the top. Instead, aided by the fast flow rate of ~1000 sccm of methane (which in conjunction with short flow times of ~20 minutes produces high quality tubes with minimum amorphous carbon[69]), the tubes wave about in the "wind". Once a waving SWNT comes in contact with another pillar it is held in place by van der Waals forces. Tubes as long as ~150 μm are seen bridging several pillars (Figure 2-2).

Since the publication of this landmark paper there have been several subsequent publications expanding on this work.[83-87]

Marty and co-workers[83] report CVD growth of suspended SWNTs across Co topped Ti fingers for electrical testing. Two and four probe measurements reveal purely ohmic responses at room temperatures, with resistances for individual SWNTs ranging from 1 to 100kΩ.

Franklin et al report a reliable and durable method of fabricating suspended SWNTs with characteristic suitable for integration into workable nano-electronic devices.[85] One major advantage of suspended nanotubes is that they are grown connected so that no further wet chemistry processing steps, which may damage or dislodge the CNTs, are necessary. The molybdenum (Mo) contacts were carefully selected from a variety of possible contact metals. It was found that gold (Au) contacts were not stable enough during CVD temperature. Mo, however, was found to exhibit good electrical conductivity after CVD and allows for ohmic contact with the CNT. The precise nature of the CNT-Mo contact is not known, though the two could be joined by the formation of a metallic carbide bonding at the contact point during the high temperature CVD process.[25]
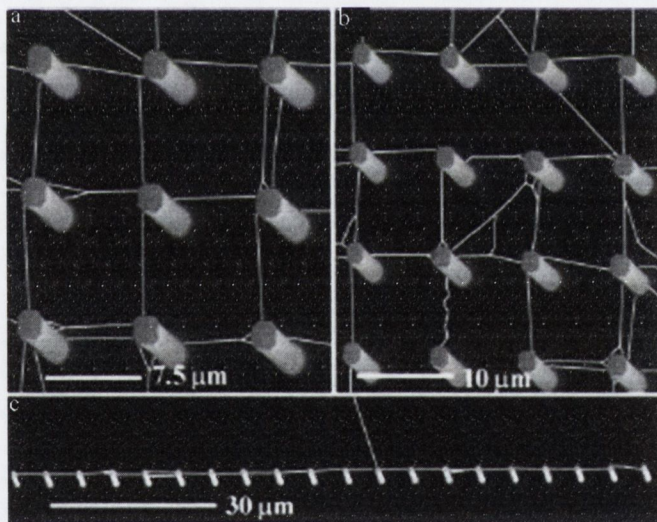
Figure 2-2 A set of SEM micrographs showing: a, b) a network of suspended SWNTs growing from 10 µm silicon pillars. Only longer tubes (> 100 µm) show alignment with flow direction. Shorter tubes are randomly aligned with respect to flow direction; the limiting factor for these tubes is pillar placement and patterning. c) Shows a single long SWNT bridging several pillars. [69]

Tombler et al used SWNTs partially suspended across SiO_2 trenches to test the electrical response of individual CNTs to mechanical bending.[84] They report that pushing on the suspended section of a tube with an AFM tip decreases the electrical conductance. The reversible nature of this interaction suggests that the nanotube/metal AFM tip interaction is not affected, and the change in conductance

is due purely to the mechanical deformation of the tube. Conductance decreased by a factor of 2 at a 5° bending angle, and by 2 orders of magnitude at a bending angle of 14°. Computer simulations[84, 88] suggest that for smaller bending angles the sp^2 bonding remains intact. However, increasing amounts of bond distortion occur about the point of contact with increasing bend angle. At a bending angle of 15° the average number of bonds per atom in the region increases to ~3.6 suggesting sp^3-bonded atoms. This decreases the number of π-electrons, therefore decreasing the conductance. This interaction is also found to be fully reversible on removal of the AFM tip.

2.6 Branched carbon nanotubes

Branched CNT structures such as Y-junctions, 4-way branching and other multi-terminal nanostructures[89-94] have a great potential for use in nano-electronics as rectifiers, switches and tunnel junctions. Such components can be harvested from directly grown CNT junction-structures or created through the functionalisation and interconnection of standard tubes through chemical bonds.[95] The latter method is beyond the scope of this overview. This section will discuss the different methods of production of CNT junction-structures and their possible applications, focusing on their electrical characterisation.

2.6.1 Growth of junction-structure CNTs

Pristine CNTs contain only hexagonal rings of carbon atoms; formation of morphologic structures such as kinks and junctions requires the presence of carbon- pentagons, heptagons, and octagons in the graphitic sheets of the tube. This is essential for maintaining sp^2 configuration for all carbon atoms in order to maximise stability. The topological defects in junction-structures such as Y-junctions obey a generalization of Euler's formula, requiring the presence of such rings to allow for additional curvature similar to that of fullerenes and CNT caps.

Liu et al carried out simulations to predict the effect of defect distribution on Y- and T-junction SWNTs and found that an asymmetric distribution about the junction can have a "shunt" effect leading to the defect loaded branch having lower quantum conductivity. They attribute this to electronic scattering at the defect sites.[96]

A number of computational studies on CNT branched structures have been published to date[97-99] as well as works modelling electrical characteristics such as conductance,[100-103] rectification[104-106] quantum tunnelling,[107] field emission,[108] and

symmetry effects on conductance[109] in junction-structure CNTs. Cummings et al have modelled the thermal properties of CNT Y-junctions and predict that thermal conductivity of a Y-junction carbon nanotube is less than that of a corresponding straight nanotube. They attribute this drop in thermal conductivity to interruption of lattice continuity at the junction acting to impede heat flow by suppressing the density of phonon modes in the system.[110]

Branched CNT structure have been physically created in a variety of ways, such as arc discharge,[111-114] "nanowelding" of straight tubes into various junction structures through irradiation with high powered electron beam[20, 115, 116] and using molecular interlinkers, such as DNA.[95] Branched CNTs have also been created using fullerenes as a starting material through methods of thermal decomposition[117-119] and laser ablation.[120] However, the most common method of preparing branched CNT structures is CVD. The majority of papers published in this area focus on simple thermal CVD[121-132] methods, though several variations such as hot filament CVD,[133-135] plasma enhanced CVD (PECVD)[136, 137] and the pyrolysis of various hydrocarbon species.[138-141]

Deepak et al have grown branched MWNTs with outer diameters between 40 – 60 nm through the pyrolysis of thiophene over nickel nanoparticles dispersed on silica at 1000°C. They showed that in the presence of water vapour, the pyrolysis of organometallic-hydrocarbon mixtures yields SWNTs, as well as narrow MWNTs with Y-junctions[140]. Pyrolysis of organometallic-hydrocarbon mixtures, in the absence of water vapour, only gives nanotubes with T- and Y-junctions (Figure 2-3).
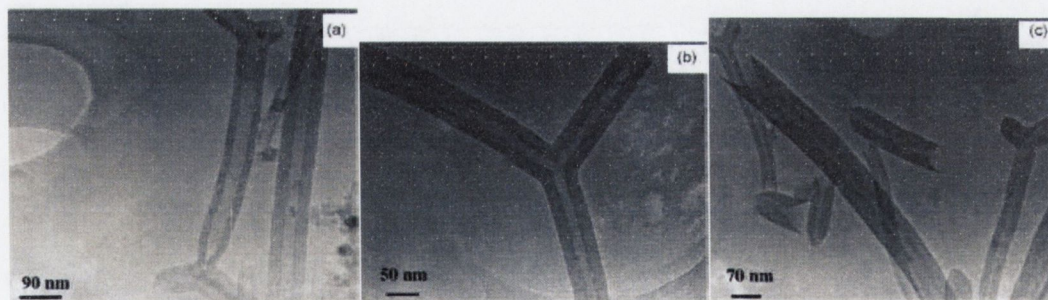
Figure 2-3 TEM images of Y- and T-junctions through the pyrolysis of thiophene over nickel nanoparticles.[140]

Ting et al have used CVD to successfully grown random arrays of branched CNTs on a scratched Si surface.[127, 128] The surface of the substrates were simply roughened with 1000-grit sandpaper to create raised regions as seed points for the subsequent CNTs. Using metal powders such as Fe, FeS, Ni and ferrocene as catalyst precursors under a flow of

CH$_4$ and H$_2$ at 900°C for about 10 minutes they produced arrays of straight CNTs with up to 30% junction-structures (Figure 2-4).
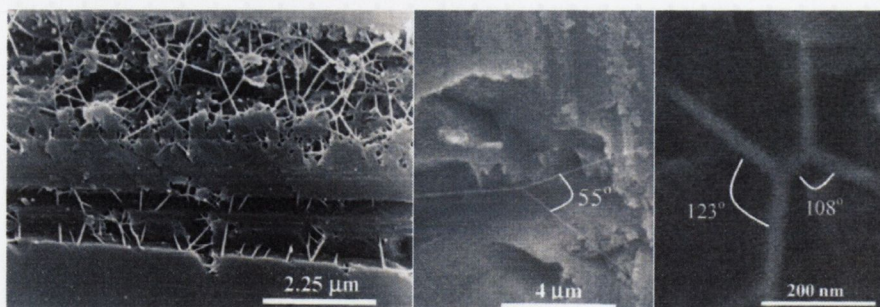
Figure 2-4 SEM micrographs of branched CNTs grown on a roughened Si surface.[127]

The formation of up to of 70% Y branched and of multi-branched carbon nanotubes reported by Satishkumar et al. Nickelocene[124] is used as both catalyst source and carbon feedstock in combination with hydrogen bubbled through thiophene in argon. The operating temperature is 1000°C. The Y-junctions are constituted of multiwalled, relatively straight tubes, in general of similar diameters in the range of 40 nm. The Y-junctions have a 'fish-bone' structure, i.e. the graphitic layers are not oriented parallel with the axis of the nanotubes constituting the junction, but at an angle.

Wei at al have refined a method of controlling the position of multiple Y-junctions (Figure 2-5) in vertically aligned forests of CNTs.[126] By fluctuating gas flow in the CVD reaction chamber they can increase the migration of catalyst particles around the substrate surface while the CNTs are growing from them through a base growth mechanism. When two such particles collide they merge into a single particle and the two separate tubes also merge into a single tube. Through this method they have achieved yields of up to 90% branched CNTs.

Other variations on CVD growth include using porous alumina membranes (PAMs) as a template for Y-junction CNT structures.[50, 142-146]

Other groups have published novel CVD based methods of creating branched structures. For example; Heyning et al use a water based aerosol injection variant of CVD using a floating catalyst to grow bamboo structure CNTs with multiple branches[147] (Figure 2-6). They report that metal containing particles are located at many of the junction sites.

Another novel approach to growing controlled arrays of junction CNTs was developed Aubuchon et al who have produced herringbone structure CNTs using a two stage PECVD method by inducing strong changes in the direction of the electric field after the initial tube growth.[148]
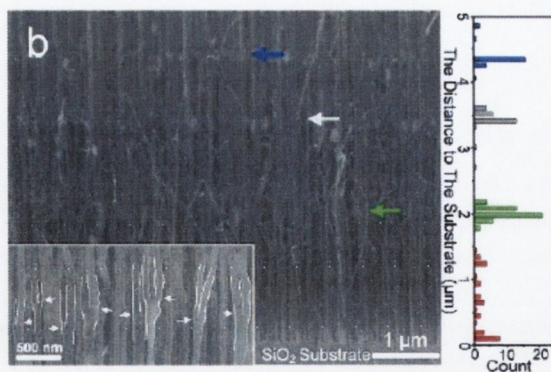
Figure 2-5 a cross-sectional SEM image depicting an array of MWNTs containing four levels and three branching interfaces. The arrows indicate interfaces of junctions, the lower left inset is the high magnification image (the junctions are contoured in white lines and indicated by arrows), and the chart on the right is a histogram showing the distribution of junctions along the growth direction.[126]
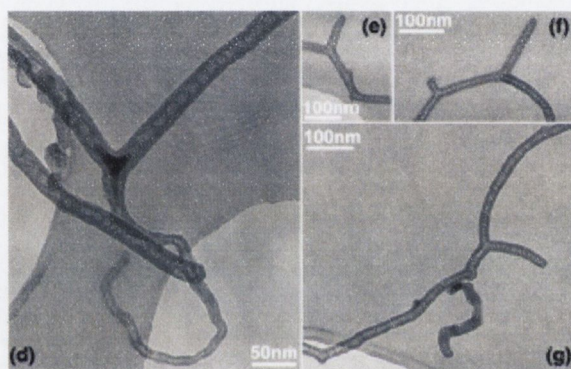
Figure 2-6 TEM micrographs of branched Bamboo structure CNTs. The directions of the bamboo-walls are clearly observable, demonstrating the growth direction of the tubes. The angles between the three tubes making the Y-junctions are on 120° (d) a catalyst particle which is blocked at the junction.[147]

2.6.2 Growth mechanisms for branched CNTs

The first structure models of Y-junction CNTs[149-151] appeared shortly after the discovery of multiwalled CNTs. The model is based on the insertion of non-hexagonal (n-H) rings (at least six heptagons) in the hexagonal network in the region where the three branches of the Y are joined together. All the subsequent structural models[101, 104] follow the same construction principle of the conservation of the sp^2 hybridisation of the carbon network, differing only in type, number and placement of the n-H rings. These variations makes it possible to construct various models for symmetric and asymmetric junctions.[97] A Y-junction is deemed to be symmetric if it is constituted from identical branches oriented at 120° to each other. The following section will give a brief outline of some of the mechanism suggested in the literature for the formation of various forms of CVD grown branched CNT.

2-11

Li et al reported creating identical CNT Y-junctions by pyrolysis of methane over cobalt supported on magnesium oxide. The junctions have straight arms with uniform diameters, and the angles[122] between the three arms are close to 120°. They also report that a triangle-shaped amorphous particle is always found at the centre of each junction. EDS shows that these triangle particles consist of Ca, Si, Mg, and O. The existence of Ca and Si is put down to impurities in starting materials. The authors suggest that these triangle particles result from the splitting of catalyst particles probably due to the thermal fluctuations during growth and left behind during the growth of the tubes. Frequently one of the two long arms of the Y-junction is capped with a pear-shaped particle. These particles have the same chemical composition as that of the triangle-shaped particle with the addition of trace amounts of Co.

Huang et al propose a growth mechanism involving two metal particles.[138] The stem of the junction grows via base growth method, but carries a metal particle at its tip which is partially free of the carbon matrix. At the temperatures used (800 – 1000°C) the iron catalyst behaves in a liquid like manner and can split in two to form two separate tubes which both grow by base growth from the top of the original and are of smaller diameter.

A novel form of branched CNT is presented by Tsai et al composed of a large stem tube 60 – 300 nm in diameter with a cluster of several smaller tubes (10 – 30nm in diameter) growing from its tip. The growth mechanism suggested is specific to PECVD.[137] It is suggested that the CNTs initially grow normally via a tip growth mechanism. However, the large electric bias creates a strong electric field at the tip leading to ion bombardment causes sputtering of graphitic layers around the catalyst particle. This produces holes in the graphitic layers. The catalyst then "leaks" out forming catalyst nodules which can act as sites for further CNT growth (Figure 2-7).

A growth mechanism based on initial tip growth from a single catalyst particle is put forward by Ting et al. They submit that under the elevated temperatures of the CVD chamber (900°C) the catalyst particle elongates within the core of the CNT.[127] This elongated catalyst particle can then break under the compressive stresses within the CNT[152] forming two separate catalyst particles. They suggest that new branches grow from specific close packed plains on the newly formed catalyst particle. The authors do not propose any specific termination mechanism for the branched CNTs but do suggest that all branches terminate at about the same time, about ten minutes into growth. After this time, additional supply of carbon feedstock serves to increase the diameter (but not the length) of the branched tubes, (Figure 2-8).
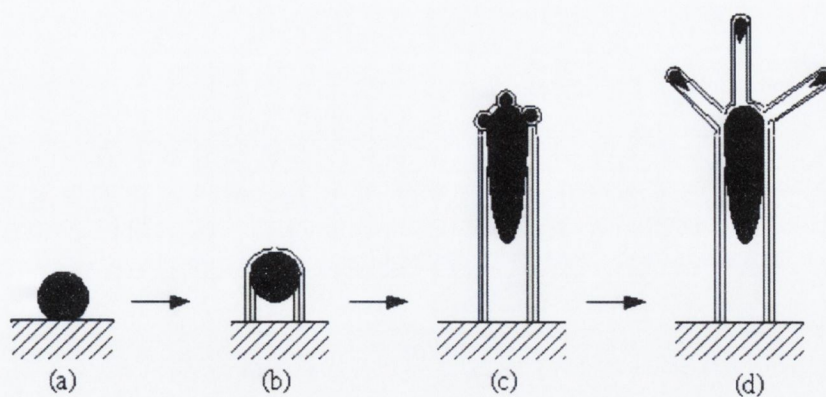
Figure 2-7 A Schematic depicting Multi-branched CNT growth mechanism for tube on tube growth, (a) spherical Pd–Si particle, (b) initial growth stage of CNT, (c) formation of small Pd–Si droplets, and (d) final stages of growth. [137]
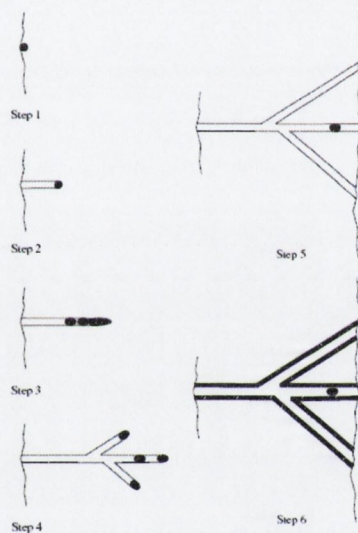
Figure 2-8 A schematic depicting the growth of a four-way branched CNT[127] Step 1: catalyst particle placement. Step 2: initiation of straight tube growth via tip-growth mechanism. Step 3: catalyst particle splitting. Step 4: tube branching, with split particles as initiation sites. Step 5: branch termination on hitting raised substrate region. Step 6: tube wall thickening.

A form of branched CNT containing multiple cores[141] is presented by Hou et al. They suggest that this form of branching arises from a chaotic gas flow within the CVD chamber leading to an uneven distribution of carbon feedstock molecules. This leads to the possibility that a growing CNT will have a surplus of carbon feedstock on one side and a dearth on the other (Figure 2-9). The authors suggest that heptagons are thus introduced into some of the outer layers on one side of the tube resulting in the formation of a second core along side the original.
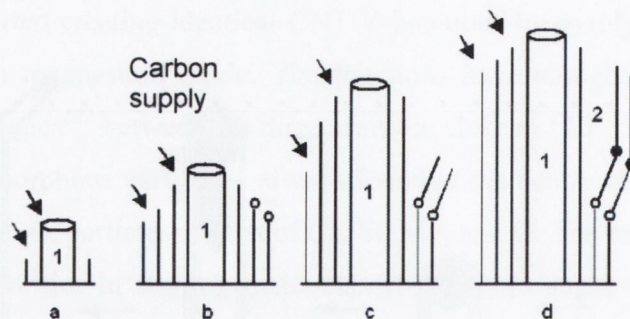
Figure 2-9 Schematic depicting the formation of a multiple core CNT junction. [141]

A novel junction formation mechanism has been employed by Gothard et al to induce branching in CNT mats at desired lengths along the tubes. This is achieved through the introduction of a titanium-containing precursor such as $C_{16}H_{40}N_4Ti$ at key points during their CVD process.[129] The tube initially grows via a base-growth mechanism. When the supply of Ti-containing Fe catalyst particles begins some of these particles attach to the sides of growing CNTs. These particles then act as a seed points for additional tube growth and becoming embedded in the original CNT wall forming a junction (Figure 2-10, left).
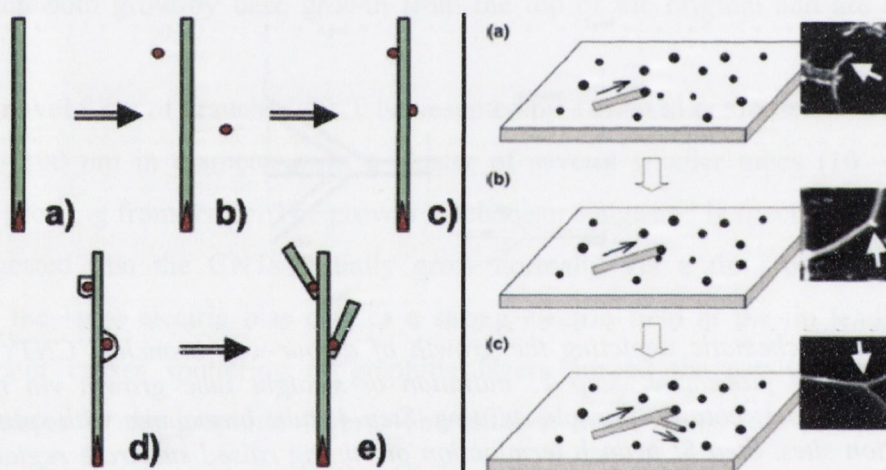
Figure 2-10 Schematics depicting the mechanism for the growth of CNT junctions based around the interaction of a straight tube with an unreacted catalyst particle. Left: shows the growth mechanism for a vertical CNT interacting with an airborne catalyst particle.[129] Right: shows the growth mechanism for a horizontal CNT interacting with a catalyst particle residing on the substrate surface.[125]

A similar mechanism is suggested by Choi et al but for SWNTs growing from Fe-Mo particles on a flat substrate.[125] The tube grows along the substrate surface via a tip growth mechanism. The sidewall of the growing nanotube meets an unreacted catalyst particle which adheres to the side of the tube and acts as a nucleation site in a similar manner to that stated above (Figure 2-10, right).

2-14

Both Heyning et al and Su et al suggest similar growth mechanism for the formation of bamboo structured CNT junctions based on a single catalyst particle.[132, 147] The Bamboo structure arises from the successive formation of CNTs caps stacked within each other (Figure 2-11). Su et al propose that kink and junction formation are due to uneven distribution of carbon feedstock atoms across the catalyst particle surface. Heyning reports that a spherical catalyst particle is more likely to lead to the formation of a CNT while a diamond shaped particle will lead to the formation of carbon fibres with a fishbone structure.

A separate junction formation mechanism based from an initial base growth and not dependent on catalyst splitting is proposed by Wei et al. In this case the junction formation occurs through the coalescence of surface particles due to induced fluctuations in gas flow across the substrate surface[126] (Figure 2-12, left). A similar catalyst fusing mechanism[153] for tip growth tubes is put forward by Tsai et al (Figure 2-12, right), and Ho et al also suggest a weld/fuse type mechanism for junction formation for tubes grown via an open tip mechanism.[154]
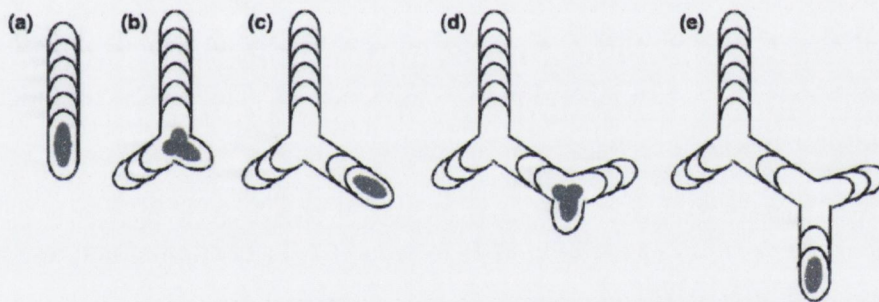
Figure 2-11 A schematic depicting the growth mechanism for a multi-branched bamboo-structure CNT: (a) the growth of a straight nanotube is initiated. (b) The catalyst particle stops and the growth of a branch is initiated. (c) The catalyst particle continues moving while growing the back-bone via a tip-growth mechanism. (d-e) The sequence (a-c) is repeated until the growth of the whole tube is terminated. [147]
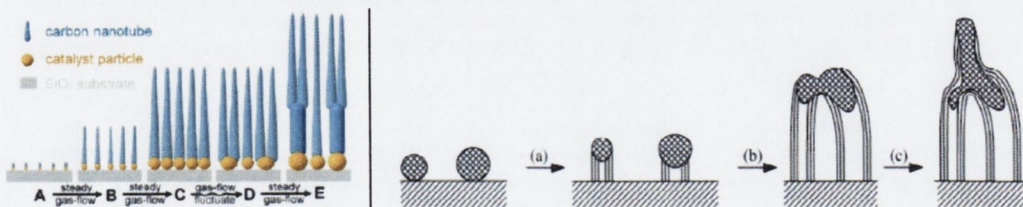
Figure 2-12 A pair of schematics depicting the mechanism for the growth of CNT junctions based on fusing of two separate catalyst particles into one, based from a base-growth model[126] (left) and tip-growth model[153] (right) .

There have been a variety of mechanisms suggested for growth of the different junction morphologies. There are however some common threads that link them. The most

important one is the introduction of either pentagons or heptagons into the graphitic matrix of the CNTs wall(s). A possible cause for this induced change in the structure of the CNT walls comes from another common thread; the elongation and subsequent splitting of catalyst particles within the tube core. These split particles are often seen caught at the junction points. As a general rule: branching mechanisms involving a tip growth mechanism entail catalyst splitting within the tube core. This is not the case for branching mechanisms involving base growth.

2.6.3 Applications of branched CNTs

Branched CNT structures have a number of possible applications; for example Park et al have recently published the results of a simulation to demonstrate the possibility of using a Y-junction CNT to separate K^+ from Cl^- ions in aqueous solution.[155] Zeng et al measured the field emission responses of a randomly aligned mat of branched CNTs compared with that of s similarly prepared mat of normal CNTs. They found that the former had a lower "turn on" electric field.[108, 154] However, the most exciting possibility for CNT junction-structures is their potential integration into CMOS circuit architectures.[13, 31, 32, 156]

To this end much work has gone into predicting and modelling the possible applications and responses of such devices. Work has been published investigating their rectification properties,[104-106] use as 2-D tunnelling junctions,[107] as well as the effect of pentagon/heptagon distribution on their electrical responses.[96, 144] However, relative to the amount of work done in modelling and growing CNT junction-structures, much less experimental data is available on their conduction properties.

An ingenious method to measure conduction through the Y-junction structures[143] employing CNTs grown on porous alumina membranes with a high concentration of Y-junction nanochannels[142] has been reported by Papadoupoulos et al. Their results show rectifying behaviour in arrays of junctions, averaging over 100–10000 of individual junctions connected in parallel. These junctions were measured in-situ within the PAM after the barrier layer was removed. The thinner "branches" were connected to a common Al electrode, while the thicker stems were connected to an Au electrode deposited on top of the PAM. Room temperature I-V measurements on these devices show repeatable rectifying behaviour that was duplicated in measurements made on single Y-junctions.

However, Bandaru et al present abrupt electrical switching in Y-junction CNTs[157] that is more pronounced that other works where mere diode-like behaviour is reported by Papadoupoulos and others.[124, 143] The samples were prepared by suspending the MWNT Y-junctions in ethanol and depositing them on a SiO_2/Si substrate with patterned Au pads. An

ion-beam FIB-SEM system was then used to deposit the Pt lead wires that connect the terminals of the Y-junction to the contact pads. The inter-branch behaviour was observed to be ohmic, with resistances in the range of 100−400 kΩ. This high value is attributed to the difficulty in achieving ideal ohmic contacts.

The functionality of several devices were tested using a control D.C. voltage swept on one terminal of the Y-junction while the current through the other two terminals was probed under a fixed A.C. bias ranging from 0.1 to 1.0 V. As the D.C. voltage was increased, at a certain point the Y-junction goes from nominally conducting to a pinched-off state (Figure 2-13). This switching behaviour was observed for all three terminals of the Y-junction, at varying D.C. bias voltages, and in several samples.

In progress towards further device applications Park et al suggest that the positioning of a particle; dielectric or insulating in nature, could increase the efficiency in the gating of a Y-junction device giving it a function similar to that of a MOSFET ,where the stem is analogous to a gate, the dielectric particle plays the role of the oxide, and the channel is formed by conduction through the branches.[158]

Little work have been done on the electrical properties of more complex branched CNT structures, however Wallin et al have demonstrated a multi input AND logic gate, from a 5 branch junction fabricated from a semiconducting hetrostructure,[94] and predict that a multi branched CNT junction will have similar results.
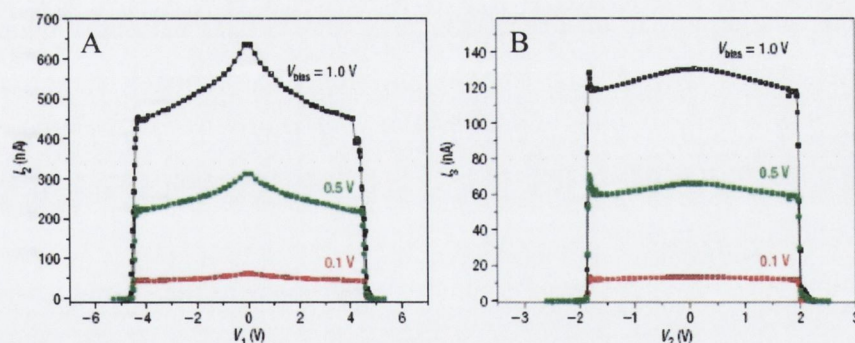
Figure 2-13 I-V plots demonstrating near perfect electrical switching in a CNT Y-junction.[157] An abrupt modulation of the electrical current through two branches of the Y-junction is seen on varying the D.C. bias voltage on the third branch. A) The voltage at which the switching action occurs is ~4.6 V on the stem. B) the switching on both of the branches occurs at ~2 V. The disparate voltage values could be related to the character, diameter, and defects, of the constituents (branch/stem) of the Y-junction.

2.7 Raman spectroscopy of CNTs

Raman spectroscopy is a form of vibrational spectroscopy pioneered by C. V. Raman. The technique is especially useful in the characterisation of CNTs, both due to their unique Raman fingerprint and the ability of the technique to give a qualitative measure of the graphitisation and purity of a sample of CNTs. Raman can also be used to measure changes in a CNT system, such as purification, or conversely its interactions additional atomic or molecular species. The following sections will give a brief overview of the theory behind Raman spectroscopy and its specific advantages and uses with respect to CNTs.

2.7.1 Introduction to Raman spectroscopy

The vast majority of photons incident on a particular molecule will be elastically scattered, i.e. the energy of the scattered photon is equal to its incident energy. Raman spectroscopy deals with the very small number of photons (about 1 in 10^7) that, on hitting an atom or molecule are scattered away with an amount of energy different to their incident energy. The effect occurs when the photon interacts with the molecules electric dipole. The scattering can be thought of as an excitation to a virtual state (lower in energy than a real electronic transition) with an almost immediate de-excitation to a new real state of different energy to the initial one. This virtual state can be considered to be a distortion of the electron distribution in a covalent bond.

Raman scattering can be further separated into Stokes and anti-Stokes radiation. When an incident photon gives up some of its energy to the incident molecule coming away with less energy it is known as Stokes radiation. However, if the photon is scattered from an atom or molecule in an excited state and comes away with greater energy then this is known as anti-Stokes radiation.

The intensity of the Stokes Raman is proportional to the number of illuminated molecules in their lowest vibrational state. Conversely the intensity of anti-Stokes radiation is proportional to number of illuminated molecules that are already in a higher vibrational state. At thermal equilibrium there will be a far greater number of molecules in a non-excited states, therefore generally Stokes Raman will have a greater intensity than anti-Stokes Raman (Figure 2-14).
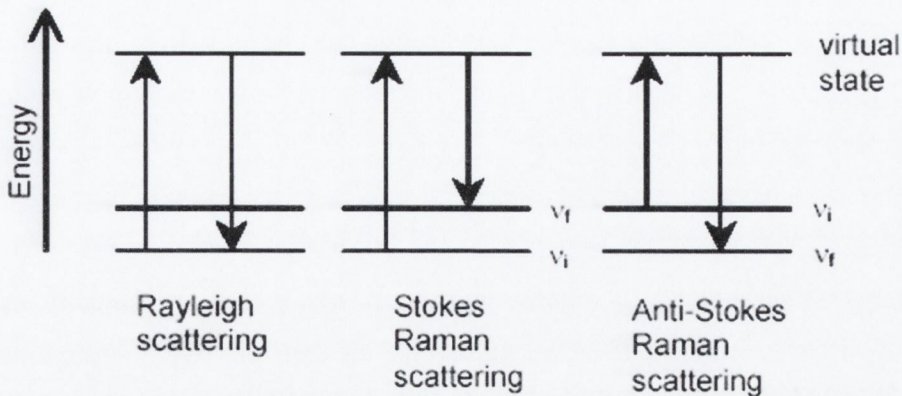
Figure 2-14 Energy level diagrams for Raleigh scatter; Stokes Raman scattering and Anti-Stokes Raman scattering.

A Raman spectrum is a plot of scattered light intensity versus energy (quoted in inverse wavelength, cm^{-1}). The intensity is usually given in arbitrary units and is proportional to the number of photons of a given energy collected during a specific scan. The units on the x-axis are usually quoted in "wavenumbers of shift from the exciting wavelength" often referred to as "Raman shift". Wavenumber is the reciprocal of wavelength given in inverse centimetres, and is effectively the number of waves per centimetre. For example the wavelength of a HeNe laser is 632.8 nm which corresponds to a wavenumber of 1580.3 cm^{-1} which coincidentally corresponds well to the energy of the G-band for CNTs. A wavenumber can be thought of as a unit of energy:

$$E = hv = \frac{hc}{\lambda} = hc\omega$$

Where: h: Planck's constant; v: the frequency of the light; c: the speed of light; λ: the wavelength of the light; and ω: the wavenumber of the light. So the "Raman shift" is the difference in energy between the scattered light and the excitation radiation.

Typical strong Raman scatterers are molecules with distributed electron clouds, such as carbon-carbon double bonds. The π-electron cloud of the double bond is easily distorted in an external electric field. Bending or stretching the bond changes the distribution of electron density substantially, and causes a large change in induced dipole moment.

In Raman spectroscopy the energy levels of molecules are explored by examining the frequencies present in the radiation scattered by the molecules due to changes in their vibration and rotation states. These scattering events occur in less than 10^{-14} seconds. The gross selection rule for rotational Raman transitions is that the molecule must be anisotropically polarisable. In other words for a vibration to be Raman active, the polarisability of the molecule must change with the vibrational motion. Polarisability, α is

the distortion of a molecule in and electric field, ε such that dipole moment, $\mu = \alpha\varepsilon$ in addition to any permanent dipole moment it may have. This means that Raman spectroscopy is useful for analyzing molecules without a permanent dipole moment which would not show up on an IR spectrum.

2.7.2 Advantages of Raman

Raman spectroscopy has many advantages as a technique. Notably its selection rules allow it to measure molecular vibrations invisible to FT-IR techniques. Raman spectroscopy requires no specific sample preparation. Samples can be measured as solids, powders, films or even solutions. The use of micro-Raman allows the investigation of areas in the same order of magnitude as the laser spot size (tens of microns). This allows not only for very small amounts of sample to be analysed but also for analysis of very specific surface locations for be analysed, and the possibility of surface mapping. The use of relatively low powered lasers means that Raman is effectively a non-destructive technique and allows samples to remain unaltered for further characterisation techniques, such as electron microscopy. Raman spectroscopy is a very fast technique generally needing less than a minute to acquire a spectrum.

Raman spectroscopy is attractive for use with CNTs not only for the above reasons, but the distinctive Raman spectrum for CNTs allows it to be used as a very fast initial check for the presence of CNTs. A great deal can be learned about the specific qualities of a CNT sample from the positions and shapes of these peaks, as well as their sizes relative to each other. These specific peaks will now be discussed in more detail.

2.7.3 The Raman Spectrum for carbon nanotubes

Raman spectroscopy has been shown to be a very useful tool in the investigation of carbon nanotubes.[7, 159-162] One of the main reasons that Raman is such a powerful tool in the characterisation of carbon nanotubes is the very distinctive and relatively simple spectra given by nanotubes. Raman spectroscopy is very sensitive to carbon materials with sp^2- and sp^3-type bonding, resulting in carbon nanotubes generally giving a very strong and clear Raman spectrum. The Raman spectrum for SWNT shows three distinct regions between 100 and 2000 cm^{-1}. There are other vibrational modes above 2000 cm^{-1}, such as the second order peaks at around 2600 cm^{-1} which has also been studied[7, 163, 164] but will not be discussed in section.

The first region of interest in the Raman spectrum for CNTs is the Radial Breathing Modes (RBM) located between 100 - 400 cm^{-1}. As the name suggests the RBM region of

the Raman spectrum for carbon nanotubes arises from the resonance of the exspansion and contraction of the diameter of the nanotube. Each distinct peak in the RBM region corresponds to nanotubes of different diameter,[161, 165] in general RBM peaks at lower wavelenghts correspond to nanotubes of larger diameter.[166] This region of the spectrum is of interest as it can be used to indicate size selection of polymers, this can be seen from the difference in relative intensities of the RBM peaks before and after addition of the polymer. Polymer or other species adsorbed on the surface will change the characteristic RBMs of the tubes causing a upshift in the RBM peak positions. The effects of such interactions on the RBM peaks can be better understood if we model the vibration as a simple harmonic oscillator:

$$\omega = \frac{1}{2\pi c} \left(\frac{k}{\mu_r} \right)^{\frac{1}{2}}$$

where c: the speed of light; k: force constant; and μ_r = reduced mass (i.e. $m_1 m_2 / (m_1 + m_2)$).

From this we can see that the stiffer the bond (i.e. the larger the force constant then the higher the vibrational frequency. For example a carbon-carbon double bond will have a higher vibrational frequency than a carbon-carbon single bond, and a triple bond will be higher again. Also from this model we can see that the addition of say, a polymer wrapping around an individual tube will increase the Young's modulus of the radial breathing vibration and hence up-shift the position of the RBM.

The RBM region is not as defined for multi-walled nanotube (MWNT) samples due to the interference of the concentric shells. In fact RBM modes are in general not seen for MWNTs. Since MWNTs contain a range of shell diameters some of the more subtle features seen in the Raman spectra for SWNTs are no longer seen. In fact, the Raman spectrum for MWNTs is closer to that of graphite. The RBM vibrations of the inner shells tend to be dampened by the outer shells. The diameters of the outer shells are often large so that their RBM vibrations are so low in frequency and so weak as to be undetectable. However, in certain specific cases where MWNTs can be created with very small inner shells RBMs can be measured.[79, 167, 168]

The next region of interest is the D-line at 1300 - 1360 cm^{-1}. This line stems from disorder in sp^3 hybridised molecular bonds. The D-band can be used a rough measure of the amount of impurities and defects in a carbon nanotube sample. As can be seen in Figure 2-15 the D-band is of comparible height to the G-band for amorphous carbon in carbon black, whereas there is no discernible D-band for Highly Ordered Pyrolytic

Graphite (HOPG). The D band is in a similar position to the Raman peak seen for diamond located at 1330 cm^{-1} due to sp^3 bonded carbon.

The third distinct region of the Nanotube spectrum is the G-band, which occurs at around 1580 cm^{-1} and gets it name from the distictive Raman spectrum of graphite. For Graphite only the E$_{2g}$ modes are Raman active. The E$_{2g1}$ modes correspond to in-plane shear between the layers and occur at a very low frequency (~42 cm^{-1}) which is below the lower limit of most commercially available Raman instruments. The frequency is so low because these vibrations are against only the weak restoring force of the interlayer bond. The second band seen in the Raman spectrum for graphite is due to the E$_{2g2}$ modes and represents in-plane displacements. The frequency is much higher as the restoring force is much greater. The G-line arises from interaction with the sp^2 hybredised bonding similar present in graphite; hence the name G-band. The physical representation of the vibrations that make up the G-band for a SWNT are show in Figure 2-16
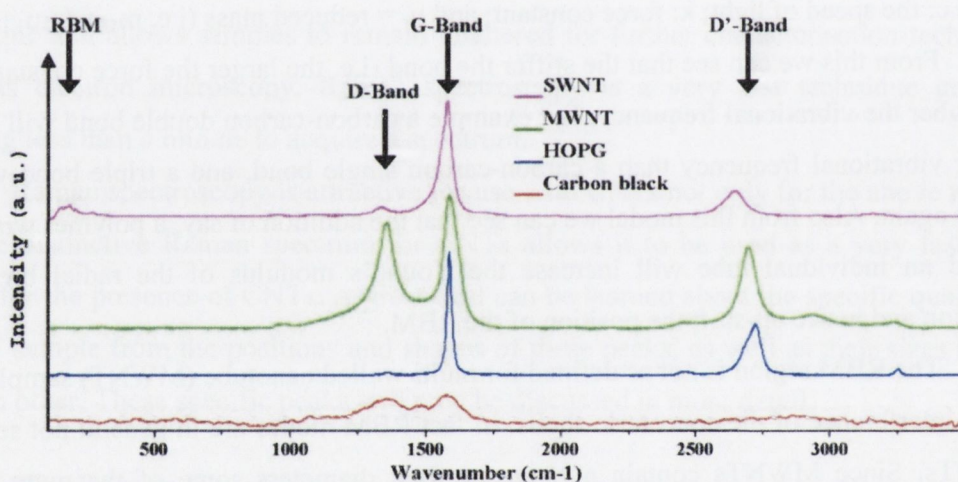
Figure 2-15 Typical Raman spectra for (top to bottom) single wall carbon nanotubes (SWNTs), mutliwall carbon nanotubes (MWNT), highly ordered pyrolytic graphite, and carbon black (amorphous carbon).

(a) E_{2g} 17 cm^{-1}

(b) E_{1g} 118 cm^{-1}

(c) A_{1g} 165 cm^{-1}

(d) E_{2g} 368 cm^{-1}

(e) E_{1g} 1585 cm^{-1}

(f) A_{1g} 1587 cm^{-1}

(g) E_{2g} 1591 cm^{-1}
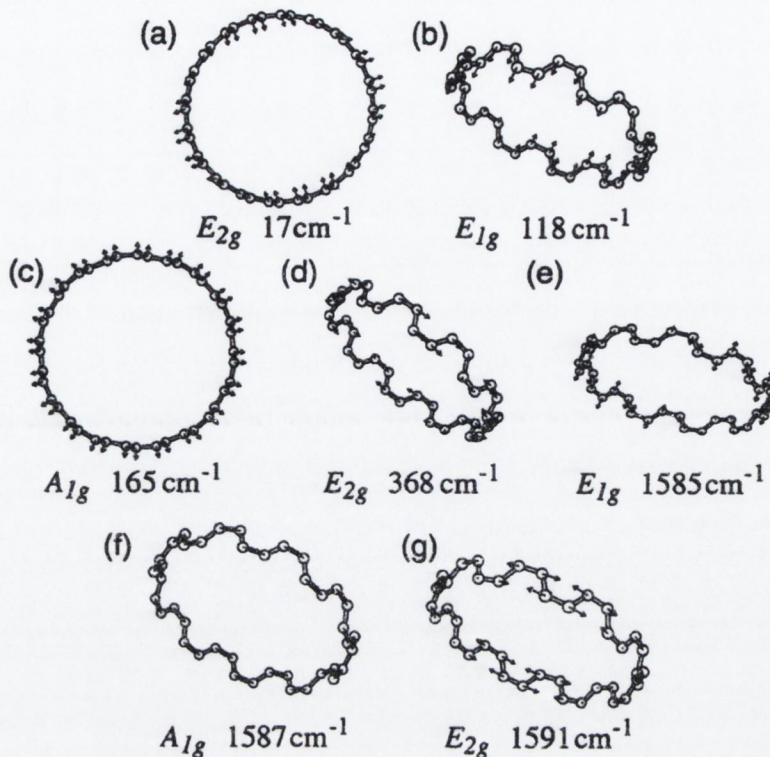
Figure 2-16 Shows a schematic of the various Raman-active vibrations for a SWNT. [1]

The G^+ - G^- splitting is very weak in MWNTs and tends to be broadened due to interference between the different shells of varying diameter. This results in the G-band appearing as a weakly asymmetric peak centred around 1582 cm^{-1}. The G-band is split into two main components: the G^+ and G^- peaks which are positioned at ~ 1590 cm^{-1} & 1570 cm^{-1} respectively. The G^+ peak is associated with vibrations along the axis of the tube. The G^- peak is associated with vibrations perpendicular to the axis.

2.7.4 What can be learned from Raman CNT spectra?

As mentioned above the individual diameters of SWNTs and the effect of polymer wrapping can be estimated from the RBM region (see Appendix B). However for MWNTs, which in general have no RBM region there is a lot of information about the tubes "quality" and purity to be gleaned from the D- and G-bands and their relation to each other.

The ratio of integrated area under the D-band with respect to that of the G-band can be used as a qualitive measure of nanotube "quality".[169] The D-band arises from sp^3 which occurs in amorphous carbon. A reduction of the amount of amorphous in a sample carbon will result in a decrease in the size of the D-band with respect to the G-band. Conversely, the addition of extra sp^3 hybridised carbons into the CNT matrix will cause increase in

intensity of the D-band with respect to the G-band. This increased sp^3 hybridisation can arise from the addition of carbon heptagons and pentagons, such those present in kinks and junctions. The D-band intensity will increased through or the addition of chemical ligands and the physical or chemical breaking of the tubes.

The G-line will be upshifted for nanotubes that are less "graphitised" i.e. that have an amorphic graphite coating, or have other species on the outer shell. As disorder of individual layers is increased both the D- and G-line peaks broaden.

An example of the relationship with the D- and G-bands can be seen in Figure 2-17, which shows the Raman spectra of a MWNT sample before and after cleaning to remove amorphous carbon. It can be seen that the D-band decreases dramatically with respect to the G-band after cleaning.
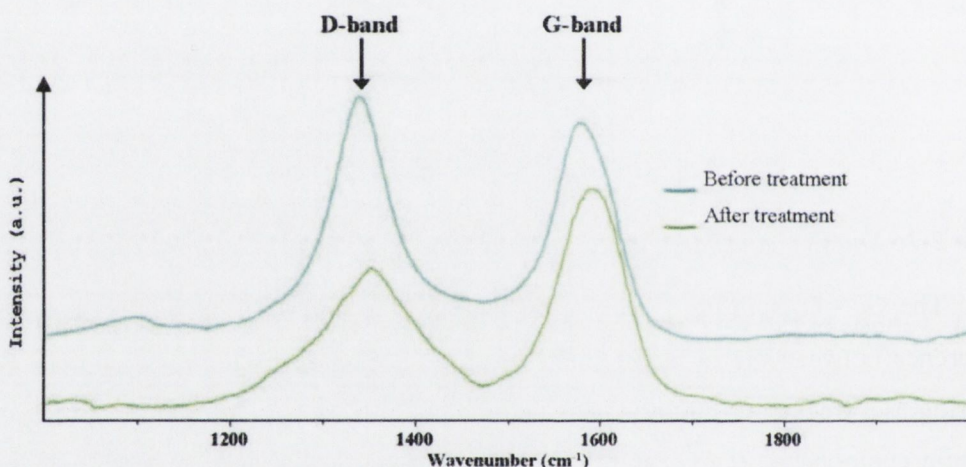
Figure 2-17 Raman spectra showing the D- & G- band region for MWNTs before (top) and after (bottom) cleaning treatment to remove amorphous carbon from the system.

2.8 References

[1] M. S. Dresselhaus, *Science of fullerenes and carbon nanotubes* (Academic Press, San Diego ; London 1996).

[2] M. Endo, S. Iijima, and M. Dresselhaus, *Carbon nanotubes* (Pergamon, Oxford, 1996).

[3] C. N. R. Rao, *Nanotubes and nanowires* (Cambridge : Royal Society of Chemistry, 2005).

[4] A. Cassell, L. Delzeit, C. Nguyen, et al., Journal De Physique Iv **11**, 401 (2001).

[5] A. Chatterjee and B. L. Deopura, Fibers and Polymers **3**, 134 (2002).

[6] L. Delzeit, A. Cassell, D. Hash, et al., Plasma Sources Science and Technology **12**, 205 (2003).

[7] M. S. Dresselhaus, G. Dresselhaus, R. Saito, et al., Physics Reports **409**, 47 (2005).

[8] M. Endo, T. Hayashi, Y. A. Kim, et al., Japanese Journal of Applied Physics Part 1- Regular Papers Brief Communications & Review Papers **45**, 4883 (2006).

[9] C. Oncel and Y. Yurum, Fullerenes Nanotubes and Carbon Nanostructures **14**, 17 (2006).

[10] P. Serp, M. Corrias, and P. Kalck, Applied Catalysis A: General **In Press, Corrected Proof** (2003).

[11] O. A. Shenderova, V. V. Zhirnov, and D. W. Brenner, Critical Reviews in Solid State and Materials Sciences **27**, 227 (2002).

[12] S. B. Sinnott and R. Andrews, Critical Reviews in Solid State and Materials Sciences **26**, 145 (2001).

[13] M. Terrones, International Materials Reviews **49**, 325 (2004).

[14] http://nanotube.msu.edu/.

[15] http://www.nanotech-now.com/nanotube-buckyball-sites.htm.

[16] R. Saito and H. Kataura, (Springer-Verlag, Berlin, 2000).

[17] http://physicsweb.org/articles/world/11/1/9

[18] W. J. Liang, M. Bockrath, D. Bozovic, et al., Nature **411**, 665 (2001).

[19] P. G. Collins and P. Avouris, Applied Physics a-Materials Science & Processing **74**, 329 (2002).

[20] M. Terrones, F. Banhart, N. Grobert, et al., Physical Review Letters **89**, 075505 (2002).

[21] S. Heinze, J. Tersoff, R. Martel, et al., Physical Review Letters **89**, art. no. (2002).

[22] V. Derycke, R. Martel, J. Appenzeller, et al., Nano Letters **1**, 453 (2001).

[23] A. Javey, Q. Wang, A. Ural, et al., Nano Letters **2**, 929 (2002).

[24] N. R. Franklin, Y. M. Li, R. J. Chen, et al., Applied Physics Letters **79**, 4571 (2001).

[25] R. Martel, V. Derycke, C. Lavoie, et al., Physical Review Letters **87**, 256805 (2001).

[26] E. Yenilmez, Q. Wang, R. J. Chen, et al., Applied Physics Letters **80**, 2225 (2002).

[27] S. J. Wind, J. Appenzeller, R. Martel, et al., Applied Physics Letters **81**, 1359 (2002).

[28] S. J. Wind, J. Appenzeller, R. Martel, et al., Applied Physics Letters **80**, 3817 (2002).

[29] A. Bachtold, P. Hadley, T. Nakanishi, et al., Science **294**, 1317 (2001).

[30] A. Bachtold, P. Hadley, T. Nakanishi, et al., Physica E-Low-Dimensional Systems & Nanostructures **16**, 42 (2003).

[31] A. P. Graham, G. S. Duesberg, R. Seidel, et al., Diamond and Related Materials **13**, 1296 (2004).

[32] P. G. Collins and P. Avouris, Scientific American **283**, 62 (2000).

[33] A. Y. Cao, B. Q. Wei, Y. Jung, et al., Applied Physics Letters **81**, 1297 (2002).

[34] R. Vajtai, K. Kordas, B. Q. Wei, et al., Materials Science & Engineering C-Biomimetic and Supramolecular Systems **19**, 271 (2002).

[35] B. Q. Wei, Z. J. Zhang, G. Ramanath, et al., Applied Physics Letters **77**, 2985 (2000).

[36] Y. H. Li, C. L. Xu, B. Q. Wei, et al., Chemistry of Materials **14**, 483 (2002).

[37] B. Q. Wei, R. Vajtai, Z. J. Zhang, et al., Journal of Nanoscience and Nanotechnology **1**, 35 (2001).

[38] B. Q. Wei, R. Vajtai, Y. Jung, et al., Nature **416**, 495 (2002).

[39] C. J. Lee, D. W. Kim, T. J. Lee, et al., Chemical Physics Letters **312**, 461 (1999).

[40] Z. F. Ren, Z. P. Huang, J. W. Xu, et al., Science **282**, 1105 (1998).

[41] Y. C. Choi, D. W. Kim, T. J. Lee, et al., Synthetic Metals **117**, 81 (2001).

[42] B. Q. Wei, Z. J. Zhang, P. M. Ajayan, et al., Carbon **40**, 47 (2002).

[43] W. Z. Li, S. S. Xie, L. X. Qian, et al., Science **274**, 1701 (1996).

[44] Z. W. Pan, S. S. Xie, B. H. Chang, et al., Chemical Physics Letters **299**, 97 (1999).

[45] J. Kong, H. T. Soh, A. M. Cassell, et al., Nature **395**, 878 (1998).

[46] L. Valentini, I. Armentano, J. M. Kenny, et al., Materials Letters, 1 (2003).

[47] B. Q. Wei, R. Vajtai, Y. Jung, et al., Chemistry of Materials **15**, 1598 (2003).

48 J. B. Bai, Materials Letters **57**, 2629 (2003).

49 Y. H. Mo, A. K. M. F. Kibria, and K. S. Nahm, Synthetic Metals **122**, 443 (2001).

50 Y. C. Sui, B. Z. Cui, R. Guardian, et al., Carbon **40**, 1011 (2002).

51 J. Zhao, Q. Y. Gao, C. Gu, et al., Chemical Physics Letters **358**, 77 (2002).

52 X. Wang, Z. Hu, Q. Wu, et al., Catalysis Today **72**, 205 (2002).

53 G. L. Hornyak, A. C. Dillon, P. A. Parilla, et al., Nanostructured Materials **12**, 83 (1999).

54 X. Y. Zhang, L. D. Zhang, G. H. Li, et al., Materials Science and Engineering A **308**, 9 (2001).

55 Z.-h. Yuan, H. Huang, L. Liu, et al., Chemical Physics Letters **345**, 39 (2001).

56 S.-H. Jeong and K.-H. Lee, Synthetic Metals **139**, 385 (2003).

57 I. Radu, Y. Hanein, and D. H. Cobden, Nanotechnology **15**, 473 (2004).

58 E. Lahiff, R. Leahy, A. I. Minett, et al., (AIP, Tirol, Austria, 2004), p. 544.

59 T. A. Hanaoka, A. Heilmann, M. Kroll, et al., Applied Organometallic Chemistry **12**, 367 (1998).

60 Y. Li, W. Kim, Y. Zhang, et al., Journal of Physical Chemistry B **105**, 11424 (2001).

61 A. M. Cassell, J. A. Raymakers, J. Kong, et al., Journal of Physical Chemistry B **103**, 6484 (1999).

62 Y. Zhang, Y. Li, W. Kim, et al., Applied Physics a-Materials Science & Processing **74**, 325 (2002).

63 X. Y. Zhang, L. D. Zhang, M. J. Zheng, et al., Journal of Crystal Growth **223**, 306 (2001).

64 M. J. Kim, T. Y. Lee, J. H. Choi, et al., Diamond and Related Materials **12**, 870 (2003).

65 S. K. Biswas, R. Vajtai, B. Q. Wei, et al., Applied Physics Letters **84**, 2889 (2004).

66 P. L. Chen, J. K. Chang, C. T. Kuo, et al., Diamond and Related Materials **13**, 1949 (2004).

67 Y. Avigal and R. Kalish, Applied Physics Letters **78**, 2291 (2001).

68 Y. G. Zhang, A. L. Chang, J. Cao, et al., Applied Physics Letters **79**, 3155 (2001).

69 N. Franklin and H. J. Dai, Advanced Materials **12**, 890 (2000).

70 M. Meyyappan, L. Delzeit, A. Cassell, et al., Plasma Sources Science & Technology **12**, 205 (2003).

71 S. M. Huang, X. Y. Cai, and J. Liu, Journal of the American Chemical Society **125**, 5636 (2003).

72 S. M. Huang, B. Maynor, X. Y. Cai, et al., Advanced Materials **15**, 1651 (2003).

73 S. M. Huang, M. Woodson, R. Smalley, et al., Nano Letters **4**, 1025 (2004).

74 L. M. Huang, X. D. Cui, B. White, et al., Journal of Physical Chemistry B **108**, 16451 (2004).

75 L. X. Zheng, M. J. O'Connell, S. K. Doorn, et al., Nature Materials **3**, 673 (2004).

76 B. H. Hong, J. Y. Lee, T. Beetz, et al., Journal of the American Chemical Society **127**, 15336 (2005).

77 L. Huang, W. S. J, and S. P. O'Brien, Nano Letters **3**, 299 (2003).

78 A. Ural, Y. M. Li, and H. J. Dai, Applied Physics Letters **81**, 3464 (2002).

79 J. Zhu, M. Yudasaka, and S. Iijima, Chemical Physics Letters **380**, 496 (2003).

80 H. Ago, J. Qi, K. Tsukagoshi, et al., Journal of Electroanalytical Chemistry **00**, 1 (2002).

81 Y. M. Li, D. Mann, M. Rolandi, et al., Nano Letters **4**, 317 (2004).

82 A. M. Cassell, N. R. Franklin, T. W. Tombler, et al., Journal of the American Chemical Society **121**, 7975 (1999).

83 L. Marty, V. Bouchiat, A. M. Bonnot, et al., Microelectronic Engineering **61-2**, 485 (2002).

[84] T. W. Tombler, C. W. Zhou, L. Alexseyev, et al., Nature **405**, 769 (2000).

[85] N. R. Franklin, Q. Wang, T. W. Tombler, et al., Applied Physics Letters **81**, 913 (2002).

[86] Y. Homma, Y. Kobayashi, T. Ogino, et al., Applied Physics Letters **81**, 2261 (2002).

[87] Y. Zhang, N. W. Franklin, R. J. Chen, et al., Chemical Physics Letters **331**, 35 (2000).

[88] C. W. Zhou, J. Kong, and H. J. Dai, Physical Review Letters **84**, 5604 (2000).

[89] H. Q. Xu, I. Shorubalko, D. Wallin, et al., IEEE Electron Device Letters **25**, 164 (2004).

[90] I. Shorubalko, H. Q. Xu, I. Maximov, et al., IEEE Electron Device Letters **23**, 377 (2002).

[91] I. Shorubalko, H. Q. Xu, P. Omling, et al., Applied Physics Letters **83**, 2369 (2003).

[92] K. Hieke and M. Ulfward, Physical Review B **62**, 16727 (2000).

[93] Z. Wei, M. Zhang, M. Yu, et al., Advanced Materials **15**, 1382 (2003).

[94] D. Wallin and H. Q. Xu, Applied Physics Letters **86**, 253510 (2005).

[95] Y. Lu, X. Yang, Y. Ma, et al., Chemical Physics Letters **419**, 390 (2006).

[96] H. Liu, Physics Letters A **339**, 378 (2005).

[97] L. P. Biro, Z. E. Horvath, G. I. Mark, et al., Diamond and Related Materials **13**, 241 (2004).

[98] F. Y. Meng, S. Q. Shi, D. S. Xu, et al., Carbon **44**, 1263 (2006).

[99] F. Y. Meng, S. Q. Shi, D. S. Xu, et al., Journal of Chemical Physics **124**, 024711 (2006).

[100] R. Egger, B. Trauzettel, S. Chen, et al., New Journal of Physics **5** (2003).

[101] G. Treboux, P. Lapstun, and K. Siiverbrook, Chemical Physics Letters **306**, 402 (1999).

[102] V. Meunier, M. B. Nardelli, J. Bernholc, et al., Applied Physics Letters **81**, 5234 (2002).

[103] D. Grimm, R. B. Muniz, and A. Latge, Physical Review B **68** (2003).

[104] A. N. Andriotis, M. Menon, D. Srivastava, et al., Physics Review B **65**, 165416 (2002).

[105] A. N. Andriotis, M. Menon, D. Srivastava, et al., Physical Review Letters **8706**, art. no. (2001).

[106] A. N. Andriotis, M. Menon, D. Srivastava, et al., Applied Physics Letters **79**, 266 (2001).

[107] M. Menon and D. Srivastava, Physical Review Letters **79**, 4453 (1997).

[108] B. Zeng, S. Tian, and Z. Yang, Applied Surface Science **251**, 245 (2005).

[109] G. Treboux, Journal of Physical Chemistry B **103**, 10378 (1999).

[110] A. Cummings, in *Department of Electrical Engineering and Computer Science* (WASHINGTON STATE UNIVERSITY, 2004), Vol. MASTER OF SCIENCE IN ELECTRICAL ENGINEERING, p. 68.

[111] Z. Wang, Z. Zhao, and J. Qiu, Carbon **44**, 1321 (2006).

[112] D. Zhou and S. Seraphin, Chem Phys Lett **238**, 286 (1995).

[113] Z. Osvath, A. A. Koos, Z. E. Horvath, et al., Chemical Physics Letters **365**, 338 (2002).

[114] Z. Klusek, S. Datta, P. Byszewski, et al., Surface Science **507**, 577 (2002).

[115] D. Srivastava, M. Menon, and P. M. Ajayan, Journal of Nanoparticle Research **5**, 395 (2003).

[116] I. Jang, S. B. Sinnott, D. Danailov, et al., Nano Letters **4**, 109 (2004).

[117] P. Nagy, R. Ehlich, L. P. Biro, et al., Applied Physics A: Materials Science and Processing **70**, 481 (2000).

[118]   L. P. Biro, R. Ehlich, Z. Osvath, et al., Materials Science & Engineering C-Biomimetic and Supramolecular Systems **19**, 3 (2002).

[119]   L. P. Biro, R. Ehlich, Z. Osvath, et al., Diamond and Related Materials **11**, 1081 (2002).

[120]   A. A. Koos, R. Ehlich, Z. E. Horvath, et al., Materials Science & Engineering C-Biomimetic and Supramolecular Systems **23**, 275 (2003).

[121]   H. W. Zhu, L. J. Ci, C. L. Xu, et al., Diamond and Related Materials **11**, 1349 (2002).

[122]   W. Z. Li, J. G. Wen, and Z. F. Ren, Applied Physics Letters **79**, 1879 (2001).

[123]   D. Y. Ding, J. N. Wang, F. Yu, et al., Applied Physics A: Materials Science and Processing **81**, 805 (2005).

[124]   B. C. Satishkumar, P. J. Thomas, A. Govindaraj, et al., Applied Physics Letters **77**, 2530 (2000).

[125]   Y. C. Choi and W. Choi, Carbon **43**, 2737 (2005).

[126]   D. Wei, Y. Liu, L. Cao, et al., Nano Letters **6**, 186 (2006).

[127]   J.-M. Ting, T.-P. Li, and C.-C. Chang, Carbon **42**, 2997–3002 (2004).

[128]   J. M. Ting and C. C. Chang, Applied Physics Letters **80**, 324 (2002).

[129]   N. Gothard, C. Daraio, J. Gaillard, et al., Nano Letters **4**, 213 (2004).

[130]   D. Liu, J. Chen, W. Deng, et al., Materials Letters **58**, 2764– 2767 (2004).

[131]   R. W. Leahy, E. Lahiff, A. I. Minett, et al., (International Society for Optical Engineering, Bellingham WA, WA 98227-0010, United States, Dublin, Ireland, 2005), Vol. 5824, p. 62.

[132]   L. F. Su, J. N. Wang, F. Yu, et al., Chemical Vapor Deposition **11**, 351 (2005).

[133]   B. Gan, J. Ahn, Q. Zhang, et al., Diamond and Related Materials **9**, 897 (2000).

[134]   B. Gan, J. Ahn, Q. Zhang, et al., Chemical Physics Letters, 23 (2001).

[135]   B. Gan, J. Ahn, Q. Zhang, et al., Materials Letters **45**, 315 (2000).

[136]   B. O. Boskovic, V. Stolojan, D. A. Zeze, et al., Journal of Applied Physics **96**, 3443 (2004).

[137]   S.-H. Tsai, C.-T. Shiu, S.-H. Lai, et al., Carbon **40**, 1597–1617 (2002).

[138]   S. Huang, L. Dai, and A. Mau, Physica B, 336–338 (2002).

[139]   F. L. Deepak, A. Govindaraj, and C. N. R. Rao, Chemical Physics Letters **345**, 5 (2001).

[140]   F. L. DEEPAK, A. GOVINDARAJ, and C. N. R. RAO, journal of chemical science **118**, 9 (2006).

[141]   P.-X. Hou, S. Bai, C. Liu, et al., Carbon **41**, 2477–2480 (2003).

[142]   J. Li, C. Papadopoulos, and J. Xu, Nature **402**, 253 (1999).

[143]   C. Papadoupoulos, A. Rakitin, J. Li, et al., Physical Review Letters **85**, 3476 (2000).

[144]   C. Papadopoulos, A. J. Yin, and J. M. Xu, Applied Physics Letters **85**, 1769 (2004).

[145]   Y. C. Sui, D. R. Acosta, J. A. Gonzalez-Leon, et al., Journal of Physical Chemistry B **105**, 1523 (2001).

[146]   L.-B. Kong, Solid State Communications **133**, 527 (2005).

[147]   O. T. Heyning, P. Bernier, and M. Glerup, Chemical Physics Letters **409**, 43 (2005).

[148]   J. F. AuBuchon, L.-H. Chen, C. Daraio, et al., Nano Letters **6**, 324 (2006).

[149]   G. E. Scuseria, Chemical Physics Letters **195**, 534 (1992).

[150]   L. A. Chernozatonskii, Physics Letters A **170**, 37 (1992).

[151]   L. A. Chernozatonskii, Physics Letters A **172**, 173 (1992).

[152]   V. I. Merkulov, A. V. Melechko, M. A. Guillorn, et al., Applied Physics Letters **79**, 2970 (2001).

[153]   S. Tsai, C. Shiu, W. Jong, et al., Carbon **38**, 1899 (2000).

[154]   G. W. Ho, A. T. S. Wee, and J. Lin, Applied Physics Letters **79**, 260 (2001).

[155] J. H. Park, S. B. Sinnott, and N. R. Aluru, Nanotechnology **17**, 895 (2006).

[156] H. Xu, Nature Materials **4**, 649 (2005).

[157] P. R. Bandaru, C. Daraio, S. Jin, et al., Nature Materials **4**, 663 (2005).

[158] J. Park, C. Daraio, S. Jin, et al., Applied Physics Letters **88**, 243113 (2006).

[159] G. S. Duesberg, I. Loa, M. Burghard, et al., Physical Review Letters **85**, 5436 (2000).

[160] A. Mews, F. Koberling, T. Basche, et al., Advanced Materials **12**, 1210 (2000).

[161] A. M. Rao, S. Bandow, E. Richter, et al., Thin Solid Films **331**, 141 (1998).

[162] C. Stephan, T. P. Nguyen, B. Lahr, et al., Journal of Materials Research **17**, 396 (2002).

[163] Q. Zhao, M. D. Frogley, and H. D. Wagner, Polymers for Advanced Technologies **13**, 759 (2002).

[164] H. Y. Yu, S. H. Jhang, Y. W. Park, et al., Synthetic Metals **121**, 1223 (2001).

[165] X. Zhang, W. Zhang, L. Liu, et al., Chemical Physics Letters **372**, 497 (2003).

[166] H. Kataura, Y. Kumazawa, Y. Maniwa, et al., Synthetic Metals **103**, 2555 (1999).

[167] X. Zhao, Y. Ando, L.-C. Qin, et al., Chemical Physics Letters **361**, 169 (2002).

[168] Y. Ando, X. Zhao, H. Kataura, et al., Diamond and Related Materials **9**, 847 (2000).

[169] S. K. Doorn, L. X. Zheng, M. J. O'Connell, et al., Journal of Physical Chemistry B **109**, 3751 (2005).

Chapter 3 Materials and Experimental techniques

3.1 Introduction

This chapter aims to describe the main experimental procedures used in this thesis. These fall into two broad categories; materials synthesis, and experimental techniques. The first section of this chapter will provide an overview of the specific substrates used, sample preparation and general CVD preparation techniques. A more detailed examination of the specific growth parameters for different morphologies and geometries for CNT growth will be covered in chapters 5 and 6. The microscopic and spectroscopic techniques used will be discussed in sections 3.3 and 3.4 respectively.

3.2 CNT synthesis

3.2.1 Substrates

Carbon nanotubes (CNTs) can be grown on a large variety of substrates and support matrices. Almost any material that can support the catalyst metal, and is able to withstand the temperatures necessary for CVD can be used as a substrate.

CNTs were successfully grown on porous alumina membranes (PAMs). The PAMs (Figure 3-1) used for these experiments were prepared by anodising aluminium foil (99 %, Goodfellows) in polyprotic acids at 0°C using a lead plate as cathode.[1, 2] The anodising voltage was kept constant (at 80V) and controls the pore diameter (approx. 1.2nm per Volt) and the pore density. 10 % sulphuric acid is used for anodising voltages up to 20 V, 1 % oxalic acid was used for anodising voltages from 20 to 80V and 1% phosphoric acid was

used above 80 V. Prior to the anodisation, the aluminium foil is cleaned in a solution of 48 g/l $K_2Cr_2O_7$ in 10 % phosphoric acid at 80°C and subsequently electro-polished in a 11:7 mixture (v/v) of concentrated phosphoric and sulphuric acids at 70-75°C. The resulting nanoporous alumina templates were filled with $Fe^{3,4}$ by an AC electro-plating procedure at a voltage of 16V.
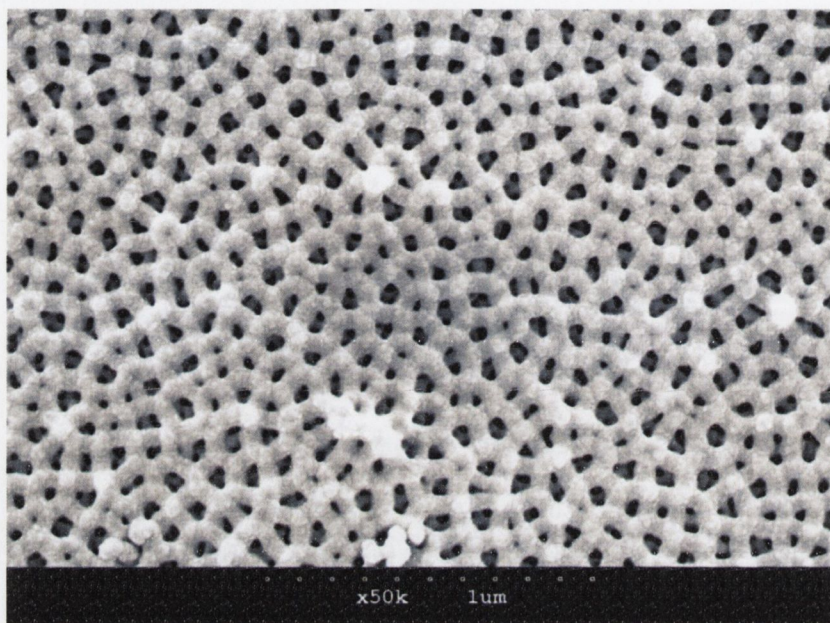
Figure 3-1 SEM micrograph showing the surface of a PAM substrate before CVD growth.

The samples were introduced into the CVD chamber and the system evacuated within minutes of Fe filling. In the event that the Fe-filled PAM could not be immediately introduced into the evacuated chamber, they were stored in a vacuum desiccator in the interim. These precautions were taken in order to avoid large amounts of oxidation of the catalyst metal.

The PAMs are received as circular membranes roughly 2 cm in diameter enclosed by a square frame of aluminium. These membranes are carefully removed from the frame using a scalpel. The freed membrane is sectioned into smaller pieces of <1 cm dimensions. These sections are loaded into a ceramic boat or a specially designed stainless steel clamp, and loaded into the furnace tube. The CVD procedure is carried out as normal. However, great care was taken on both gas introduction and system venting to insure that the very flimsy membranes were not blown free of the boat.

A number of mesoporous silica samples incorporating different concentrations of either iron or cobalt catalyst were received from Prof Spalding's group in UCC. A mesoporous material contains uniform pores in the order of 2 to 50 nm in diameter. The samples were prepared by the supercritical CO_2 method: hexagonal mesoporous silica was

prepared from a mixture of tetramethoxy silane, aqueous hydrochloric acid a Pluronic surfactant.[5, 6] Iron oxide Fe_3O_4 was incorporated into the mesoporous silica powder by degrading $[Fe_3(CO)_{12}]$ in supercritical carbon dioxide (sc-CO_2). Cobalt was incorporated by the use of $[Co_2(CO)_8]$ as a precursor.[7]

Carbon nanotubes were grown on several non-porous substrates. Silicon is one of the most common substrates as it is readily available and can be obtained with highly polished surfaces that are easily patterned. Silicon substrates are heavily used in the semiconductor industry[8] and thus are popular with CNT growth due to the possibility of integration of in situ grown tubes into current IC chip architectures.

Several CVD experiments grew dense forests of MWNTs on plain, polished silicon substrates with a native oxide layer. The substrates were cleaved into square pieces roughly 1 cm a side from larger wafers using a diamond scribe.

All of the trench growth optimisation work featured in Chapter 6 was carried out on silicon segments with a test card patterned pre-etched into the surface. The patterns contain a variety of both square and trench designs etched into the surface of the wafer. These segments were further cleaved into smaller segments with a diamond scribe.

Further trench etched silicon wafers were received from Tyndall National Institute as part of their NAP 9 open access programme.[9] The silicon wafers were received pre-cut with a diamond saw into 5 mm^2 pieces with a square region (15 mm a side) at the centre. This region contains a set of trenches of one of a particular width etched to a depth of 300 nm. There is an un-etched section of silicon substrate ~1 μm wide between each trench. The trench widths on any section are of one of the following widths: 120, 170, 240, 300, 400, 500 nm (Figure 3-2).
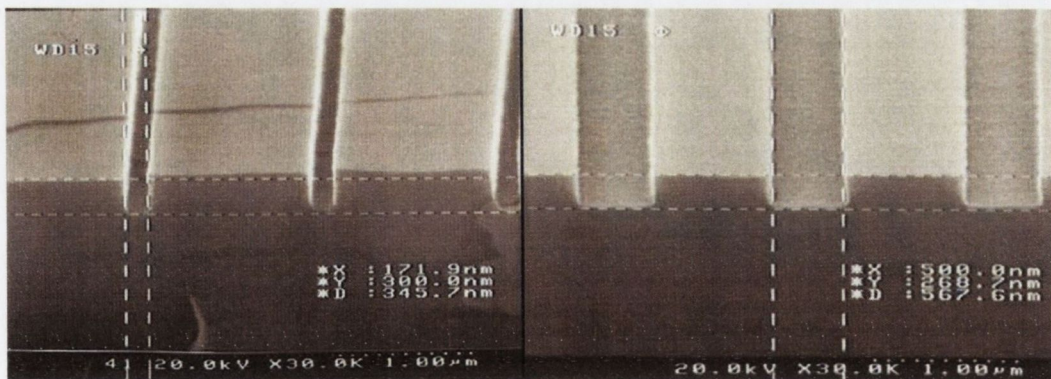
Figure 3-2 SEM micrograph showing trench edge of a cleaved edge of etched region of 170 nm (left) and 500 nm (right).

Nanotubes were grown on several test-chip die arrays received from Intel®. The test-chips consist of trench arrays of differing geometries with a variety of widths ranging

from <200 nm to several microns and trench depths ranging from 160 – 300 nm (Figure 3-3). The trenches are etched into a silicon nitride layer on a silicon wafer. The wafers were cleaved by hand using a diamond scribe into sections of between two to six die in size.
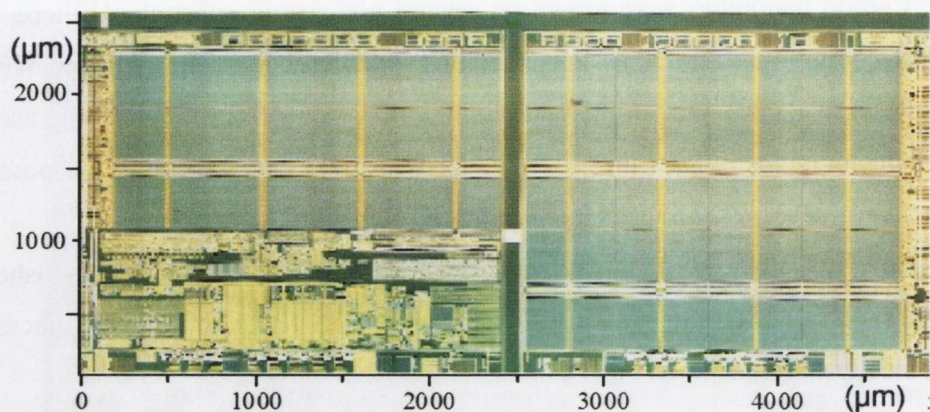
Figure 3-3 Optical micrograph of a single Intel® test-chip.

Silicon nitride (SiN) membranes (Figure 3-4) obtained from SPI supplies were also used as substrates for tube growth. These membranes were acquired as 0.5 * 0.5 mm windows in a silicon frame with a diagonal length of 3 mm that fits neatly into the TEM sample holder. The membrane thicknesses were given as 20, 50 and 100 nm allowing CVD grown CNTs to be examined in-situ with techniques such as TEM. The membranes were obtained both as either continuous or perforated windows. The perforated windows have roughly circular holes that are 2 μm in diameter on 4 μm centres. The solid membranes were etched using the FIB system to produce small arrays of slits of similar dimensions to the trenches used in the Si wafer systems used.
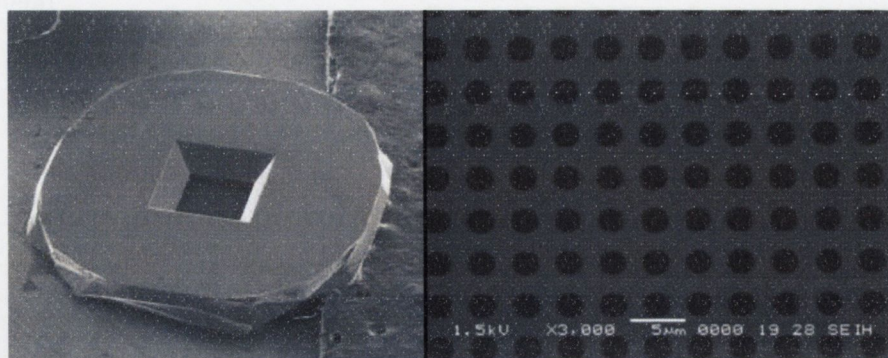
Figure 3-4 SEM image of A) SiN membrane in Si frame B) high magnification image of perforated membrane. Image courtesy of SPI. [10]

3.2.2 Catalyst metal

Iron catalyst was applied to the surface of the silicon substrates by dropping a catalyst solution from a glass pipette and allowing them to dry in a laminar flow hood at room temperature. A solution of block co-polymer: polystyrene-polyvinylferrocene (PS-PVF) in toluene was used. The PS-PVF was anionically synthesized in-house,[11] and characterized by Nuclear Magnetic Resonance and Gel Permeation Chromatography to determine its iron content (2.1%).

A separate method of catalyst deposition involves direct deposition by evaporation of iron wire. 1 cm^2 sections of silicon cleaved from a wafer served as substrates. The sections were either completely or partially covered in aluminium foil. This foil was pierced in several places with a pin to allow the iron to form a variety of island sizes. The wrapped and partially wrapped silicon sections are loaded into a tray that holds up to 16 sections. The tray is placed in the evaporator and pumped down to a pressure below 10^{-5} mbar. A 1 – 2 cm section of iron wire was balled up and loaded into a high tension tungsten basket. When the desired chamber pressure was reached the current through the tungsten basket was increased until the iron wire melted and evaporated. The samples were exposed to the evaporating iron until a 15 nm layer had deposited on the surface. This thickness of the deposited layer was originally measured using a crystal thickness monitor, subsequent deposition were controlled by deposition time.

3.2.3 CVD treatment

The design and construction of the custom-built CVD system will be discussed in detail in chapter 4. In this section the general method for CVD growth of nanotubes will be given.

The furnace-tube of the CVD system can accommodate any solid substrate up to 2 cm wide and 10 cm long (see section 4.2.1, Figure 4-5). Solid substrates were cut into squares of roughly 1 cm a side. Samples were placed in ceramic furnace-boats prior to insertion into the furnace-tube. Any substrate that was too large to lie flat on the bottom of the boat is loaded so that it leaned to one side so that the surface with deposited catalyst faced towards the acetylene inlet.

The samples are loaded into the boat and pushed into the furnace-tube so that it sits at the centre of the heated zone. This position is marked by the location of the furnace's inbuilt thermocouple. The position is also marked on the hooked rod used to push the boat into place. On occasions when two boats were used they were positioned either side of the central mark. The maximum sample separation was less than 5 cm either side of the central mark, so that the samples remained in same temperature zone (see Chapter 4, Figure 4-5)

When the sample was in place, the CVD chamber was sealed and pumped down for approximately 20 minutes to 10^{-3} mbarr using a mechanical rotary vein pump. The mechanical pump is allowed to run for the entirety of the CVD treatment. The chamber is then flooded with argon in order to remove remaining oxygen from the system. Argon is allowed to flow for approximately 5 minutes before heating is begun. Argon flow is continued at an even rate for the entire CVD run. Once the system has been flushed with argon the furnace set-point is adjusted to the desired working temperature. The system is then allowed to heat directly to the desired the working-temperature.

When the required temperature is reached the system is allowed to sit for five minutes to allow the temperature of the entire system to equilibrate before the acetylene flow is started. The acetylene is allowed to flow for the desired amount of time (usually 60 minutes) and is then stopped. The system is kept at the operating temperature for 5 minutes before cooling in order to allow for any remaining acetylene to be removed from the system. When cool-down begins the set-point is set to room temperature, and the furnace is opened so that the heated section of the furnace-tube is exposed to ambient temperature.

On reaching room temperature, the argon flow is stopped, the pump is switched off and the system is gently vented to atmospheric pressure, whereupon the chamber is opened and the furnace boats are carefully removed.

Some sample types require some alterations to standard procedure. For example, when growth is being carried out on the silicon nitride (SiN) initial heating to the desired temperature is carried out in steps of 50°C with a 10 minute equilibration in between each step. This precaution is taken in order to minimise the thermal stressing on the SiN windows and prevent them from snapping.

When powdered samples, such as mesoporous silica are used care must be taken so that the powders are not blown out of the boat. To this end, the samples are cooled after the CVD treatment without splitting the furnace. When the furnace is split open the top of the furnace tube is exposed to ambient temperature while the bottom of the tube is still in contact with the heated surface. This sets up a convection current within the tube that can lift the powder out of the ceramic boat. Keeping the furnace closed does not allow these currents to be set up.

3.3 Electron microscopy

Electron microscopy is an important set of techniques for characterisation of CNTs. These methods allow the user to examine a visual representation of microscopic features of a

sample. Specifically important in this work were the techniques of scanning electron microscopy (SEM) and transmission electron microscopy (TEM). SEM allows the investigation of CNTs grown in-situ; enabling the measurement of individual MWNTs (length and diameter) and allowing for statistical analysis to be carried out on arrays of tubes to examine distribution factors. TEM in general has a higher resolution and allows the examination of individual and small groups of CNTs in finer detail. Such images can lead to a better understanding of CNT structure and interactions.

3.3.1 Transmission electron microscopy

The majority of TEM was carried out on a Hitachi H-7000 Scanning Transmission Electron Microscope (Figure 3-5), at typical accelerating voltages of ~ 100 Kv. Image magnifications of up to 500 K were obtained, with a quoted resolution of 0.5nm. Images are recorded digitally using a Megaview 2 CCD camera from SIS and saved in bitmap format. TEM was carried out on samples supported either on copper grids or SiN membrane windows.

Samples were prepared for TEM by dropping a CNT suspension onto a formvar coated copper grid with a cleaned glass pipette. The droplet is then left on the grid for a set amount of time (10 – 120 seconds) to dry. The suspensions were created by sonicating several substrates supporting CVD grown CNTs in a solvent such as methanol for several minutes.
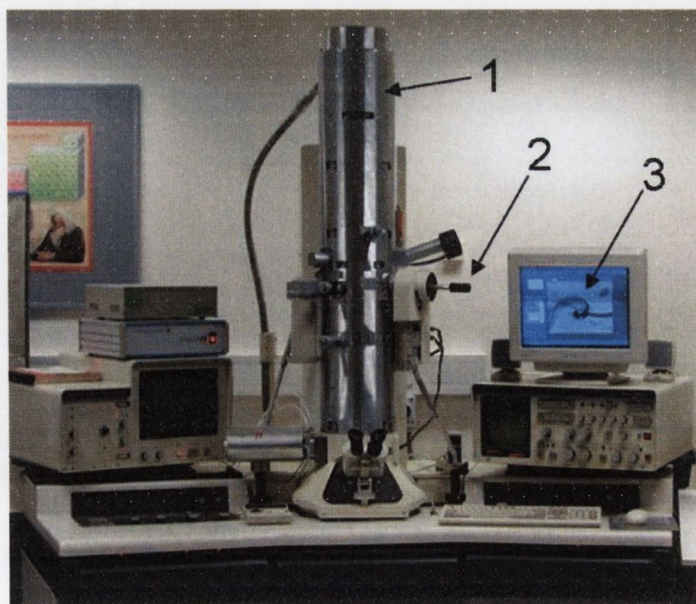
Figure 3-5 Hitachi H-7000 Scanning Transmission Electron Microscope. 1: column; 2: inlet port; 3: camera view screen.[12]

The SiN membranes discussed above were used in the TEM to study in situ grown CNTs without removal from their original growth substrate.

3.3.2 Scanning electron microscopy

SEM studies were carried out on a Hitachi S-4300 Field Emission Scanning Electron Microscope (Figure 3-6). Gold coated samples were investigated with an accelerating voltage of 20 kV and a beam current of ~ 10 μA. Un-coated samples were investigated with an accelerating voltage of 5 kV.

Gold coating is used to help prevent "charging" on surfaces that are not electrically conducting, such as silicon dioxide. This effect occurs when electrons from the microscope beam cannot be dissipated to earth, and thus "pool" on the nonconductive surface. This accumulated charge can then scatter lower energy secondary electrons, causing a loss in fine detail in the resultant image. A thin layer of gold deposited on the surface of the substrate can be earthed to allow the electrons left on the surface from the electron beam to dissipate.

The substrates were treated with a 5-10 nm sputter coated layer of gold. This can lead to a larger deviation in the diameter measurements. The thickness of the gold layers has been shown to be relatively consistent; however it is experimentally more correct to combine the maximum possible deviation with the variation error in measuring the diameter of the tube using analysis software.
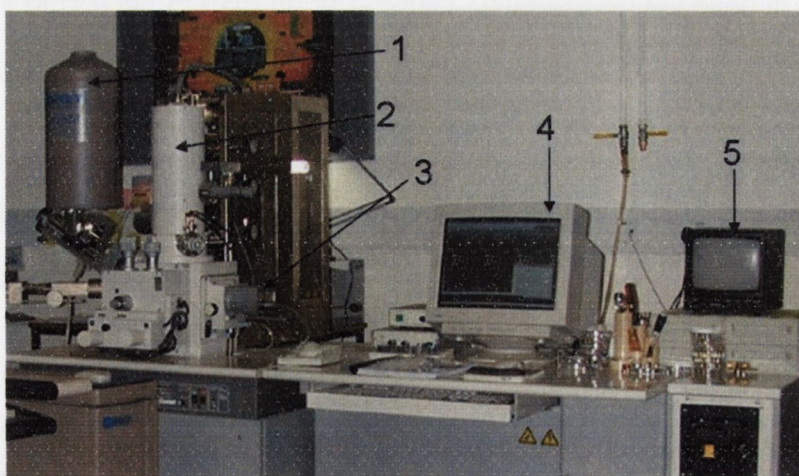
Figure 3-6 Hitachi S-4300 Field Emission Scanning Electron Microscope. 1: liquid nitrogen reservoir; 2: column; 3: Inlet port; 4: SEM camera display; 5: camera display from inside the chamber.[12]

3.3.3 Focused ion beam patterning

Focused ion beam (FIB) systems are similar to scanning electron microscopes but involve a rastering beam of ions as opposed to electrons. In a dual beam system the FIB column is normally mounted at an angle with respect to the vertical i.e. the SEM column. The ions are electric-field extracted from a liquid metal ion source[13, 14] (LMIS) which consists of a tungsten needle with a radius of curvature of 1 μm that is wetted by the liquid metal. The electric field results in the formation of a "Taylor cone" on the wetted tip from which the ions are extracted. The most commonly used liquid metal is Ga[14, 16] since it is liquid almost at room temperature, with a melting point of 29.8°C. This results in little interdiffusion between it and the tungsten needle. It has low surface energy, and therefore flows well through the W needle. Its low volatility at the melting point leads to a longer lifetime for the source. The Ga$^+$ ions are extracted from the LMIS and accelerated though a potential down the ion column.

A FIB system can also be used to deposit metals or insulators in user defined areas. Typically a gas precursor, such as an organo-metallic compound, is introduced to the chamber through an inlet capillary positioned just above the sample surface and close to the ion beam. The gas molecules adsorb on the sample surface around the inlet but only decompose when the ion beam hits them, and thus the deposition is in fact a form of CVD. The precursor gas is chosen so that it has sufficient sticking probability so that enough sticks to the sample surface; it must also decompose under the ion beam faster than it is sputtered away.

Electron beam deposition of materials can be used to produce very low energy deposition that will not affect the underlying surface as dramatically as the ion beam assisted deposition.[17] The electron beam can normally use the same gas injectors as the ion beam.[18-20] Lower beam voltages result in higher deposition rates;[18] this is attributed to the secondary electrons being mainly responsible for the deposition as opposed to the primary beam itself.

A FEI 235 Dual Beam system equipped with a Raith Quantum Lithography System was used for several functions in the characterisation and processing of the samples. The electron beam allows for both normal SEM imaging of samples and for the deposition of small amounts of Pt. The electron beam can be used to deposit Pt directly onto the CNTs without fear of implanting them with Ga$^+$ ions. The acceleration voltages used were normally 5 kV when imaging and 15kV when depositing.

The Ga$^+$ ion beam is used to deposit larger amounts of Pt on the surface of the sample, such as for intermediate contacts bridging those made with E-beam to larger

electrical contacts suitable for probe attachment. It is however possible to create small contact pads in the region of 100 μm^2 using the ion beam. These pads can then be connected to either through wire bonding or use of an electrical measurement rig with a microprobe station. The ion beam can be used without the Pt source to etch material from the surface of the substrate to cut through existing electrical contacts, breaking short circuits. It can also be used mill substrates such as the SiN membranes to create trench arrays. The ion beam was operated at currents of between 50 - 500 pA depending on size of deposition required and relative position to CNT structures of interest.

3.3.4 Image analysis software

All measurements and statistical analysis on the SEM micrographs were carried out using USCTA image tool 3. Some images were cropped for presentation using Arcsoft PhotoStudio 2000SE. This software was also used to centre the scale bar in micrographs. No further manipulation was carried out on the any electron micrographs shown in this thesis.

3.4 Spectroscopy

While microscopy techniques give a visual representation of the physical structure of a sample spectroscopy techniques measure electromagnetic radiation that is reflected or absorbed by a sample to give information such molecular bonding and elemental species present in the sample. In this section a description of each of the spectroscopy devices used will be given.

3.4.1 Energy dispersive X-ray spectroscopy

Energy dispersive X-ray spectroscopy is a simple and direct method of determining the elemental makeup of a sample. EDX in conjunction with low resolution SEM was used to was used on several occasions to locate and identify surface catalyst metal. The machine used was a Hitachi S-3500N Variable Pressure Scanning Electron Microscope used in back scatter mode with integrated EDX (Figure 3-7).
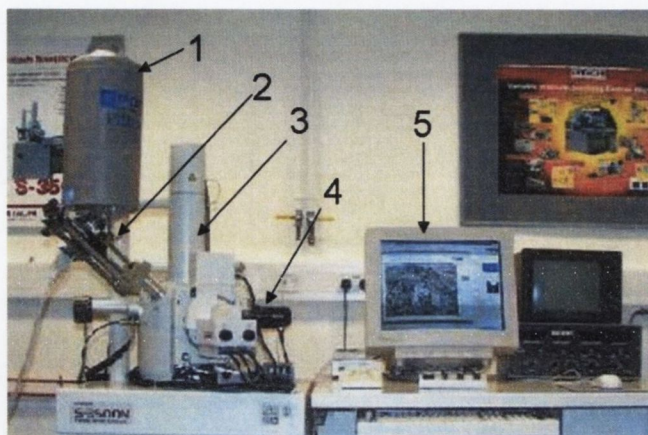
Figure 3-7 Hitachi S-3500N Variable Pressure Scanning Electron Microscope 1: liquid nitrogen reservoir; 2: EDX unit; 3: column; 4: Inlet port; 5: SEM camera display.[12]

3.4.2 Fourier transform infra-red spectroscopy

A Nicolet Nexus spectrometer was used to the IR spectrum of annealed and un-annealed CNTs (see section 5.4). The Nexus has a range from 450 cm^{-1} to 4000 cm^{-1} and with a resolution of 4 cm^{-1}. Samples of CNTs are prepared by making a < 1 % mix of CNTs in KBr and pressing a disc. The KBr/CNT disc is then measured in the transmission mode of the instrument.

3.4.3 Raman spectroscopy

Raman spectra were measured using a HORIBA Jobin Yvon labRAM HR. This is a bench top micro-Raman unit with a confocal microscope. It has an 800 mm focal length spectrometer giving it a quoted resolution of 0.3 cm^{-1}.

The microscope is fitted with a digital camera to allow for visual focusing on a sample surface. However the camera in conjunction with the mechanised stage can be used to take composite optical images (Figure 3-3).

For the majority of the work a 632.8nm HeNe laser was used. This type of laser is commonly used as it is close to resonant with the G-band of CNTs.

CNTs where generally measured in situ. In some cases however, CNT suspensions were drop cast onto simple glass microscope slides before further characterisations, such as TEM were carried out.

Where possible, at least five accumulations were taken and collection times varied between 5 – 300 seconds per accumulation.

Some of the initial Raman spectra were taken using an older HORIBA Jobin Yvon labRAM with a 300mm focal length spectrometer. Though this has a slightly lower

resolution, the same laser line was used (632.8 nm) so that spectra taken on either machine are directly comparable.

Each instrument has both a 600 and 1800 grating for medium and high resolution imaging. In general the 1800 grating was used; any use of the 600 grating will be mentioned in the text.

3.5 References

[1] C. A. Foss, G. L. Hornyak, J. A. Stockert, et al., Journal of Physical Chemistry **98**, 2963 (1994).

[2] A. Heilmann, F. Altmann, D. Katzer, et al., Applied Surface Science **145**, 682 (1999).

[3] T. A. Hanaoka, A. Heilmann, M. Kroll, et al., Applied Organometallic Chemistry **12**, 367 (1998).

[4] P. M. Paulus, F. Luis, M. Kroll, et al., Journal of Magnetism and Magnetic Materials **224**, 180 (2001).

[5] G. S. Attard, J. C. Glyde, and C. G. Goltner, Nature **378**, 366 (1995).

[6] N. R. B. Coleman and G. S. Attard, Microporous and Mesoporous Materials **44-45**, 73 (2001).

[7] T. A. Crowley, K. J. Ziegler, D. M. Lyons, et al., Chemistry of Materials **15**, 3518 (2003).

[8] http://www.intel.com/technology/silicon.

[9] http://www.tyndall.ie/nap/.

[10] http://www.2spi.com.

[11] E. Lahiff, C. Y. Ryu, S. Curran, et al., Nano Letters **3**, 1333 (2003).

[12] www.tcd.ie/cma.

[13] W. Czarczynski and Z. Znamirowski, Vacuum **44,** 1095-1099 (1993).

[14] V. G. Dudnikov, Review of Scientific Instruments 67, 915-920 (1996).

[15] J. C. Beckman, T. H. P. Chang, A. Wagner, and R. F. W. Pease, Journal of Vacuum Science & Technology B 14, 3911-3915 (1996).

[16] J. Melngailis, Journal of Vacuum Science & Technology B 5, 469-495 (1987).

[17] L. A. Giannuzzi and F. A. Stevie, Introduction to focused Ion beams (Springer, New York, 2005).

[18] S. Lipp, L. Frey, C. Lehrer, E. Demm, S. Pauthner, and H. Ryssel, Microelectronics and Reliability 36, 1779-1782 (1996).

[19] S. Lipp, L. Frey, C. Lehrer, B. Frank, E. Demm, S. Pauthner, and H. Ryssel, Journal of Vacuum Science & Technology B 14, 3920-3923 (1996).

[20] S. Lipp, L. Frey, C. Lehrer, B. Frank, E. Demm, and H. Ryssel, Journal of Vacuum Science & Technology B 14, 3996-3999 (1996).

Chapter 4 Chemical vapour deposition of carbon nanotubes

4.1 Introduction

This chapter will cover the use of chemical vapour deposition (CVD) both as a tool for the production of thin films and more specifically for the production of carbon nanotubes. A brief overview of the basics of CVD; its advantages and uses in industry will be given in the sections 4-2 – 4-4. The process of designing and building a research CVD system for the growth of carbon nanotubes will be discussed in section 4.5.

4.2 Basics of CVD

Chemical Vapour Deposition (CVD) is a crystal growth process used to deposit a wide range of conducting, semiconducting, and insulating materials. It has also been used to produce carbon fibres, filaments, and tubular carbon materials for many years.[1-3] CVD is a versatile process in which gas-phase molecules are decomposed into reactive species, leading to film or particle growth. A gas or vapour precursor is transformed into solids such as thin films, powders, or various structured materials inside a reactor (Figure 4-1). A basic CVD process consists of the following steps:

1) A predefined mix of reactant and inert gases are introduced into the reaction chamber;

2) The gas species move to the substrate;

3) The reactants get adsorbed on the surface of the substrate;

4) The reactants undergo chemical reactions with the substrate to form the film;

5) The gaseous by-products of the reactions are desorbed and evacuated from the reaction chamber.
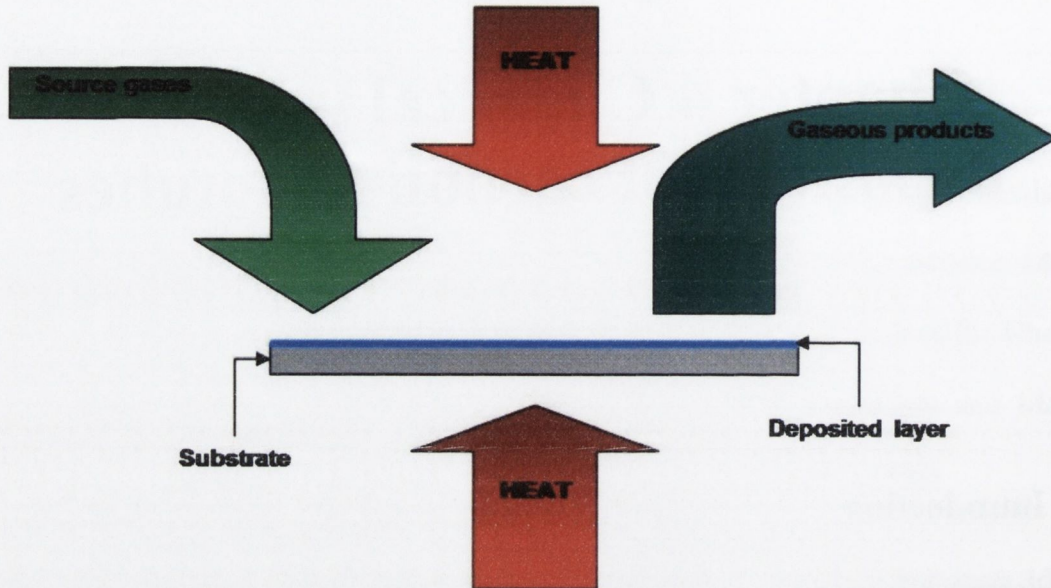
Figure 4-1 Illustration showing the general process of chemical vapour deposition.

Chemical vapour deposition is a commonly used technique both in research towards new devices and materials and in established industry. Due to its application in a variety of areas several variants have evolved, some of which are listed below:

4.2.1 Thermal activation (thermal CVD)

Thermal CVD is one of the most basic and commonly used forms of CVD. As the name suggests heat is used to activate a chemical reaction. This can be achieved by heating both sample and the active gases in a single or multi-stage furnace or simply by heating the sample with a heating filament. The active gas (such as acetylene or methane in the case of carbon nanotube (CNT) growth) is raised to a temperature whereupon it thermally decomposes on entering the heated section of the furnace (or makes contact with the heated substrate). The constituents of the decomposed gas then take part in the desired reaction, such as the catalyst enabled transformation of liberated carbon atoms into nanotubes. This form of reaction activation in CVD has the advantage of being very simple to set up and does not require use of additional processes as in plasma or laser enhanced CVD.

4.2.2 Atomic layer deposition (ALD)

ALD is a form of CVD that uses short pulses of gas and keeps the precursors separate during the reaction. These reactive gasses are pulsed into the substrate chamber and the system purged with an inert gas between pulses. Often two complimentary active species (such as ZnCl and H_2O) will be used in alternate pulses. Each precursor adsorbs until it saturates the surface, and the film cannot grow any further until the second gas is introduced. The self-limiting nature of this process adds a high degree of control. Through proper management of the conditions accurate uniform films a few angstroms thick are achievable over large areas.[4]

4.2.3 Low pressure (LPCVD)

Any CVD process that operates with the pressure in the reaction chamber at/or below atmosphere is either LPCVD or UHVCVD (ultrahigh vacuum is below 10^{-6} mbar). At these low pressures the mean free paths of the precursor gas molecules are large compared to the size of features on the sample surface. Therefore, under these conditions the process can be thought of as ballistic transport.[5] The high mean free path helps to reduce unwanted gas phase reactions and can help to improve control over, and quality of deposited film uniformity.

4.2.4 Laser-assisted (LACVD or LCVD)

LA-CVD involves the deposition of material by localised chemical reaction directed by a laser beam. The chemical reaction that occurs in this form of CVD can be pyrolytically activated by the thermal energy from the heated substrate. Or it can be photolytically activated by the changes in the electronic structure of the precursor material brought about by the photon energy of the laser. It has the advantage of operating at lower temperatures than standard thermally activated CVD; it also allows for patterned growth by manipulating the laser and growth of alternating layers from admixtures of gases. LA-CVD has produced CNTs using a continuous wave CO_2 laser to active a mixture of vaporised $Fe(CO)_5$, ethylene (C_2H_4) and acetylene (C_2H_2).[6]

4.2.5 Plasma enhanced (PECVD)

PECVD uses plasma within the reaction chamber; usually created between two charged plates around the substrate, to enhance the chemical reactions of the precursor species. PECVD is often used in the semiconductor industry as it allows the process to operate at lower temperatures; this also has advantages for CNTs, allowing them to be integrated into other devices.[7] Plasma enhancement in CNT production has been shown to help increase alignment[8] in CNT arrays and to promote the growth of semiconducting over metallic SWNTs.[9]

4.2.6 Metal-organics (MOCVD)

MOCVD uses metal-organics (i.e. compounds containing one or more direct metal–carbon covalent bond) as the precursor. Examples of materials produced by MOCVD include GaAS used in light emitting diodes (LEDs), InGaAsP in fibre optic communications, PbSnTe used in infrared detectors and InAlGaN used in blue LEDs.[10] The advantage of using organometallic precursors is that deposition can occur at lower temperatures (~500°C) than with other substitutes such as halides, however organometallic compounds tend to be more expensive with the added disadvantage of being highly reactive and hence difficult to purify.

There are several other more subtle variations on CVD and its variants; such as Microwave plasma-assisted CVD (MPCVD), Rapid thermal CVD (RTCVD), and Remote plasma-enhanced CVD (RPECVD) but they are beyond the scope of this overview.

CVD has been used extensively to synthesize high quality CNTs either with bulk supported catalyst or directly on substrates. Typically, the process consists of dissociation of a carbon feedstock, interaction with catalytic particles, and growth of the nanotubes. The substrate is exposed to one or more volatile precursors, which react and/or decompose on the substrate surface to produce the desired deposit. Frequently, volatile byproducts are also produced, which are removed by gas flow through the reaction chamber. As well as the ease of producing clean, good quality CNTs there are several other advantages to CVD both as a general technique and specifically for producing CNTs.

4.3 The role of catalyst in CVD carbon nanotube growth

The exact role of the catalyst particle in the growth mechanism of carbon nanotubes is still debated. However, it would appear that the size of the metal island does have an effect on

its role in the growth process. In smaller metal islands, a few nm in diameter, the carbon atoms are not dissolved into the body of the particle but instead stay on the surface of the catalyst particle. Hoffmann et al suggest that it is energetically favourable for hydrocarbon feedstock molecules such as C_2H_2 to disassociate on surface of a small heated catalyst island.[52] The released carbon atoms then diffuse across the surface without needing to be dissolved into the bulk.

However, in larger particles of more than ~5 nm in diameter[52] the carbon atoms are dissolved into the bulk of the metal forming a metal-carbide solution.[54-56] Carbon atoms diffuse through the interior of the metal particle, mainly due to the existence of a concentration gradient along the diffusion path.[57, 58] Formation of carbon-metal eutectic alloy enhances the diffusion of carbon in the metal alloy, initiating carbon aggregations which act as a nucleation seed for nanotube growth.[59]

Supersaturation of the solution arises from a temperature gradient within the particle.[60] There is however some evidence that a temperature gradient is not necessary for such a saturation to occur. Within a metal particle the C-C separations are larger than that of graphite and the interaction is quite weak and slightly repulsive (-0.05 – 0.01 eV).[62] Calculations using density functional theory (DFT) show that it is more favourable for carbons to dissolve into a catalyst metal cluster (such as Ni) and coordinate with up to eight metal atoms than to remain on the surface at the initial stages.[61] However, the absorption capacity of such a metal island is finite, and, as the carbon density within it increases the rate of dissolution decreases until the metal solution is saturated. At this point no more carbon dissolves; all the new catalysed carbon precipitates on the surface.

Once the carbons have diffused to the surface of the metal particle the process for both large and small islands appears to be relatively similar. The nucleation of a closed-cap over a flat surface is energetically favourable compared to any other structure with dangling bonds or to a fullerene-type structure.[63] Carbon atoms that precipitate onto the surface of the metal catalyst can form chains, however these chains are too tightly bonded to the surface to break free.[61] Dimers are formed first, and then short chains, which eventually interconnect so as to form a sp^2-bonded graphene sheet. Molecular dynamics studies show that such sp^2 bonded carbon sheets "float" on top of curved catalyst surface due to the weak interaction between the graphene and the metal (such as iron).[64] Carbon atoms still covalently bonded to the catalyst hold the tube walls in place. Similar calculations carried out with gold as the metal reveal that once C dimers or chains are formed they tend to leave the catalyst surface because the interaction is not strong enough

to allow for graphene fragments to form. Following from this there is no time for a closed structure to form before falling free of the gold particle.

4.4 Advantages of CVD

In general, CVD has the ability to synthesize films of widely varying stoichiometry and to deposit uniform thin films of materials, even onto non-uniform shapes.

CVD allows a large degree of control over growth conditions, such as active gas type, reaction temperature, as well as flow rate and time. This allows the user to tune the properties and even the type of CNT produced. Choice of active gas and reaction temperature can affect whether the majority of tubes produced are singlewall (SWNT) or multiwall (MWNT) carbon nanotubes. For example using acetylene at relatively low temperatures will yield a majority of MWNTs whereas methane combined with higher temperatures will yield mostly SWNTs. Flow time combined with the particle size of the catalyst metal can be used to control the length and diameter of the CNTs.[11]

The choice of substrate allows for a huge degree of versatility. CNTs can be grown on almost any substrate that can withstand the reaction temperatures and support the catalyst metal. Porous substrates such as porous alumina membranes[12-18] and mesoporous silica[19-23] can be used to template arrays of tubes. The location of tube growth can be directed through lithographic patterning of the catalyst metal on the substrate[24-27] and the patterning of the substrate itself as in the case of Si/SiO_2 substrates.[22] The direction and orientation of tube growth can be influenced by external electric fields[8,28] and to a lesser extent by substrate geometries.[22,27,29,30] The high degree of control over CNT type and position allows for the possibility of in situ grown devices[7,29,31-36] that require little or no additional post production handling.

As material deposition technique CVD allows for the syntheses of materials of a closely controlled purity through the use of very high purity reagents. With CVD it is possible to produce CNTs with a very low amount of amorphous carbon as compared with other techniques such as the arc discharge method. The nature of CVD allows for a high degree of scalability from small bench-top rigs to industrial scale production units.[37] Overall; CVD as a CNT production method provides the versatility required for research while allowing for the possibility of mass production.

4.5 CVD in Industry

The first recorded use of a CVD process was for the preparation of carbon black as a pigment[38] and the first large scale use of CVD was used in improving fragile carbon filaments used in electric lights.[39,40] Today, CVD techniques are widely used throughout industry and academic research.

CVD can be used for a wide variety of applications from the fabrication of microelectronic devices[10,41,42], deposition of protective coatings, to the production of materials such as diamond[43-47] and, of course the growth of nanotubes.[35]

Nowadays CVD is an integral part of integrated circuit (IC) manufacturing and semiconductor device processing in general. The CVD processes used in industry tend to be for purposes and of complexities beyond the scope of this review. Rather, a brief overview is given here to give an idea of the contextual relevance of work undertaken in this project.

One of the most basic uses of CVD in the semiconductor industry is to cover a doped silicon wafer with a uniform layer of epitaxial silicon that can separate the original layer from additional circuit layers above it. Silicon dioxide is, of course, the dielectric material of choice for the microelectronics industry.[10]

Similarly, CVD is used to deposit metals, such as W, Mo, Pt Al, and Cu as interconnects filling in vias between stacked layers. CVD is also used to deposit connections between the source and drain of transistors.[48] Gate electrodes are often made from CVD deposited layers of polycrystalline silicon, or poly-silicon thin films. Other applications of thin films are the use of amorphous silicon in solar photovoltaic devices, epitaxial SiGe in high speed electronic devices and epitaxial GaAsP in light emitting diodes.[10]

4.6 Building a CVD system

4.6.1 Design philosophy

The decision to design and build a custom-made CVD system was based on both economic factors, and the desire to have a compact bench-top apparatus (Figure 4-2). The focus of the apparatus design was affected by the need for the system to be flexible and versatile. The academic research environment in which the device was to be operated required that it be adaptable, easy to use, modify, and upgrade. It was also necessary that it be robust

enough to tolerate multiple users. Also kept in mind during the design phase was the concept of using components whose spare parts and consumables were cost effective, easily sourced and, where possible, compatible with those of surrounding equipment (Figure 4-3)

4.6.2 CVD components

With the above philosophy in mind a bench-top thermal CVD system was designed. There are several necessary elements required for such a setup. These elements can be divided into several categories:

Gas inlet system

In order for any reaction to take place the reactant gases must be delivered to the sample substrate in the heated zone of the reaction chamber. The gas inlet system encompasses the components used to direct the gases (acetylene and argon) into the reaction chamber. In the case of each gas it was directed though metal tubing (either stainless steel or copper) through a valve protected mass flow controller (MFC) into the reaction chamber.

Gases, regulators and piping

An inert carrier gas is used to help disperse the active precursor gas during CVD. Argon was chosen for its cost and the ready availability of high purity stock (99.998%). As mentioned above argon is substantially heavier than air and thus can help in literally pushing remaining oxygen from the system. A dual stage regulator fitted with an additional needle valve as an initial step-down in pressure was fitted to the Ar tank. The acetylene line was connected to the corresponding MFC via a dual stage regulator using stainless steel tubing rather than copper tubing which not is compatible with acetylene[49,50] (Figure 4-4, item 2).

The mass flow controllers

The accurate control over flow rates of individual gases afforded by mass flow controller units (MFCs) makes them a highly desirable addition to an experimental CVD system (Figure 4-3, items 2 & 12, and, Figure 4-9, item 4). The MKS 1479 MFC units are controlled by a central controller (MKS digital supply and readout type PR4000A) and are quoted by the manufacturer as being able to control gas flow rate with an accuracy of ± 1% and a repeatability of 0.2%.
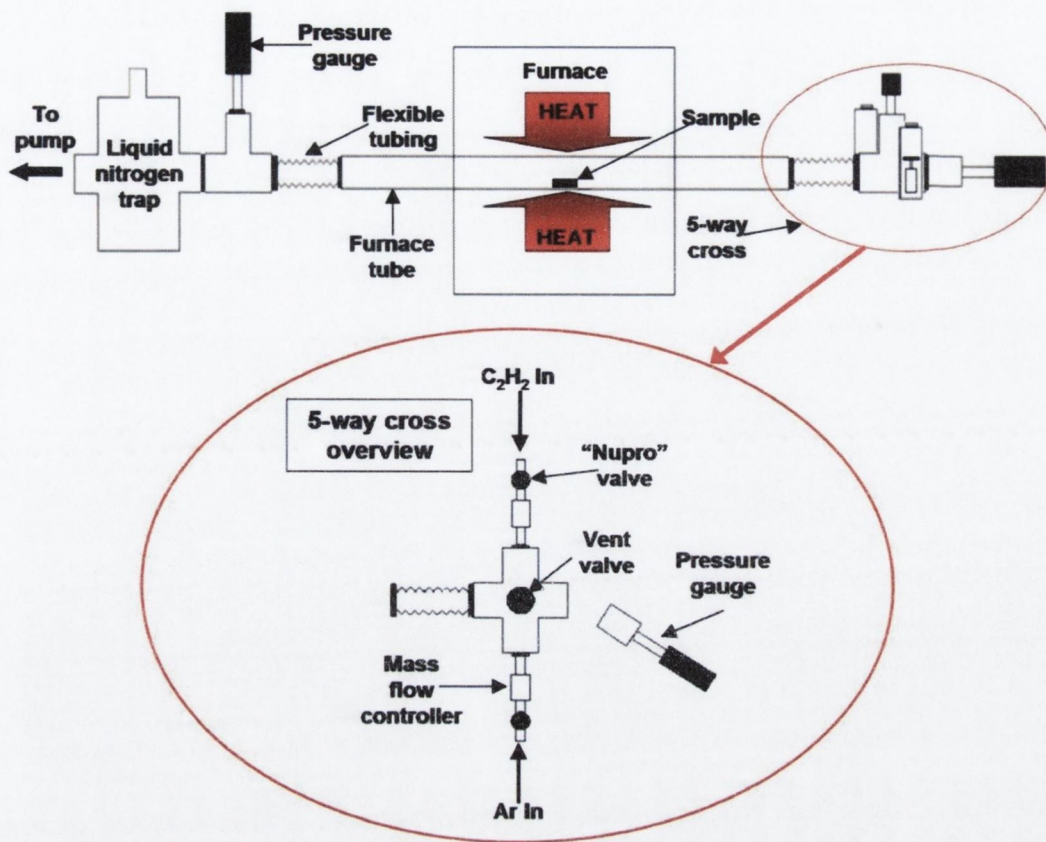
Figure 4-2 Schematic showing the original design for the custom built CVD system.
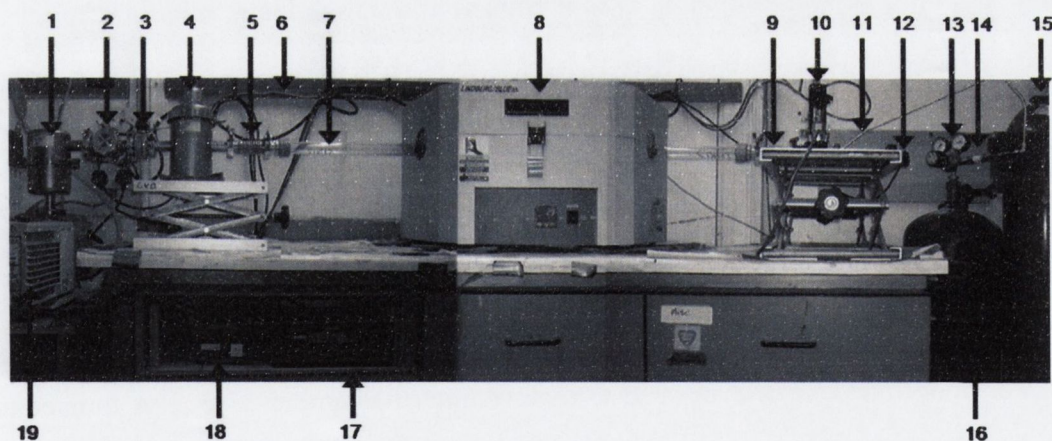
Figure 4-3 Image of the custom built CVD system comprised of 1: Molecular sieve trap; 2: 4-way cross with pressure gauge 1(not in view); 3: system isolation valve; 4: liquid nitrogen cold-trap; 5; flexible connector; 6: lead rack; 7: furnace-tube; 8: furnace; 9: lab-jack; 10: mass flow controllers; 11: stainless steel tubing of acetylene line; 12: pressure gauge 2; 13: Acetylene regulator; 14: flashback arrestor; 15: argon cylinder; 16: acetylene cylinder; 17: mass flow controller readout; 18: pressure gauge readout; 19: pump.

The first of the two MFCs fitted to the CVD has a quoted range of 10 – 5000 standard cubic centimetres per minute (sccm) and is fitted with corrosive resistant o-rings suitable for use with acetylene. The second MFC has a quote range of 100 – 50000 sccm and is suitable for all non-volatile gases.

An MFC operates by combining an electronic thermal sensor with a highly sensitive solenoid proportioning control valve. The whole device is packaged in metal seals to eliminate permeation of ambient gases into the device.
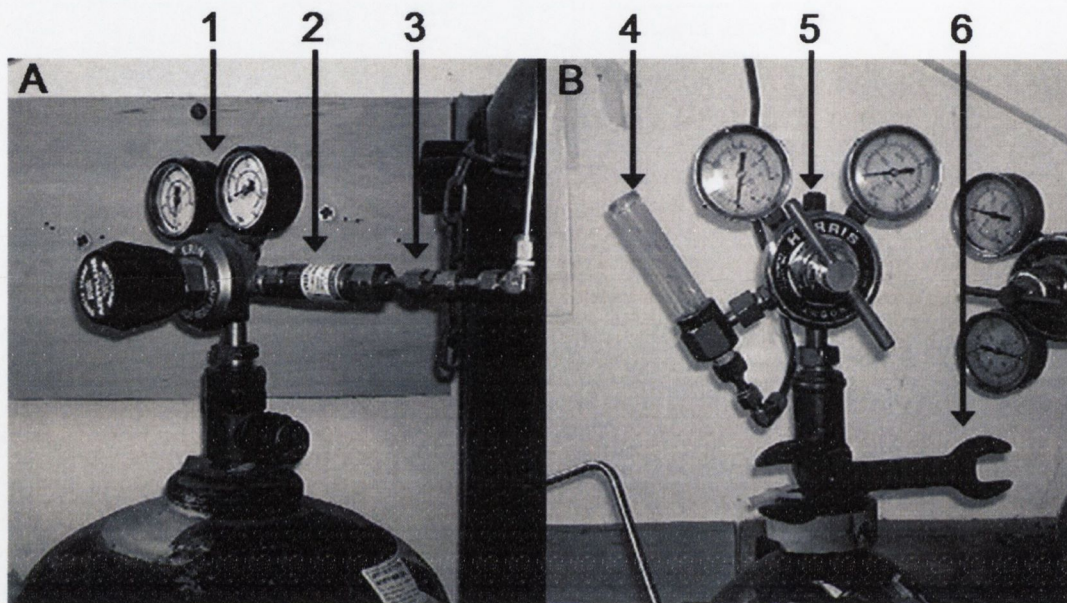
Figure 4-4 A: regulator setup for the acetylene tank. 1: dual-stage regulator; 2: flashback arrestor; 3: swagelok fittings. B: regulator setup for the argon tank. 4: ball flow meter; 5: dual-stage regulator; 6: cylinder wrench.

Reaction chamber

In order for CVD to take place the precursor gases must be brought into contact with the sample substrate under the correct conditions. For thermally activated CVD this requires a closed chamber that can be evacuated to remove unwanted ambient gases. A furnace-tube with stainless steel fittings connecting it to both the inlet and outlet systems fulfilled this function.

In order for the reaction to take place the chamber must also possess the means to heat the system to the temperature required for thermal activation of the desired reaction. A horizontal tube furnace encases the central section of the furnace-tube. This allows the contents of the tube in that section (namely the sample substrate and the reactant gases) to be heated to the desired reaction temperature.

The furnace

A Linberg-Blue M Mini-mite horizontal tube furnace (Figure 4-3, item 8) was chosen as the cornerstone of the build design. The Mini-mite has a footprint of 29.2 * 40.6 cm allowing a compact bench-top apparatus to be built around it. The furnace has a heating range up to 1100°C allowing for the CVD operate at a wide range of temperatures. The active heating length of the Mini-mite is 25cm and the diameter of the internal cavity is 2.5 cm.

In order to ascertain the effect of position of the sample within the reaction chamber a simple calibration was carried out (Figure 4-5). The furnace set-point was put to 710°C and temperature inside the inserted furnace-tube was measured with an external thermocouple. The furnace uses an internal thermocouple mounted at the centre of its heated length to measure its temperature relative to the set-point. Within two minutes of the set-point being achieved by the furnace the temperature in the furnace-tube was also seen to be stable at the set-point temperature according to the external thermocouple.

It was found that the temperature inside the furnace-tube varied by less than 5°C from the set-point temperature within 10cm of the centre of the furnace. Subsequently during the running of the CVD system, the temperature of any sample placed at the centre of the furnace was taken to be that of the furnace readout.
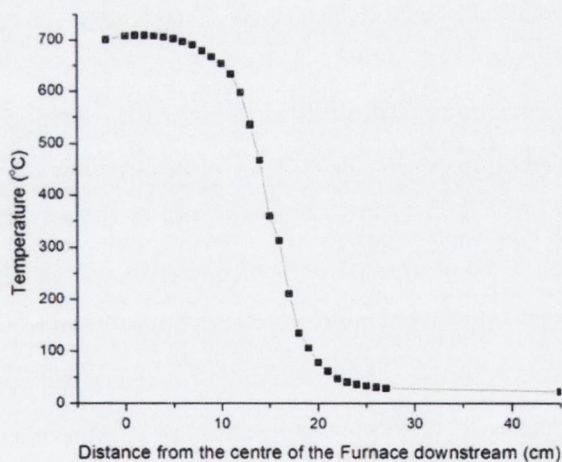
Figure 4-5 Change in temperature of the inside of the furnace-tube with respect to distance from the centre of the furnace.

The furnace-tube

A 1000 cm ceramic furnace-tube (98% Al_2O_3) was fitted through the furnace (Figure 4-3, item 8). This furnace-tube has an outer diameter (OD) of 21 mm and an inner diameter (ID) of 18 mm allowing it to fit snugly into the Mini-mite tube furnace and to accept samples of size ~1 cm*1 cm mounted in combustion boats.

The open ended tubes were fitted with specially machined NW25 weld-ring flanges so that they sat flush over the ends of the tube. The flanges were held in place and made gas tight with a high temperature epoxy (Epox-EEZ) (Figure 4-6). Any leaks that formed around this seal were easily repaired with that addition of either Epox-EEZ or standard vacuum glue to the affected area. It was found that adding a generous amount of silicone vacuum grease over the seals helped prevent any minor leaks.
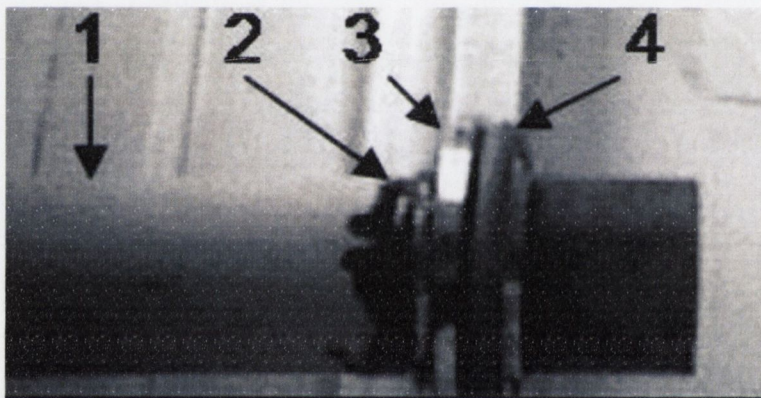
Figure 4-6 1: alumina furnace-tube; 2: Epox-EEZ high temperature epoxy; 3: custom machined NW25 weld ring flange.

In order to ensure that temperature at the ends of the furnace-tube would not rise above the tolerance of the epoxy seals (260°C) a simple test was carried out. The furnace temperature was set to 800°C. Argon flowed though the furnace-tube at 1000 sccm under normal operating conditions, which the exception of acetylene (which was not flowed into the system). The temperature and gas flow were held stable for two hours after the furnace stabilised at 800°C. The temperature of the outside of the exposed sections of the furnace-tube was measured at several points at regular time intervals both upstream and downstream using a thermocouple.

After two hours the surface temperature of the furnace-tube on the upstream side showed only slight increase in temperature (<15°C) above ambient; even within a few centimetres of the furnace housing.

On the downstream side of the furnace the heating was more pronounced. Figure 4-7A shows a plot of temperature of the furnace-tube with respect to distance from the

edge of the furnace housing (0 cm) out to the downstream fittings (45 cm). It can be seen that even after long heating periods the temperature drops off rapidly with distance. It should also be noted that only regions of the furnace-tube within a few centimetres of the furnace rose above 100°C during two hours of heating. Figure 4-7B shows a plot of temperature with respect to time. It can be seen here that after an initial jump in temperature on the introduction of the gas, the increase in temperature continues at a much slower rate. It is obvious from this plot that the temperature at the downstream fittings is unlikely to approach the epoxy temperature tolerance, even after extended periods of time. From these tests it was deemed that there was no risk of thermal degradation in the furnace-tube end seals.
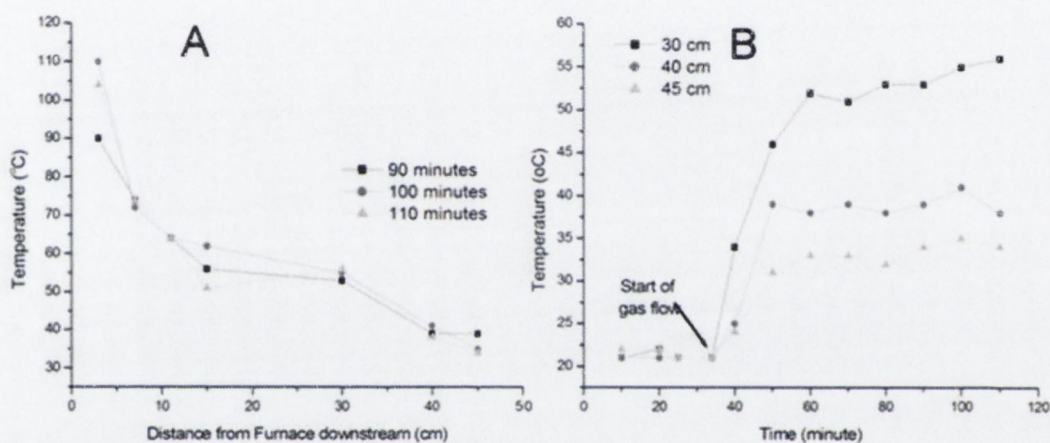
Figure 4-7 A: the temperature of the furnace-tube surface at different distances downstream from the furnace housing and B: the change in surface temperature of the furnace-tube over time while the furnace is heated to 800°C for 120 minutes under an argon flow of 1000 sccm. In both cases the distance is measured from the edge of the furnace housing.

Recently the system has been fitted with quartz furnace-tubes. Quartz tubes have the advantage of being transparent, which allows for easier sample loading and unloading and greater accuracy in sample placement. The furnace-tubes used have a wider inner diameter (2.2 cm) than the original tubes and so can accept larger boats, allow for a greater number of larger samples. This feature is especially useful for alternative applications of the furnace for uses such as annealing as they allow the introduction of larger sample volumes into the furnace.

Custom-made brass fittings were produced with a NW25 KF flange-face to allow the furnace-tubes to couple to the rest KF fittings in the system. These brass fittings are

attached to the quartz furnace-tube via a compression fitting composed of two rubber O-rings sandwiching a brass gasket (Figure 4-8).

Both types of furnace-tube are at high risk of cracking or breaking; this is due both to the brittleness of the materials and to their high aspect ratio shape. Any vertical or horizontal misalignments between opposite ends of the system risk putting a destructive amount of sheer stress on the delicate furnace-tube. In order to prevent this, sections of flexible stainless steel KF tubing were used to connect either end of the furnace-tube to the rest of the system. These flexible sections not only protect the tube from being twisted or bent, but also help to further isolate it from the vibrations caused by the pump, lessening the amount of rubbing between the tube and furnace housing.
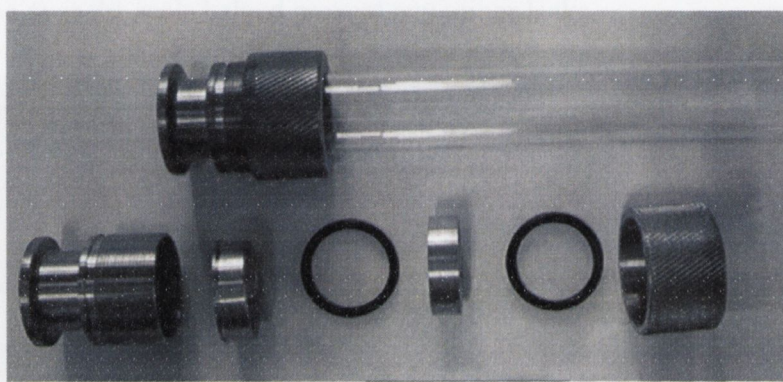
Figure 4-8 Image showing brass NW25 QF adaptor for the quartz furnace-tube. The Adaptor consists of a compression fitting containing a brass gasket sandwiched between two rubber O-rings.

Gas outlet system

The system requires a process to remove the unnecessary reaction by-products and unreacted precursor gases from the reaction chamber and vent them safely from the system. Gas removal was achieved by using a mechanical pump to move the unwanted gases through a series of filters and traps before venting them into a fume hood.

The pump:

During the CVD production of CNTs it is important to minimise the amount of oxygen present in the system in order to prevent burning the newly formed nanotubes. A rotary vane pump is a good choice as the first measure in removing gases from a closed system due to its cost effectiveness, robustness and ease of maintenance. An Edwards RV12 single phase rotary vane pump (with a maximum vacuum of $1*10^{-3}$ mbar) was placed at the opposite end of the system to the gas inlets (Figure 4-3, item 19). When in place, the

Edwards pump can produce an operating pressure of $2 - 3 * 10^{-2}$ mbar within a matter of minutes.

It was not deemed necessary that the CVD system operate at high or ultrahigh vacuum (HV and UHV). The fittings and gauges required for HV and UHV tend to be less cost effective and less robust then their low vacuum counterparts. The speed of pump down time and the lack of requirement for chamber bake-outs allow a lower vacuum system a quicker turnover time.

Despite the relatively high ultimate pressure that can be achieved with a rotary vane pump (at optimum performance the gaseous molecular density is 10^{15} cm^{-3} within the chamber[51]) it is low enough to stop prohibitive oxidation of the sample when combined with flushing the system with argon (Ar). Argon (40u) being substantially heavy than oxygen (16u) helps to literally push it out of the chamber.

The Edwards RV12 has a pumping capacity of 2 L per minute, comparable to both the flow rates (< 2 L per minute under usual operating conditions) and the total volume of the closed CVD chamber (2.5 L). The pump is also robust enough to maintain constant operation throughout an entire CVD cycle. The ballast is opened while the gases are bled into the CVD chamber to prolong the lifetime of the pump.

Rotary vane pumps are oil running pumps and as such they tend to generate a certain amount of vaporised oil at the outlet. To prevent this oil from entering the atmosphere and to help reclaim as much of it as possible an oil mist filter is attached to the outlet of the pump between it and the outlet hose. The remains of the exhaust are carried though a hose to the fume hood.

Traps and filters:

To ensure that any exhaust gases passing though the pump are as "clean" as possible a series of traps and filters have been incorporated into the system design. A liquid nitrogen cold-trap is situated immediately downstream of the furnace-tube. The trap consists of two stainless steel containers; one within the other. The inner canister is filled with liquid nitrogen; gas flows though the outer container. Upon contact with the cold walls of the inner canister any vapour within it condenses out of the gas flow and precipitates on the walls of the trap. The trap also acts as a physical trap for any larger particles; such as solid substrates or "blow-off" from powdered samples, which may become dislodged and travel out of the furnace-tube. A molecular sieve trap filled with activated alumina beads is placed on the inlet of the pump (Figure 4-3, item 1) to further clean the exhaust gas.

Monitory and control systems

In any research tool it is desirable to control and monitor all possible parameters involved in the process. In this system temperature of the reaction is both controlled and monitored by the furnace and its inbuilt thermocouple. The flow of gases into the system is controlled by a pair of MFCs which are in turn monitored and controlled by an external readout unit. The pressure within the chamber is measured by two gauges on either end of the system.

<u>The pressure gauges:</u>

In order to obtain accurate pressure readings two pirani gauges were placed on the system, one at either end of the work-tube (Figure 4-3, items 2 and 12). This placement is to account for any conduction limiting of the pressure brought about the geometry of the furnace-tube. This configuration of the pressure gauges also allows for greater ease in isolating any leaks which may occur in the system. Pirani gauges were chosen as they operate well in the pressure range achievable by the rotary vane pump. This type of gauge is very robust and can operate at any orientation.

Sample insertion and retrieval

An obvious and necessary feature of any CVD system is the ability to insert an unreacted sample substrate into the reaction chamber and remove it upon completion of the desired reaction.

<u>Sample loading:</u>

The sample load system is very simple. The pirani gauge mounted between the two MFCs can be easily removed, (Figure 4-9) opening a direct path to the centre of the furnace. The sample boats can then be easily pushed in and pulled out using a hooked rod.

The 5-way cross which houses the sample loading port (also the two MFCs and the vent-valve) sits across two Fisherbrand "labjacks". Each of the labjacks has a top plate area of 20 cm * 20 cm and a maximum height of 27 cm (and a maximum load capacity of 36 kg). The five way cross is affixed to both jacks via two 1 ¼" U-bolts, one over each side arm (connecting to the MFCs), in one of each of the jacks. Securing the five-way cross in this way prevents stressing the furnace-tube from knocks or jerks during sample introduction.

Other system features

Along with the main features for CVD as mentioned above, several other design choices are required in the build, namely how these different components are joined together and the implementation of various safeguards.

The fittings:

Kwikflange (KF) fittings are used to connect all the elements of the system other than in the gas lines where ¼" Swagelok fittings were used. KF flanges are compression fittings that can maintain vacuum down pressures down to below 10^{-4} mbarr. The seal is made by a neoprene O-ring on a stainless steel support-ring compressed between two flange-faces and held in place with a clamp. KF fittings are cheaper than other vacuum fittings such as Conflat flanges (CF), which require copper gaskets that must be replaced each time the flanges are opened. The KF fittings used are produced from stainless steel which does not have any noticeable outgassing effects under normal working pressure and are stable to temperatures well above the normal operating temperate of the furnace. Stainless steel can be easily cleaned with common solvents, such as isopropyl alcohol and acetone. All fittings used were QF NW25 (with an inner diameter of 2.54 cm) where possible.

Valves:

There are several valves are in place throughout the system. These valves act as either safety features to protect particularly delicate components, or can play a feature in the operation of the CVD itself.

Two Nupro "H" valves with Swagelok fittings (Figure 4-9, item 1) are in place, one in front of each of the two mass flow controllers. These valves act as a protective measure and can quickly isolate MFCs from the inlet gas line. In order to aid the smooth running of the CVD these valves can be "cracked" open to guard against "overshoot" in the MFCs when new flow rate set-points are selected. This overshoot can cause a burst of gas into the system, which may blow lighter, flimsier samples out of the sample boat or even push the boat out of the heated area of the furnace-tube.

A simple vent-valve is in place above the sample load port to allow the vacuum to be broken at the end of an experimental run (Figure 4-9, item 3). The vent valve can be opened gradually to ensure that pressure increase on venting is at a low enough rate so that the samples are not blown out of the sample boat.
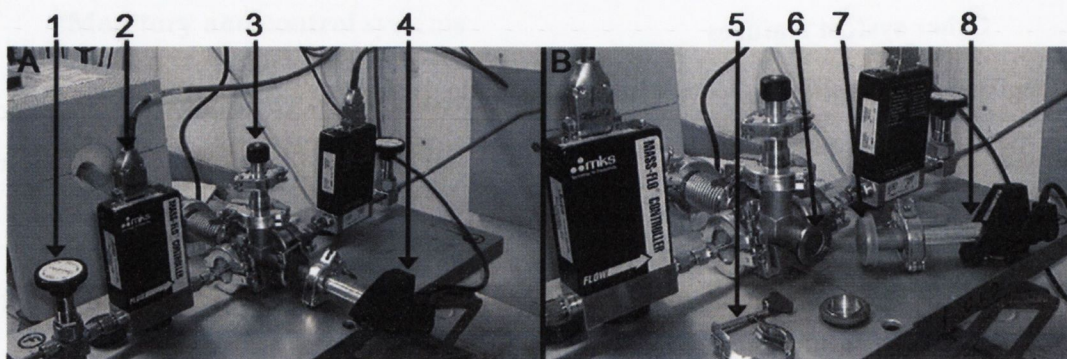
Figure 4-9 Photograph showing the front of the chamber A: closed, ready for pump down and B: open ready for sample loading or removal. 1: Nupro "H" shut off valve; 2: MKS mass flow controller; 3: vent-valve; 4: Pirani pressure gauge; 5: QF NW25 clamp beside NW25 O-ring and centring ring; 6: sample load port; 7: NW25 to NW16 converter nipple with dust cove; 8: Pirani pressure gauge.

A butterfly valve is located behind the liquid nitrogen trap (Figure 4-3, item 3). A butterfly valve consists of a plate mounted in the plane perpendicular to the gas flow. The plate can swivel on its centre axis within a cavity of the same diameter. The plate can be rotated so that it either completely blocks the cavity and stems the gas flow, or stands parallel to the direction of flow allowing the gas to flow around it. The butterfly valve is positioned so that when closed it isolates both the pump and the second pressure gauge from the rest of the system. In the event of a sudden jump in pressure (such as that caused by a crack or break in the furnace-tube) the pump can be quickly shut off from the main chamber so that it is not overstrained.

Closing the butterfly valve after the system has been pumped down and monitoring the changes in pressure on either side of the valve can help in highlighting and locating leaks in the system as well as being a check to ensure the pump is working at optimum capacity.

4.6.3 Safety

Safety is always a concern in the laboratory and several safety features are in place on the CVD system. The acetylene cylinder is fitted with a dual stage gas regulator along with a flashback arrestor to prevent a flame from an ignited stream of gas travelling back into the cylinder. Both the acetylene and argon cylinders can be quickly and simply isolated from the rest of the system by the two Nupro valves mentioned above. As general good practice neither cylinder is opened more than ½ - ¾ of a turn and the cylinder wrench is always left in place on the main cylinder valve when it is open (Figure 4-9).

When dealing with a highly combustible gas such as acetylene fire-prevention is always a premium concern. Since even static electricity could ignite acetylene it has been ensured that the rest of the CVD system is properly grounded.

The fumes emitted from the system under normal experimental conditions were checked for combustibility by filling a gas jar and adding a lit splint to the contents. A lit splint placed near the top of the jar showed no change. When the lit splint was placed at the bottom of the jar it was extinguished, thus it is concluded that only a negligible amount of non-pyrolysed acetylene remained in the exhaust fumes.

4.7 Overview of the CVD system

The system is simple and easy to use. The use of KF fittings means that removal or rearrangement of components is simple and quick, in fact the entire system can be taken apart, cleaned and reassembled by one person in less than one working day. The compact nature of the setup not only allows it to sit neatly on a desk but also allows for a fast turn around time. On average, from sample placement to sample removal during an experimental run can take as little as two hours plus the length of time for which the active gas is run. This speed means that several users can have access to the system on any given day. Overall the build's size and versatility make it ideal for controlled growth of small amounts of CNTs.

4.8 References

[1]   H. O. Pierson and M. L. Lieberman, Carbon **13**, 159-166 (1975).

[2]   H. Matsubara, Y. Yamaguchi, J. Shioya, and S. Murakami, Synthetic Metals **18**, 503-507 (1987).

[3]   M. Werner and R. Locher, Reports on Progress in Physics **61**, 1665-1710 (1998).

[4]   M. Leskela and M. Ritala, Thin Solid Films **409**, 138-146 (2002).

[5]   J. T. Drotar, Y. P. Zhao, T. M. Lu, and G. C. Wang, Physical Review B.

[6]   R. Alexandrescu, A. Crunteanu, R. E. Morjan, I. Morjan, F. Rohmund, L. K. L. Falk, G. Ledoux, and F. Huisken, Infrared Physics & Technology, 43-50.

[7]   Z. F. Ren, Z. P. Huang, J. W. Xu, J. H. Wang, P. Bush, M. P. Siegal, and P. N. Provencio, Science **282**, 1105-1107 (1998).

[8]   Y. G. Zhang, A. L. Chang, J. Cao, Q. Wang, W. Kim, Y. M. Li, N. Morris, E. Yenilmez, J. Kong, and H. J. Dai, Applied Physics Letters **79**, 3155-3157 (2001).

[9]   Y. M. Li, D. Mann, M. Rolandi, W. Kim, A. Ural, S. Hung, A. Javey, J. Cao, D. W. Wang, E. Yenilmez, Q. Wang, J. F. Gibbons, Y. Nishi, and H. J. Dai, Nano Letters **4**, 317-321 (2004).

[10]   K. L. Choy, Progress in Materials Science **48**, 57-170 (2003).

[11]   E. F. Kukovitsky, S. G. L'Vov, N. A. Sainov, V. A. Shustov, and L. A. Chernozatonskii, Chemical Physics Letters **355,** 497-503 (2002).

[12]   J. Haruyama, I. Takesue, S. Kato, K. Takazawa, and Y. Sato, Applied Surface Science **175-176,** 597-605 (2001).

[13]   J. Haruyama, I. Takesue, and T. Hasegawa, Physica B: Condensed Matter **323,** 252-255 (2002).

[14]   G. L. Hornyak, A. C. Dillon, P. A. Parilla, J. J. Schneider, N. Czap, K. M. Jones, F. S. Fasoon, A. Mason, and M. J. Heben, Nanostructured Materials **12,** 83-88 (1999).

[15]   Y. F. Mei, X. L. Wu, X. F. Shao, G. S. Huang, and G. G. Siu, Physics Letters A **309,** 109-113 (2003).

[16]   M. J. Kim, T. Y. Lee, J. H. Choi, J. B. Park, J. Seung Lee, S. K. Kim, J.-B. Yoo, and C.-Y. Park, Diamond and Related Materials **12,** 870-873 (2003).

[17]   Y. C. Sui, B. Z. Cui, R. Guardian, D. R. Acosta, L. Martinez, and R. Perez, Carbon **40,** 1011-1016 (2002).

[18]   X. Y. Zhang, L. D. Zhang, G. H. Li, and L. X. Zhao, Materials Science and Engineering A **308,** 9-12 (2001).

[19]   L. Huang, W. S. J, and S. P. O'Brien, Nano Letters **3,** 299 - 303 (2003).

[20]   E. Munoz, D. Coutinho, R. F. Reidy, A. Zakhidov, W. L. Zhou, and K. J. Balkus, Microporous and Mesoporous Materials **67,** 61-65 (2004).

[21]   Y. Murakami, S. Yamakita, T. Okubo, and S. Maruyama, Chemical Physics Letters **375,** 393-398 (2003).

[22]   B. Q. Wei, R. Vajtai, Y. Jung, J. Ward, R. Zhang, G. Ramanath, and P. M. Ajayan, Nature **416,** 495-496 (2002).

[23]   J. Zhu, M. Yudasaka, and S. Iijima, Chemical Physics Letters **380,** 496-502 (2003).

[24]   H. Ago, J. Qi, K. Tsukagoshi, K. Murata, S. Ohshima, Y. Aoyagi, and M. Yumura, Journal of Electroanalytical Chemistry **00,** 1-6 (2002).

[25]   G. S. Duesberg, A. R. Graham, F. Kreupl, M. Liebau, R. Seidel, E. Unger, and W. Hoenlein, Diamond and Related Materials **13,** 354-361 (2004).

[26]   S.-H. Jeong and K.-H. Lee, Synthetic Metals **139,** 385-390 (2003).

[27]   B. Q. Wei, R. Vajtai, Y. Jung, J. Ward, R. Zhang, G. Ramanath, and P. M. Ajayan, Chemistry of Materials **15,** 1598-1606 (2003).

[28]   A. Ural, Y. M. Li, and H. J. Dai, Applied Physics Letters **81,** 3464-3466 (2002).

[29]   S. S. Fan, M. G. Chapline, N. R. Franklin, T. W. Tombler, A. M. Cassell, and H. J. Dai, Science **283,** 512-514 (1999).

[30]   S. Fan, W. Liang, H. Dang, N. Franklin, T. Tombler, M. Chapline, and H. Dai, Physica E: Low-dimensional Systems and Nanostructures **8,** 179-183 (2000).

[31]   P. R. Bandaru, C. Daraio, S. Jin, and A. M. Rao, Nature Materials **4,** 663-666 (2005).

[32]   A. P. Graham, G. S. Duesberg, R. Seidel, M. Liebau, E. Unger, F. Kreupl, and W. Honlein, Diamond and Related Materials **13,** 1296-1300 (2004).

[33]   M.-K. Li, M. Lu, L.-B. Kong, X.-Y. Guo, and H.-L. Li, Materials Science and Engineering A **354,** 92-96 (2003).

[34]   S. Reitzenstein, L. Worschech, and A. Forchel, Ieee Electron Device Letters **24,** 625-627 (2003).

[35]   M. Terrones, International Materials Reviews **49,** 325-377 (2004).

[36]   S. C. Tseng, C. H. Li, Y. Y. Lin, C. H. Tsai, Z. P. Wang, K. C. Leou, C. H. Tsai, S. P. Chen, J. Y. Lee, and B. C. Yao, Diamond and Related Materials **14,** 2064-2068 (2005).

[37]   http://www.cnanotech.com/.

[38]   Gaille, (1944).

[39]   S. Mann, (USA, 1880).

[40]   M. L. Hitchman and K. F. Jenson, *Chemical Vapor Deposition: principles and applications* (Academic Press Inc., London, 1993).

[41]   http://www.umaine.edu/lasst/devicefab.htm.

[42]   M. R. Werner and W. R. Fahrner, Ieee Transactions on Industrial Electronics **48**, 249-257 (2001).

[43]   K. Kitahama, K. Hirata, H. Nakamatsu, S. Kawai, N. Fujimori, T. Imai, H. Yoshino, and A. Doi, Applied Physics Letters **49**, 634-635 (1986).

[44]   K. Suzuki, A. Sawabe, H. Yasuda, and T. Inuzuka, Applied Physics Letters **50**, 728-729 (1987).

[45]   K. E. Spear, M. Frenklach, A. Badzian, T. Badzian, T. Hartnett, and R. Messier, Journal of the Electrochemical Society **134**, C483-C483 (1987).

[46]   Y. Gurbuz, O. Esame, I. Tekin, W. P. Kang, and J. L. Davidson, Solid-State Electronics **49**, 1055-1070 (2005).

[47]   B. V. Spitsyn, L. L. Bouilov, and A. E. Alexenko, Brazilian Journal of Physics **30**, 471-481 (2000).

[48]   http://www.timedomaincvd.com/CVD_Fundamentals/films/SiO2_properties.html.

[49]   http://www.ecs.csus.edu/techshop/ApndxE.html.

[50]   http://www.labsafety.com/refinfo/ezfacts/ezf181.htm.

[51]   J. B. Hudson, *Surface science: an introduction* (Wiley interscience, New York, 1998).

[52]   S. Hofmann, G. Csanyi, A. C. Ferrari, M. C. Payne, and J. Robertson, Physical Review Letters **95** (2005).

[53]   H. Kanzow and A. Ding, Physical Review B **60**, 11180-11186 (1999).

[54]   V. N. Parmon, Catalysis Letters **42**, 195-199 (1996).

[55]   Y. H. Mo, A. K. M. F. Kibria, and K. S. Nahm, Synthetic Metals **122**, 443-447 (2001).

[56]   A. Sacco, P. Thacker, T. N. Chang, and A. T. S. Chian, Journal of Catalysis **85**, 224 (1984).

[57]   L. F. Su, J. N. Wang, F. Yu, and Z. M. Sheng, Chemical Vapor Deposition **11**, 351-354 (2005).

[58]   B. Q. Wei, R. Vajtai, Z. J. Zhang, G. Ramanath, and P. M. Ajayan, Journal of Nanoscience and Nanotechnology **1**, 35-38 (2001).

[59]   Y. C. Choi, D. W. Kim, T. J. Lee, C. J. Lee, and Y. H. Lee, Synthetic Metals **117**, 81-86 (2001).

[60]   J. Gavillet, A. Loiseau, F. Ducastelle, S. Thair, P. Bernier, O. Stephan, J. Thibault, and C. J. C., Carbon **40**, 1649 (2002).

[61]   J. Zhao, A. Martinez-Limia, and P. B. Balbuena, Nanotechnology **16**, S575-S581 (2005).

[62]   H. Numakura, K. Kashiwazaki, H. Yokohama, and M. Koiwa, Journal of Alloys and Compounds **310**, 344 (2000).

[63]   X. Fan, R. Buczko, A. A. Puretzky, D. B. Geohegan, J. Y. Howe, S. T. Pantelides, and S. J. Pennycook, Physical Review Letters **90**, 145501 (2003).

[64]   R. Jean-Yves, G. Francois, and G. Giulia, Physical Review Letters **95**, 096103 (2005).

Chapter 5 CNT growth and alternative treatments in the custom-built CVD system

5.1 Introduction

This chapter will discuss the various applications of the custom-built CVD system discussed in the chapter 4. Section 5.1 will comprise of a brief review of some projects and results achieved that are not directly related to growth of interconnect arrays. A variety of CNT geometries have been achieved using various combinations of conditions, catalyst and substrate. A summary of some alternative uses of the system will be shown in sections 5.2 and 5.3.

5.2 Carbon nanotubes grown in the custom-built CVD system

The following section shall discuss the various geometries and alignments of CNTs grown in the system. Some examples of alternative catalyst delivery methods and substrates will also be given.

5.2.1 Long CNTs

Alongside the CNT arrays grown in the custom-built CVD system, long MWNTs are often produced. These tubes have lengths in the tens of microns and aspect ratios of ~1000. Long CNTs are desirable for their physical properties such as increased binding in composite materials. However long CNTs especially MWNTs, which are mostly metallic, could be

used for wiring micro-electric devices and even as components in microelectro-mechanical systems such as micro-electric motors.

Ultralong CNTs have been grown to lengths of hundreds of microns,[1-3] millimetres[4,5] and even centimetres.[6,7] Free standing SWNT ropes have been grown to lengths of tens of centimeters[8]. While the majority of long tubes are produced by CVD methods, arc-discharge grown MWNTs with ratios of >1000 have also been reported.[9,10] Recently long MWNTs have been shown to increased alignment in epoxy composites and have.[11] Long MWNTs have been fabricated into elaborate patterns and networks through by their inner shells with an AFM tip.[12]

The majority of long tubes were grown on iron-filled porous alumina membranes at 700 – 800°C, under 5000 sccm of argon and 3000 sccm of acetylene. On removal from the CVD furnace the samples were seen to have changed from a translucent white to a shiny black.

The long tubes grown on these PAM substrates are typically in the order of tens of microns in length and tend to occur on flat sections of PAM where metal catalyst had agglomerated on the surface. The high flow rates most likely act to carry the growing CNT along with the gas flow, keeping it off the surface and allowing for unhindered growth.

One contributing factor to enhanced length in CNTs grown in CVD is gas flow within the reaction chamber.[7,13] Huang et al suggest a kite mechanism for ultralong SWNTs.[13-15] They suggest that tip growth SWNTs can be lifted from the substrate either by convection currents in the heated gases or from a vertically aligned electric field. Once freed from the substrate surface the metal tip particles are caught in the laminar flow and kept aloft, the tubes then continue to grow in the direction of the flow. Growth stops when either the metal particle hits the substrate again or the carbon source is stopped.

The limit in length of CNTs grown in the custom-built CVD most likely arises from the chaotic flow in the reaction chamber. The gas inlet tubes for the argon and acetylene are directly opposite each other and perpendicular to direction of the furnace tube (see figure 4-9). This arrangement encourages kink and bend formation through an uneven mixing of the carbon feed stock. This large amount of bending makes it more likely that the tubes will hit the surface of the substrate reducing the likelihood of ultralong CNT growth.

Another criterion for ultralong CNT growth is the ability to prevent "carbon poisoning" of the catalyst particles. Hata et al have used water vapour in their gas mix to grow ordered arrays of CNTs 2.5mm high[20]. Water acts as a weak oxidiser that selectively

removes amorphous carbon from around the catalyst particles without damaging the growing tubes.

The custom-built CVD system contains no inlet for oxidising species (such as water, hydrogen or ammonia) due to logistical factors. Therefore the limitation on tube length could also be due to carbon poisoning of the catalyst particles. Raman spectra of such samples tend to show large D-bands relative the G-band, would also suggest carbon poisoning due presence of significant amounts of amorphous carbon (Figure 5-1).
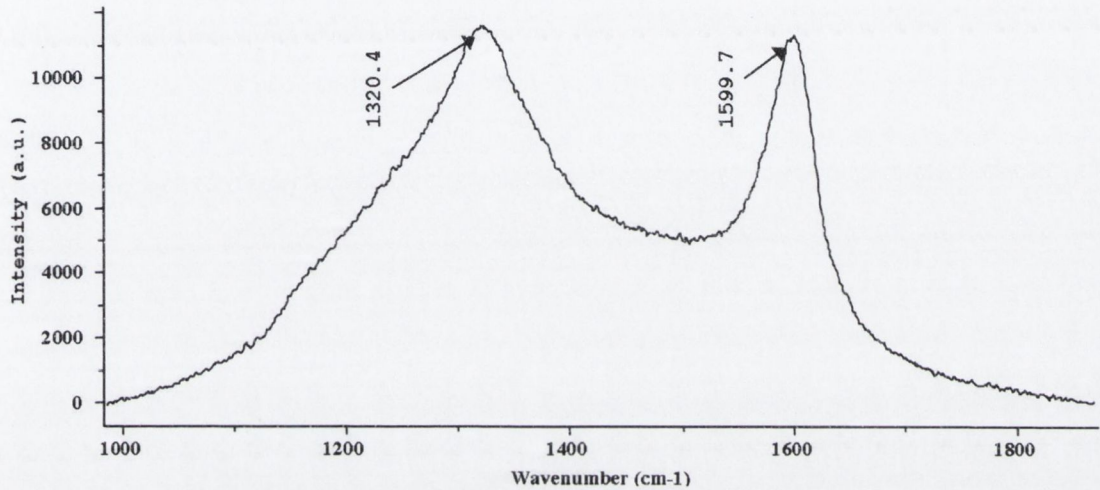
Figure 5-1 Typical Raman spectrum for MWNTs grown in iron-filled PAMs. The spectrum was taken using 632 nm laser light.

Figure 5-2 shows a selection of long tubes with high aspect ratios. Figure 5-2A shows a single long tube grown on the surface of an Iron filled porous alumina membrane (PAM). These tubes were grown at 800°C under an acetylene flow rate of 100 sccm for 49 minutes mixed with an Argon flow of 800 sccm. The straight length of the tube is approximately 17 μm. However as can be seen the tube does double back on itself giving it a total length of 21 ± 2 μm. The diameter of this tube has been measured as 30 ± 10 nm, resulting in an aspect ratio of around 800.

Figure 5-2B shows a network of long tubes also grown on an iron filled PAM substrate but at a temperature of 700°C under an acetylene flow rate of 100 sccm for 56 minutes mixed with an Argon flow of 800 sccm. The lengths of the tubes ranged from 3.8 - 13.3 μm each with a deviation of ± 0.3 μm. The diameters of all the tubes were measured to be 20 ± 10 nm, giving aspect ratios of up to 1000 ± 400.

Figure 5-2C shows another tube grown on the same substrate and under the same conditions as Figure 5-2B. It has a length of 18.0 ± 0.3 μm and a diameter of 30 ± 10 nm giving it an aspect ratio of 700 ± 300.

Figure 5-2D differs from the previous examples in that the long tubes are grown on etched Si substrate at a temperature of 800°C under an acetylene flow rate of 50 sccm for 40 minutes mixed with an Argon flow of 500 sccm. A dense carpet of long entangled CNTs was produced; this density is thought to arise not from the conditions of growth but in the manner that the catalyst was introduced onto the substrate. A relatively high concentration of catalyst containing solution (1%) was used instead of the more dilute concentrations discussed in chapter 6. The increased size of metal particles therefore allowed more carbon to be absorbed and longer tubes to be grown. It is also evident from the micrograph that although the substrate is patterned, the CNTs are not growing from the trench edges.

Rather these tubes are growing from the flat sections in between. The growth and termination mechanisms therefore, would be the same as for the previous examples. Part of the carpet was scraped away with a razor blade. It is the edge of this scraped area that is shown in the figure. The section of tube shown is 9.4 μm long with a diameter of 25 ± 5 nm giving it an aspect ratio of at least 460.

5.2.2 CNT mats and forests

The growth of CNTs mats and dense carpets[16-30] has been researched quite extensively in the literature. The applications of these arrays include the possibility of large scale bulk synthesis of CNTs. However, the controlled positioning of dense vertically aligned CNT growth could be used in field emission devices,[31] chemical sensors [32] and optical devices.[33] Arrays of tubes have also been grown using catalyst metal-filled PAM as templates for growth.[34]

The custom-built CVD system is capable of growing dense carpets of CNTs through the placement of concentrated amounts of catalyst on the substrate before CVD treatment.

Figure 5-3 shows tubes grown at a temperature of 700°C under an acetylene flow rate of 50 sccm for 60 minutes mixed with an Argon flow of 500 sccm. The substrate used was a plain Si wafer segment. The iron catalyst was applied via a 0.5% solution of poly(styrene-vinylferrocene) (PVF) in toluene dropped onto the substrate surface and allowed to dry before the sample was loaded into the furnace tube. After CVD treatment the majority of the surface was found to be covered in a dense mat of "spaghetti-like," randomly orientated CNTs. The average diameter of the CNTs in was found to be 38 ± 7 nm.
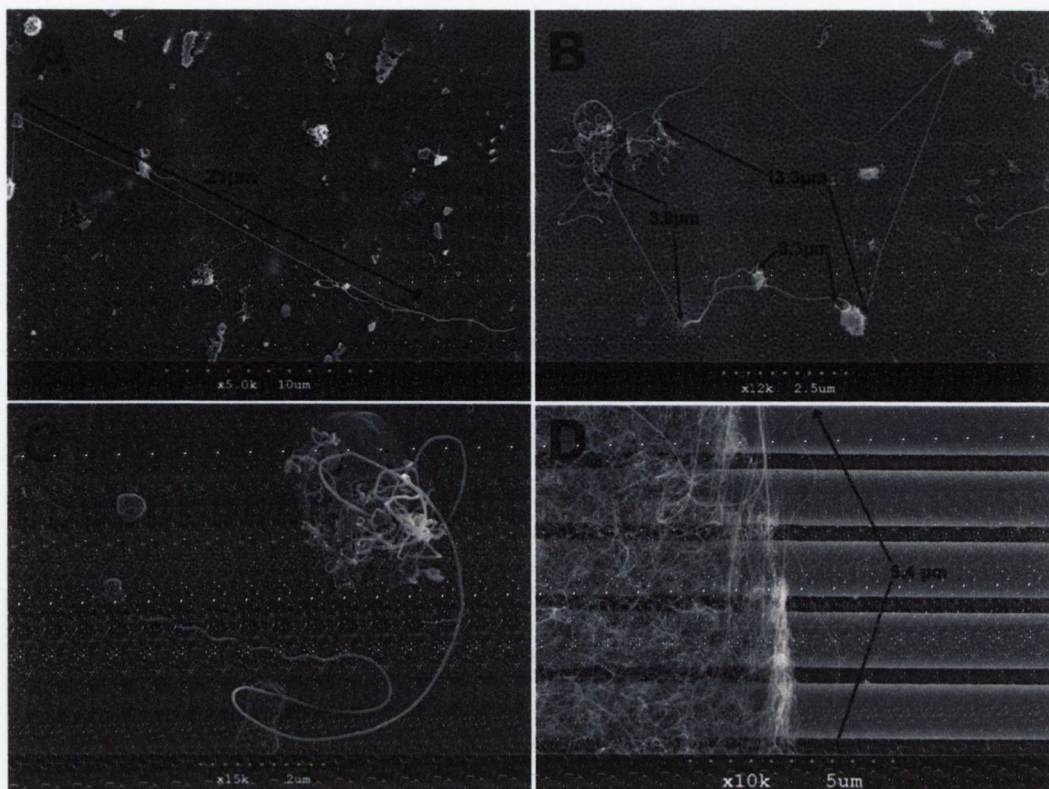
Figure 5-2 SEM micrographs showing long tubes grown on porous alumina membranes (A-C) and silicon dioxide substrate (D) under the following conditions: A) Temp= 800°C, Ar flow= 5000 sccm, C₂H₂ flow = 3000 sccm, time= 49 minutes; B & C) Temp= 700°C, Ar flow= 5000 sccm, C₂H₂ flow = 3000 sccm, time= 56 minutes; D) = 800°C, Ar flow= 500 sccm, C₂H₂ flow = 50 sccm, time= 40 minutes .

Denser, more ordered CNT-carpets were produced using a higher concentration (~1%) of catalyst containing PVF solution (Figure 5-4). The catalyst was patterned on the substrate via soft lithography using a patterned stamp.[16] As can be seen in Figure 5-4A CNT growth on the catalyst islands is substantially denser. The CNTs grew close enough together that the Van der Waals forces allowed the tubes to sterically support each other to grow vertically. The tubes were noted to be predominantly vertically aligned over the bulk of the catalyst region. At the edges of the islands a fringe of horizontal tubes was noticed (Figure 5-4B). The horizontal tubes show less orientation that those aligned vertically; however they are seen to grow radially away from the centre of the island.

The highest quality CNT forests were grown on substrates that were pre-treated by evaporating 15 nm of iron through a simple mask fabricated from a sheet of aluminium foil designed to give islands of a variety of sizes (Figure 5-5). The CVD was performed at a temperature of 700°C under an acetylene flow rate of 300 sccm for 150 minutes mixed with an Argon flow of 1000 sccm on Si substrates. Figure 5-5 shows a set of micrographs with progressively higher magnifications on a forest of tubes grown on one of the large catalyst islands (~10 mm² in area). In order to accurately measure the height of the forests

the samples were imaged without a gold coating and the sample was tilted to an angle of 60°. The forest was measured to be 65 ± 3 μm in height. The tubes in the forest are small range of diameters from 8 ± 1 nm to 16 ± 1 nm. Overall the growth of these forests was shown to be even across the across the bulk of the catalyst metal islands. No CNTs are noted on areas of the substrate that were covered during iron evaporation.
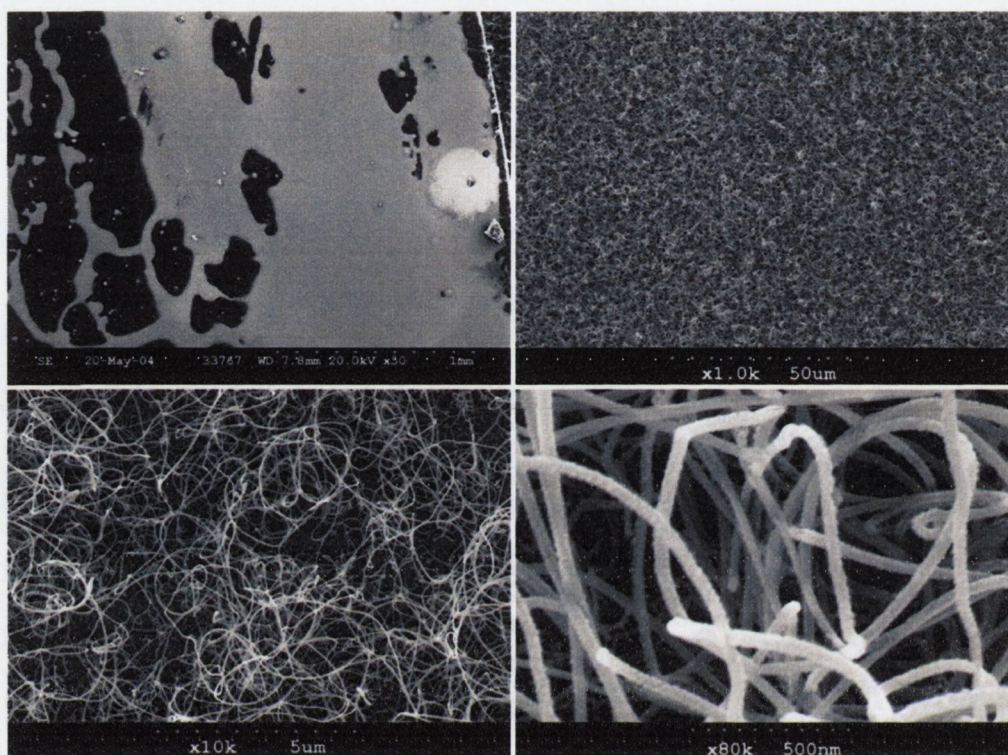
Figure 5-3 shows a series of SEM micrographs illustrating a series of progressive close-ups of a tangled mat of spaghetti-like CNTs grown on a plain silicon wafer using an iron catalyst under the following condition: Temp= 700°C, Ar flow= 500 sccm, C_2H_2 flow = 50 sccm, time= 60 minutes.
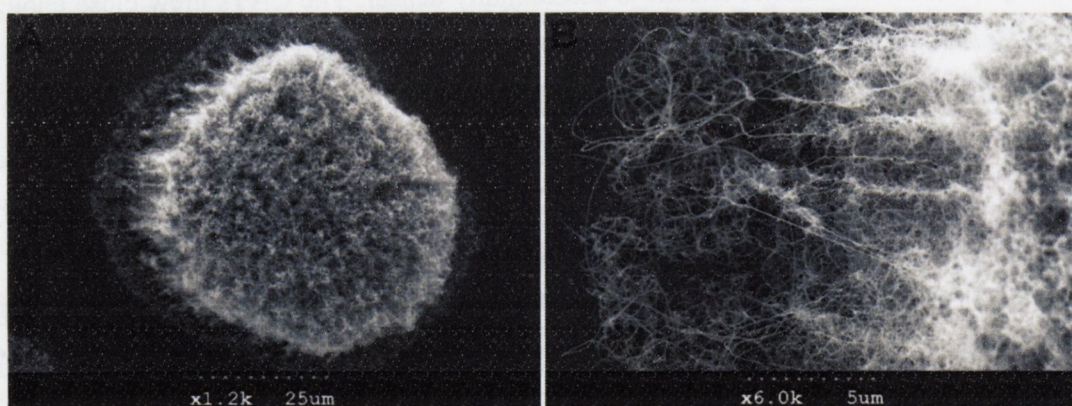
Figure 5-4 SEM micrograph displaying A: a vertically aligned column of CNTs grown on a patterned catalyst island, and B: a close-up of the horizontal radially aligned CNTs at the edge of the catalyst island. The CNTs grown on a plain silicon wafer using an iron catalyst.
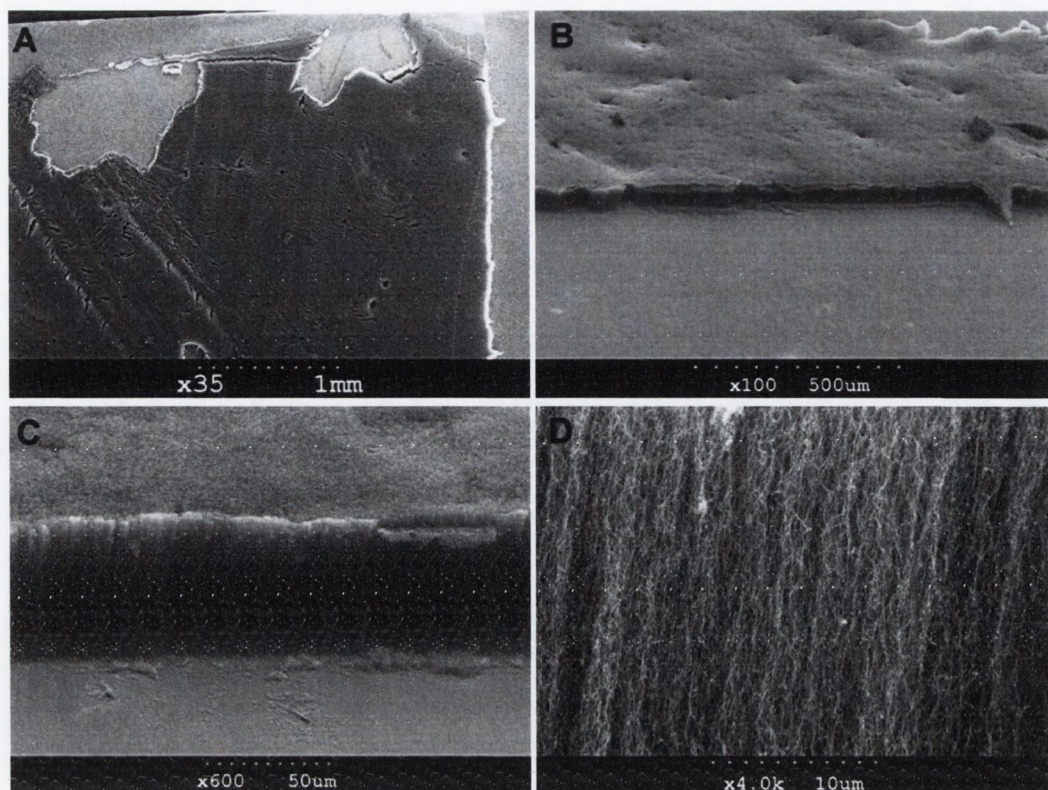
Figure 5-5 A series of SEM micrographs (A-D) showing a series of progressive close-ups of a large forest of CNTs grown on iron evaporated onto a Si substrate under the following condition: Temp=700°C, Ar flow= 1000 sccm, C_2H_2 flow=300 sccm, time=150 minutes.

5.2.3 Growth on mesoporous silica

The characteristics of CVD grown nanotubes are affected not only by conditions such as temperature, time and catalyst, but also by the substrate morphology. Porous matrices such as porous alumina membranes (PAMs)[35-45] and mesoporous silica[4, 18, 27, 46-51] can be used as templates for ordered arrays of CNT growth.

A preliminary feasibility study of CNT growth on mesoporous silica was undertaken in collaboration with Prof. Spalding's Dimensional Solids Group in University College Cork. A number of mesoporous silica samples incorporating different concentrations of either iron or cobalt catalyst were received.

The growth of CNTs within the pores of such a ceramic could result in a composite with increased thermal conductivity and reduced thermal shock resistance combined with the strength and toughness of the ceramic. Such a composite could have applications as conductive substrates for microprocessor die mountings or coatings and packaging in the electronics industry.

Initial CVD experiments with these samples yielded substantial CNT growth. Figure 5-6 shows a powdered sample of Dicobalt octacarbonyl in P65 mesoporous silica that had undergone CNT growth at a temperature of 800°C under an acetylene flow rate of

50 sccm for 72 minutes mixed with an Argon flow of 500 sccm. Visually, the powder sample was seen to turn from its original dark grey colour to black after CVD treatment.

The CVD treated samples were examined under SEM. A range of CNT diameters from ~20 – 60 nm were measured (Figure 5-6C). These relatively large diameters suggest that it is unlikely that they could have originated from the pores which are quoted as being 3 nm in diameter.
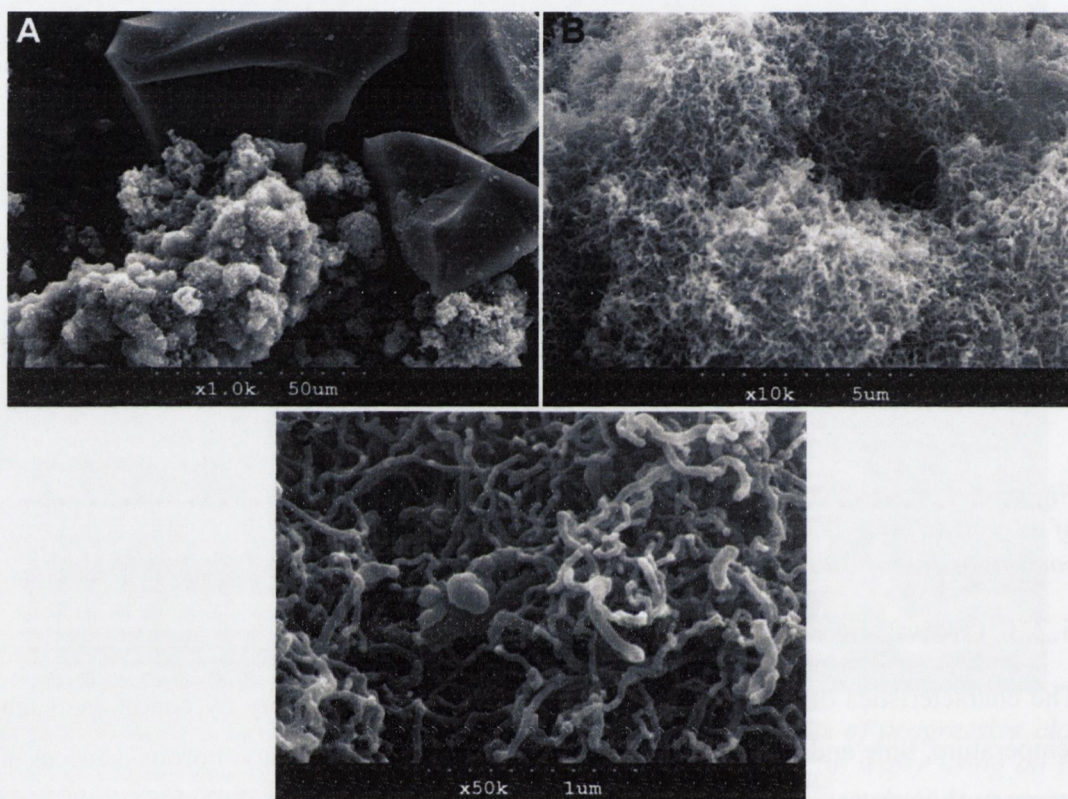
Figure 5-6 SEM micrographs depicting A: a low magnification over view of several Co-filled silica particles after CVD, note that significant growth appears only on the particle in the lower middle region of the micrograph. B & C show consecutive close-ups of the CNT growth on the lower-middle particle of micrograph A. CVD was carried out substrate under the following conditions: Temp= 800°C, Ar flow= 500 sccm, C_2H_2 flow = 50 sccm, time= 72 minutes.

An EDX study of the surface of the silica samples in different treatment-states was undertaken. An investigation of the "as-received" sample suggests that the catalyst metal is actually on the surface in places (Figure 5-7). In regions where the EDX spectra show metal peaks bright features are visible under back scattered SEM. Features that appear bright under backscatter SEM suggest that they are heavier than their surrounding and/or are raised above them. The EDX unit has a penetration depth of ~1 μm below the surface. In regions where no metal peaks are measured one can assume that there is no metal less

than 1 µm down into the pores. Areas of the sample surface where the bright metal islands were not seen produced EDX spectra with negligible metal peaks.
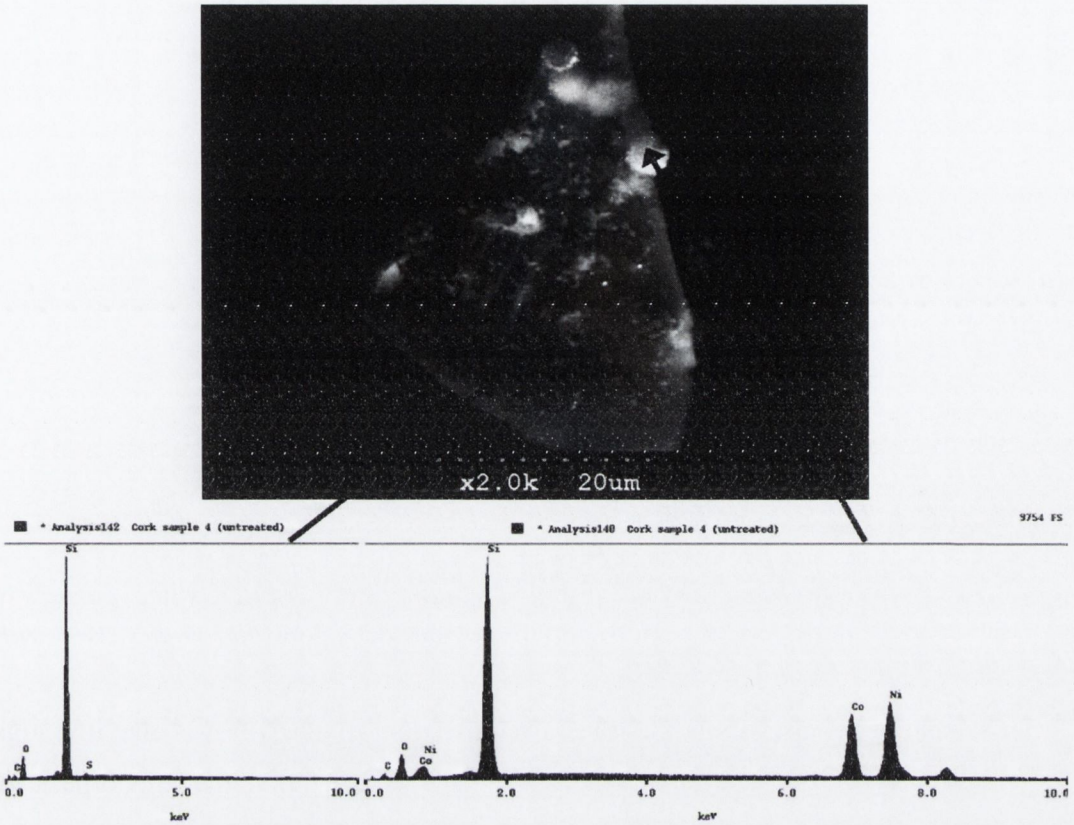
Figure 5-7 Low resolution SEM micrograph of "as-received" Co-filled silica particle with representative EDX spectra for regions containing surface metal (left) and regions without metal catalyst on the surface (right).

The sample used above was again investigated with EDX after it had been annealed under similar conditions to those used during the CVD, except without the introduction of the reactive gas (Figure 5-8). Visually, the appearance of metal islands on the surface are clearer and more distinct that for non-annealed samples. The EDX spectra showed that the ratio of the height of the Co peak with respect to the Si peak was substantially higher than for the untreated samples in all metal locations investigated. Figure 5-8 shows representative Si and Co peak heights for an annealed sample.
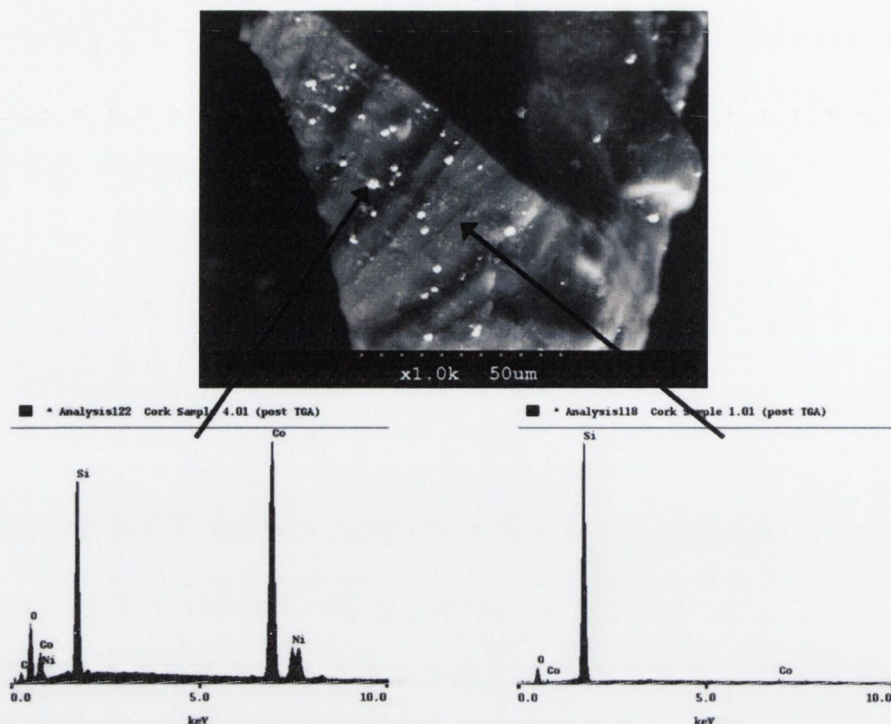
Figure 5-8 Low resolution SEM micrograph of annealed Co-filled silica particle with representative EDX spectra for regions containing surface metal (left) and regions without metal catalyst on the surface (right).

A small amount of the CVD treated sample from Figure 5-6 was also investigated using EDX (Figure 5-9). The metal islands yielded spectra with similar Si:Co peak ratios to those seen in the annealed samples with the addition of a significant carbon peak. No significant traces of carbon are seen on regions of the sample that do not contain surface metal.
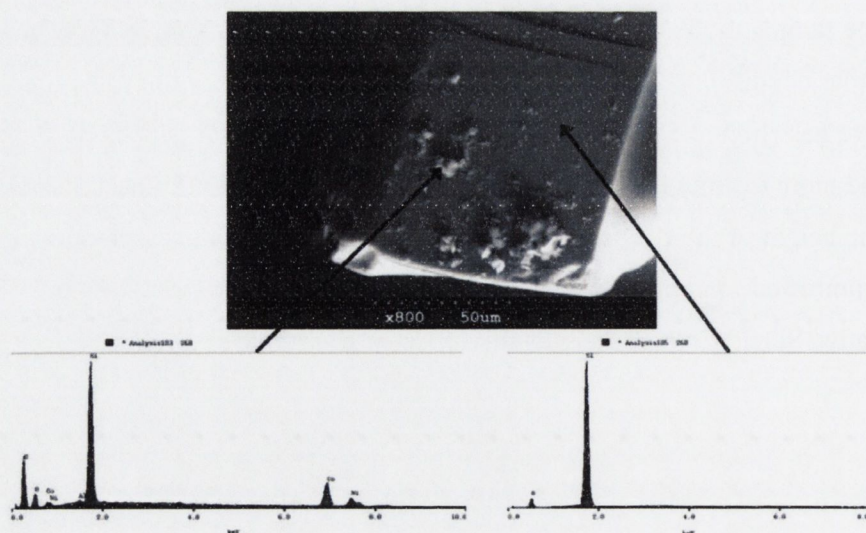
Figure 5-9 Low resolution SEM micrograph of Co-filled silica particle after CVD (under the conditions: Temp= 800°C, Ar flow= 500 sccm, C_2H_2 flow = 50 sccm, time= 72 minutes) with representative EDX spectra for regions containing surface metal and carbon (left) and regions without metal catalyst on the surface (right).

This inhomogeneous coverage of carbon is consistent with the results found from hi-resolution SEM investigation. As can be seen in Figure 5-6 the lower middle silica particle presents substantial but patchy growth of CNTs (Figure 5-6A), whereas the two particles in the upper region of the micrograph displayed much more sparse coverings of CNTs. The same inhomogeneity was also seen in Raman spectroscopy study of the sample: spectra were collected at several points over the surface of the sample. In many regions only the peaks associated with silica were found, whereas with in other sections the characteristic peaks for CNTs were seen (Figure 5-10). From this it can be assumed that only catalyst metal available to seed CNT growth is located on the surface as opposed to within the pores.
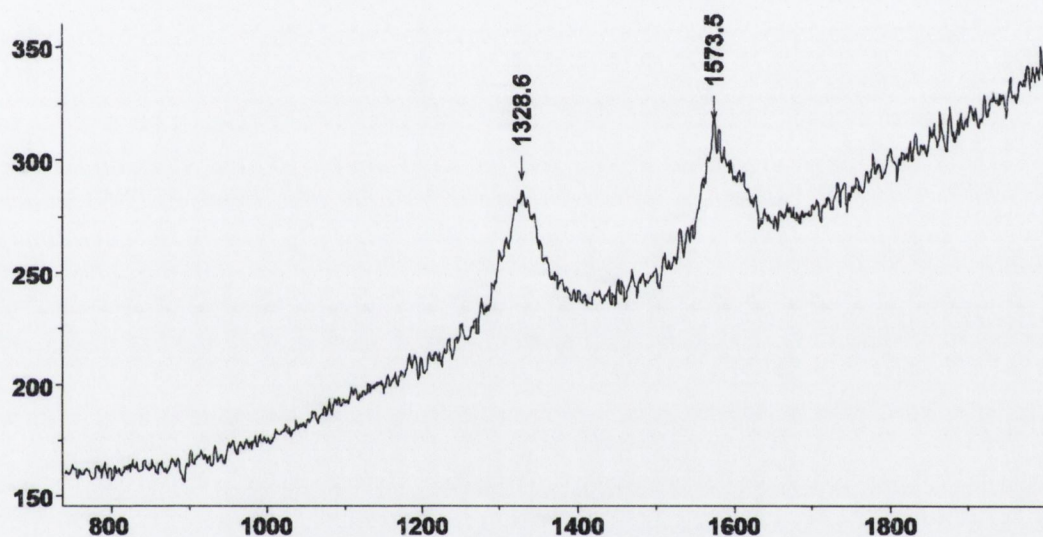
Figure 5-10 Raman spectra of the carbon containing regions on the surface of the Co-filled silica particle after CVD (under the conditions: Temp= 800°C, Ar flow= 500 sccm, C₂H₂ flow = 50 sccm, time= 72 minutes), which display the characteristic peaks associated with CNTs.

Similar results were noted for Iron-filled samples. A powdered sample of tri-iron dodecacarbonyl in P85 silica was run in the CVD system growth at a temperature of 800°C under an acetylene flow rate of 50 sccm for 60 minutes mixed with an Argon flow of 500 sccm. An EDX study of the sample before and after CVD comprising of scans accumulated over a larger area than previous study (~100 μm^2) gave an overview of the surfaces before and after CVD (Figure 5-11). It can be seen that amounts of iron and carbon on the surface is vastly increased after CVD. Both high-resolution SEM and Raman spectroscopy (Figure 5-12) confirm that there are indeed CNTs present on the surface and these are undoubtedly the major contributor to the high C peak seen in the EDX spectra. The SEM investigation of the surface showed a range of CNT diameters from ~10–70 nm. Even larger structures, possibly carbon fibres with even larger diameters of up to 200 nm

were also noted in several samples. This variety of shapes and sizes suggest that the CNTs are not growing from uniform catalyst particles as would be the case if they were contained within a porous lattice.
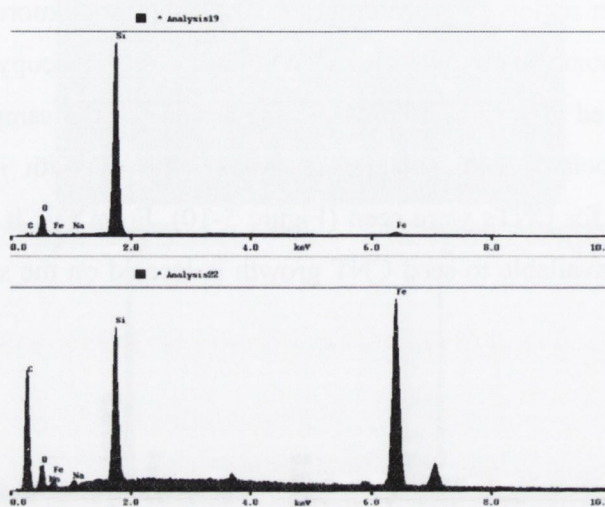
Figure 5-11 shows representative EDX spectra taken from a ~100 μm² area on the surface of iron-filled mesoporous silica powder before (top) and after (bottom) CVD under the following conditions: Temp= 800°C, Ar flow= 500 sccm, C₂H₂ flow = 50 sccm, time= 60 minutes.
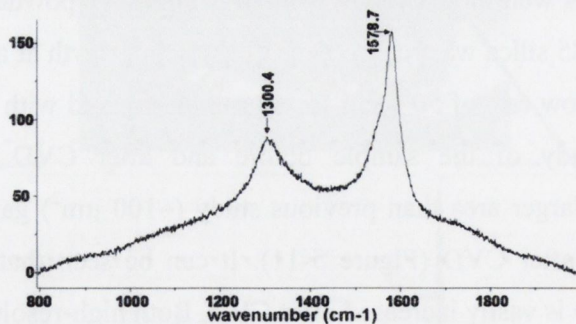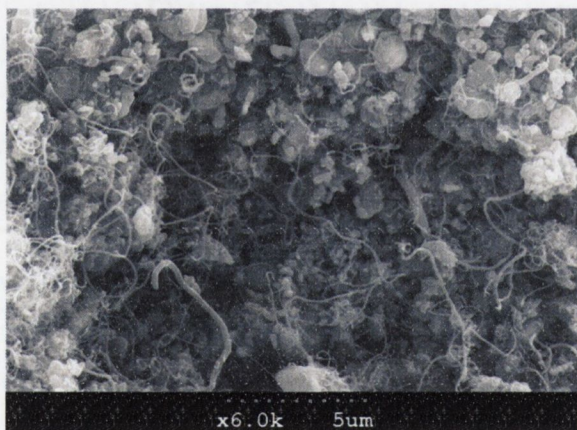
Figure 5-12 shows the Raman spectra detailing the characteristic CNT peaks at ~1330 & 1580 cm⁻¹ (left) and an SEM micrograph showing CNTs grown on iron-filled mesoporous silica powder under the following conditions: Temp= 800°C, Ar flow= 500 sccm, C₂H₂ flow = 50 sccm, time= 60 minutes.

Following on from this initial feasibility study the project was continued with research focusing on working with metal-filled mesoporous silica-powder samples that have been acid-cleaned to remove surface metal and with mesoporous silica thin films.[52] Work on this project is ongoing.

5.3 Alternative catalyst delivery system

The field of nanotube growth is still relatively new. The investigation of new and novel methods for catalyst delivery and growth in general is ongoing.[3, 53]

A simple and cost effective catalyst delivery method is always desirable in CVD growth of CNTS. To this end an aqueous iron (II) sulphate ($FeSO_4$) solution was investigated. Aqueous solutions negate the need for expensive and possibly hazardous organic solvents. It was also hoped that the crystalline structure of $FeSO_4$ would provide natural patterning of the resultant CNTs.

Initial tests showed that even saturated solutions of $FeSO_4$ were too viscous to provide a sufficient of catalyst on the substrate surface. Even the process of drop-casting several layers was found to be ineffective.

It was found the addition of a stiffening agent such as polyvinylpyrrolidon (PVP) resulted in a better surface coverage during drop casting of films on the substrate surface. The best growth results were achieved using a solution of ~2% $FeSO_4$ and ~2% PVP in water (i.e. 0.21 g $FeSO_4$ and 0.20g PVP (MWCA 55,000) in 10ml H_2O) dropped onto a plain Si wafer segment and growth conditions consisting of a temperature of 700°C under an acetylene flow rate of 50 sccm for 60 minutes mixed with an Argon flow of 500 sccm (Figure 5-13).

The addition of PVP provides a solution of low enough viscosity to form a droplet on substrate surface when drop-cast. This droplet allows a sufficient amount of catalyst to be held on the surface without simply flowing off the edge. Once the water has evaporated from a drop-cast sample the familiar crystal structure of the iron sulphate is seen. The speed of evaporation was found to have an effect on resultant crystal size. Samples dried in an oven at 60°C were found to be of a sufficiently small size so as not be too raised above the substrate surface. Investigation of the sample surface after CVD reveals that an outline of the crystal pattern on the substrate surface remains as an amorphous skeleton (Figure 5-13A). The amorphous skeletal outline was found to be made up of nests of randomly orientated CNTs (Figure 5-13B & C). The diameters of the CNTs in the middle of the nests were found to have a variety of diameters ranging from ~20 – 70 nm. The amorphous

skeleton itself was found to contain a mixture of CNTs and carbon fibres (Figure 5-14). The long fibre in Figure 5-14A was measured at 37.7 ± 0.3 µm long and 360 ± 20 nm in diameter.
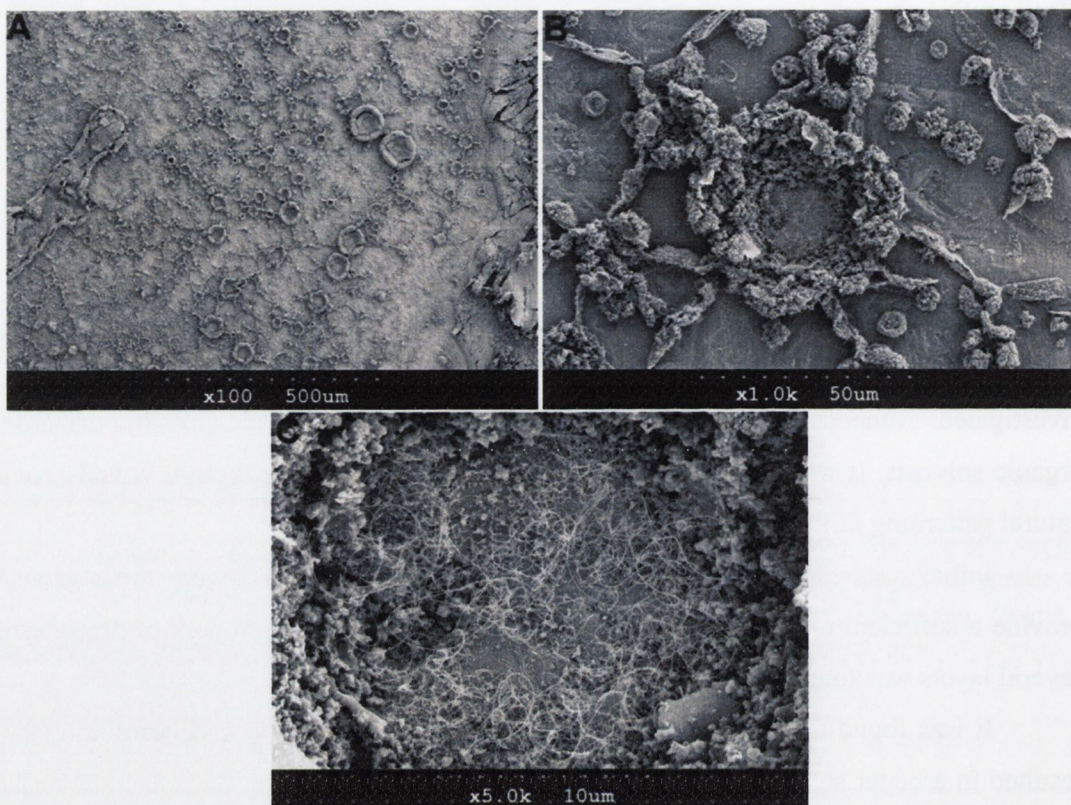
Figure 5-13 SEM micrographs illustrating series of progressively higher magnified images of a "nest" of CNTs at the centre of a hollow in the amorphous skeleton left behind after CVD of a FeSO$_4$/PVP solution dropped and dried onto a plain silicon wafer substrate under the following conditions Temp= 700ºC, Ar flow= 500 sccm, C$_2$H$_2$ flow = 50 sccm, time= 60 minutes.
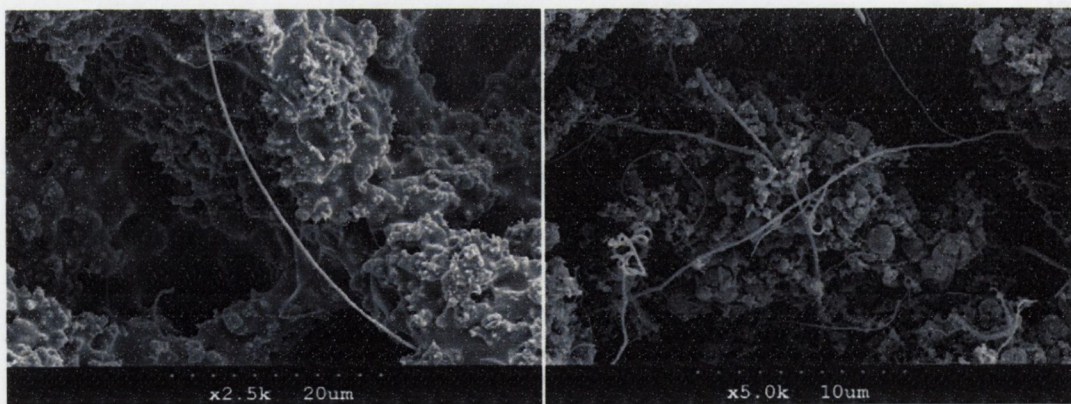
Figure 5-14 SEM micrographs illustrating a representative distribution of CNTs and carbon fibres grown on the amorphous skeleton during CVD.

Though the results using FeSO$_4$/PVP solutions proved to be both interesting and beautiful the presence of the amorphous skeleton and the carbon fibres among the CNT

yield mean that other catalyst delivery mechanisms such as PVF and iron evaporation as mention above are more favourable.

5.4 Treatment of pre-grown CNTs

As mentioned, the CVD system was designed to be flexible. An alternative application which requires virtually no modification of the system is that of nanotube annealing. It has been shown that functional groups can be removed from CNTs (from nanocyl) through heating in an inert atmosphere. The IR spectrum of the unannealed tubes suggest the presence of carboxylic acid groups -C(=O)OH on the surface of the CNTs. This is suggested by the presence of CO peaks at ~1660 cm^{-1}, along with the sharp C=O stretch peaks and the O-H stretching band appearing at around 3000 cm^{-1}.

The functionalised CNTs to be annealed are placed in a clean sample boat and wrapped in aluminium foil. The foil is pierced in several places so that although gas can pass into the boat most of the tubes are still contained by the foil. These foil wrapped boats are then loaded into the furnace which is pumped down and heated up to 500°C under an Argon flow of 1000 sccm. Annealing continues for 1 hour before the system is cooled and the samples removed. Infrared spectroscopy before and after annealing shows significant reduction of functional groups. (Figure 5-15)
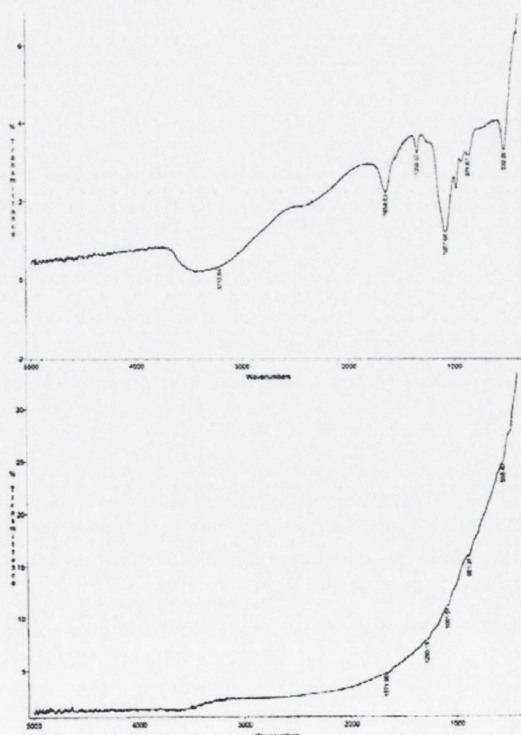
Figure 5-15 IR spectra of A: untreated CNTs containing functional groups, and B: annealed CNTs for one hour at 500°C under Ar flow of 1000 sccm.

5.5 References

[1]   W. Kim, H. C. Choi, M. Shim, et al., Nano Letters **2**, 703 (2002).

[2]   N. Franklin and H. J. Dai, Advanced Materials **12**, 890 (2000).

[3]   M. Kumar and Y. Ando, Diamond and Related Materials **12**, 998 (2003).

[4]   L. M. Huang, X. D. Cui, B. White, et al., Journal of Physical Chemistry B **108**, 16451 (2004).

[5]   S. M. Huang, X. Y. Cai, and J. Liu, Journal of the American Chemical Society **125**, 5636 (2003).

[6]   L. X. Zheng, M. J. O'Connell, S. K. Doorn, et al., Nature Materials **3**, 673 (2004).

[7]   B. H. Hong, J. Y. Lee, T. Beetz, et al., Journal of the American Chemical Society **127**, 15336 (2005).

[8]   H. W. Zhu, C. L. Xu, D. H. Wu, et al., Science **296**, 884 (2002).

[9]   Y. Ando, X. Zhao, H. Kataura, et al., Diamond and Related Materials **9**, 847 (2000).

[10]   Y. Ando, X. Zhao, H. Shimoyama, et al., International Journal of Inorganic Materials **1**, 77 (1999).

[11]   K. Q. Xiao and L. C. Zhang, Journal of Materials Science **40**, 6513 (2005).

[12]   B. H. Hong, J. P. Small, M. S. Purewal, et al., Proceedings of the National Academy of Sciences of the United States of America **102**, 14155 (2005).

[13]   S. M. Huang, B. Maynor, X. Y. Cai, et al., Advanced Materials **15**, 1651 (2003).

[14]   S. K. Doorn, L. X. Zheng, M. J. O'Connell, et al., Journal of Physical Chemistry B **109**, 3751 (2005).

[15]   S. M. Huang, M. Woodson, R. Smalley, et al., Nano Letters **4**, 1025 (2004).

[16]   E. Lahiff, C. Y. Ryu, S. Curran, et al., Nano Letters **3**, 1333 (2003).

[17]   K. Hata, D. N. Futaba, K. Mizuno, et al., Science **306**, 1362 (2004).

[18]   Z. F. Ren, Z. P. Huang, J. W. Xu, et al., Science **282**, 1105 (1998).

[19]   Z.-h. Yuan, H. Huang, L. Liu, et al., Chemical Physics Letters **345**, 39 (2001).

[20]   H. Ago, J. Qi, K. Tsukagoshi, et al., Journal of Electroanalytical Chemistry **00**, 1 (2002).

[21]   S. Fan, W. Liang, H. Dang, et al., Physica E: Low-dimensional Systems and Nanostructures **8**, 179 (2000).

[22]   S. S. Fan, M. G. Chapline, N. R. Franklin, et al., Science **283**, 512 (1999).

[23]   S. K. Biswas, R. Vajtai, B. Q. Wei, et al., Applied Physics Letters **84**, 2889 (2004).

[24]   B. Q. Wei, R. Vajtai, Y. Jung, et al., Chemistry of Materials **15**, 1598 (2003).

[25]   B. Q. Wei, R. Vajtai, Y. Jung, et al., Nature **416**, 495 (2002).

[26]   O. A. Shenderova, V. V. Zhirnov, and D. W. Brenner, Critical Reviews in Solid State and Materials Sciences **27**, 227 (2002).

[27]   W. Z. Li, S. S. Xie, L. X. Qian, et al., Science **274**, 1701 (1996).

[28]   Z. Y. Juang, I. P. Chien, J. F. Lai, et al., Diamond and Related Materials **13**, 1203 (2004).

[29]   Y. Murakami, S. Chiashi, Y. Miyauchi, et al., Chemical Physics Letters **385**, 298 (2004).

[30]   W. D. Zhang, Y. Wen, J. Li, et al., Thin Solid Films **422**, 120 (2002).

[31]   P. Avouris, Chemical Physics **281**, 429 (2002).

[32]   A. Modi, N. Koratkar, E. Lass, et al., Nature **424**, 171 (2003).

[33]   Y. C. Chen, N. R. Raravikar, L. S. Schadler, et al., Applied Physics Letters **81**, 975 (2002).

[34]   P. L. Chen, J. K. Chang, C. T. Kuo, et al., Diamond and Related Materials **13**, 1949 (2004).

[35]   M.-K. Li, M. Lu, L.-B. Kong, et al., Materials Science and Engineering A **354**, 92 (2003).

[36] J. B. Bai, Materials Letters **57**, 2629 (2003).

[37] Y. F. Mei, X. L. Wu, X. F. Shao, et al., Physics Letters A **309**, 109 (2003).

[38] M. J. Kim, T. Y. Lee, J. H. Choi, et al., Diamond and Related Materials **12**, 870 (2003).

[39] J. Zhao, Q. Y. Gao, C. Gu, et al., Chemical Physics Letters **358**, 77 (2002).

[40] X. Wang, Z. Hu, Q. Wu, et al., Catalysis Today **72**, 205 (2002).

[41] J. Haruyama, I. Takesue, S. Kato, et al., Applied Surface Science **175-176**, 597 (2001).

[42] G. L. Hornyak, A. C. Dillon, P. A. Parilla, et al., Nanostructured Materials **12**, 83 (1999).

[43] S.-H. Jeong and K.-H. Lee, Synthetic Metals **139**, 385 (2003).

[44] L. P. Biro, R. Ehlich, Z. Osvath, et al., Materials Science & Engineering C-Biomimetic and Supramolecular Systems **19**, 3 (2002).

[45] C. Papadopoulos, A. J. Yin, and J. M. Xu, Applied Physics Letters **85**, 1769 (2004).

[46] Y. Murakami, S. Yamakita, T. Okubo, et al., Chemical Physics Letters **375**, 393 (2003).

[47] N. Petkov, S. Mintova, K. Karaghiosoff, et al., Materials Science and Engineering: C **23**, 145 (2003).

[48] L. Huang, W. S. J, and S. P. O'Brien, Nano Letters **3**, 299 (2003).

[49] T. Wang, X. Y. Liu, D. Y. Zhao, et al., Chemical Physics Letters **389**, 327 (2004).

[50] E. Munoz, D. Coutinho, R. F. Reidy, et al., Microporous and Mesoporous Materials **67**, 61 (2004).

[51] J. Zhu, M. Yudasaka, and S. Iijima, Chemical Physics Letters **380**, 496 (2003).

[52] C. Kufazvinei, R. W. Leahy, S. M. Lipson, et al., (International Society for Optical Engineering, Bellingham WA, WA 98227-0010, United States, Dublin, Ireland, 2005), Vol. 5824, p. 149.

[53] J. B. Bai, A.-L. Hamon, A. Marraud, et al., Chemical Physics Letters **365**, 184 (2002).

J. H. Bai, Scientia Sinica 37, 3679 (2002).

Y. S. Mao, X. Li, W. Li, J. F. Shen, et al., Physics Letters A 304, 169 (2002).

M. L. Zhao, L. Li, J. S. Li, R. Chen, et al., Physical and Chemical Sciences B, 109 (2002).

C. Luo, J. Xu, L. Ding, C. Shen, et al., Chemical Physics Letters (2003).

X. Wang, L. Hu, F. Yu, Z. Qi, et al., Physical Review Letters 20, 3 (2002).

D. P. Qian, H. J. Kang, S. Kato, et al., Applied Surface Science (2002) (2001).

C. Z. Zhang, W. C. Zhang, C. Pantano, et al., Microelectronics Journal (1999).

L. G. F. Zhang, et al., Journal of Physics and Chemistry of Solids (2001), P. L. Yang, W. Huang, Y. Yang, et al., Materials Science and Engineering C (2004).

Bioinformatics and Nanomolecular Systems 19, 1 (2002).

C. Pantano, L. Z. Xia, L. Z. Xu, Applied Physics Review 85, 769 (2004).

W. Wang, et al., Z. Zhang, M. Kobe, et al., Chemical Physics Letters 375, 353 (2002).

X. Lou, L. Li, R. Jia, H. J. Gao, et al., Materials 48, 2, 279, Journal of Inorganic Materials 3, 144 (2002).

E. Zhang, W. H. Zhang, Microelectronics Engineering (2002).

R. Motoo, M. Hirata, Inorganic Materials A 86-086, 43 (2004).

R. Mutoo, D. Capelle, JP et al., Advanced Materials 1456 (2001).

S. Yoshida, M. Hayashi, Y. Kato, X. K. Xu, et al., J. Phys. D (2003).

C. Khachton, R. W. Larsen, B. J. Jasan, et al., International Journal of Oxygen Engineering for Integration (2004), K. Hata, et al., Chemical Science, Nature (2004).

H. Leisch, C. Wu, N. Lima, et al., Nano Letters 3, 1251 (2003).

F. H. Zhang, R. Russ, et al., et al. Biomaterials (2003), 4589, 865 (2003).

Z. F. Ren, Z. P. Huang, J. W. Xu, et al., Science 282, 1105 (1998).

Z. H. Yuen, H. Huang, L. J. M, et al., Chemical Physics Letters 348, 38 (2001).

H. Ago, J. Qi, K. Tsukagoshi, et al., Journal of Electroanalytical Chemistry (2002).

S. Fan, W. Liang, H. Cheng, et al., Physics E: Low-dimensional Systems and Nanostructures 4, 119 (2003).

S. Fan, M. G. Chapline, N. R. Franklin, et al., Science 283, 512 (1999).

S. Q. Brown, R. Valko, G. G. Wei, et al., Applied Physics Letters 84, 2382 (2004).

B. Q. Wei, R. Vajtai, Y. Jung, et al., Chemistry of Materials 15, 1598 (2003).

B. Q. Wei, R. Vajtai, Y. Jung, et al., Nature 416, 495 (2002).

D. N. Shishekova, N. H. Zhirnov, and D. W. Brenner, Critical Reviews in Solid State and Materials Sciences 27, 227 (2002).

W. Z. Li, S. S. Xie, L. X. Qian, et al., Science 274, 1701 (1996).

A. Y. Zhang, H. Q. Chen, J. P. Lin, et al., Diamond and Related Materials 12, 1201 (2003).

Y. Murakami, S. Chiashi, Y. Miyauchi, et al., Chemical Physics Letters 385, 298 (2004).

W. Z. Zhang, Y. Wen, S. Y. Li, et al., Chinese Physics 583, 159 (2004).

S. Fan, et al., Chemical Physics 261, 439 (2003).

A. Fonseca, K. Kemenski, et al., Carbon in the bulbs 43, 6, 593 (2003).

Y. Li Chen, N. R. Franklin, J. S. Schindler, et al., Applied Physics Letters 81, 975 (2003).

E. N. Chen, J. H. Zhang, G. T. Kim, et al., Diamond and Related Materials 12, 1040 (2003).

D. Xu, H. M. Liu, L. H. Kang, et al., Materials Science and Engineering 34, 254 (2002).

Chapter 6 Characterisation and optimisation of MWNT junction arrays

6.1 Introduction

This chapter aims to describe the process undertaken from the initial discovery of the ability to grow junction-structure CNTs to the optimisation of their growth. Section 6.2 deals the initial growth of MWNT junctions on porous silica and alumina substrates as well as roughened Si. The growth of ordered arrays of straight and junction-structure MWNTs on various geometries of trench-etched Si is discussed in Section 6.3. In Section 6.4 the optimisation of the linear density and proportion of junctions in the arrays through control of initial conditions will be discussed. Section 6.5 discusses a model for the growth of these arrays. This growth model is divided into several parts: catalyst positioning, the growth of the CNTs themselves, junction formation and CNT growth termination. The Raman spectroscopy of the arrays is covered in Section 6.6. Section 6.7 wraps up the chapter.

6.2 Growth of MWNT junctions on various substrates

The first junction-structure MWNTs of this project were observed on the surface of porous alumina membranes (PAMs) that had been filled with Fe catalyst. The structures occurred within large defects (holes/pits) on the surface of the PAMs (Figure 6-1). The tubes are seen to span from one side of the defect to the other. The CNTs shown in these micrographs were grown at 800°C under a 50 sccm (standard cubic centimetres per

minutes) flow of C_2H_2 for 60 minutes. The tubes are several microns long and $30 - 40$ nm diameter. In addition to individual straight tubes spanning such defects; Y-junctions and more complex junctions, such as X-junctions were observed (Figure 6-1).

Further experimentation with these PAM substrates revealed the formation of junction-structure CNTs not only in holes in the surface, but also from regions raised above the substrate surface. Figure 6-2 shows two separate MWNT junctions suspended above the PAM surface having grown from Fe containing detritus; most likely broken shards of PAM scattered on the surface during cutting.

Similar junction-structures were seen among CNT growth on mesoporous silica indicating that the formation of junctions appears to be relatively independent of substrate choice (Figure 6-3). In this case the junction-structures are suspended from catalyst islands that have pooled on the silica surface.

The common factor in the physical morphology of these three examples of junction growth is the presence of discrete catalyst regions raised above the adjoining substrate surface. This allows for CNTs to grow out into "open space" without being impeded by surface interactions.

A plain silicon surface was prepared by roughly scoring it with small grain sandpaper. The scratched substrate surface was then treated with a polystyrene-polyvinylferrocene (PS-PVF) solution in toluene as outlined in Chapter 3. After CVD treatment of these samples significant numbers of branched CNT structures were observed to grow from the ridges on the substrate (Figure 6-4). These results are in agreement with similar work reported in the literature.[1, 2]

The next step was to endeavour to grow these structures in a more controlled fashion that could afford control over their position, alignment and the frequency with which they occur. To achieve this; CNTs were grown on patterns of trench arrays etched in to Si wafers.
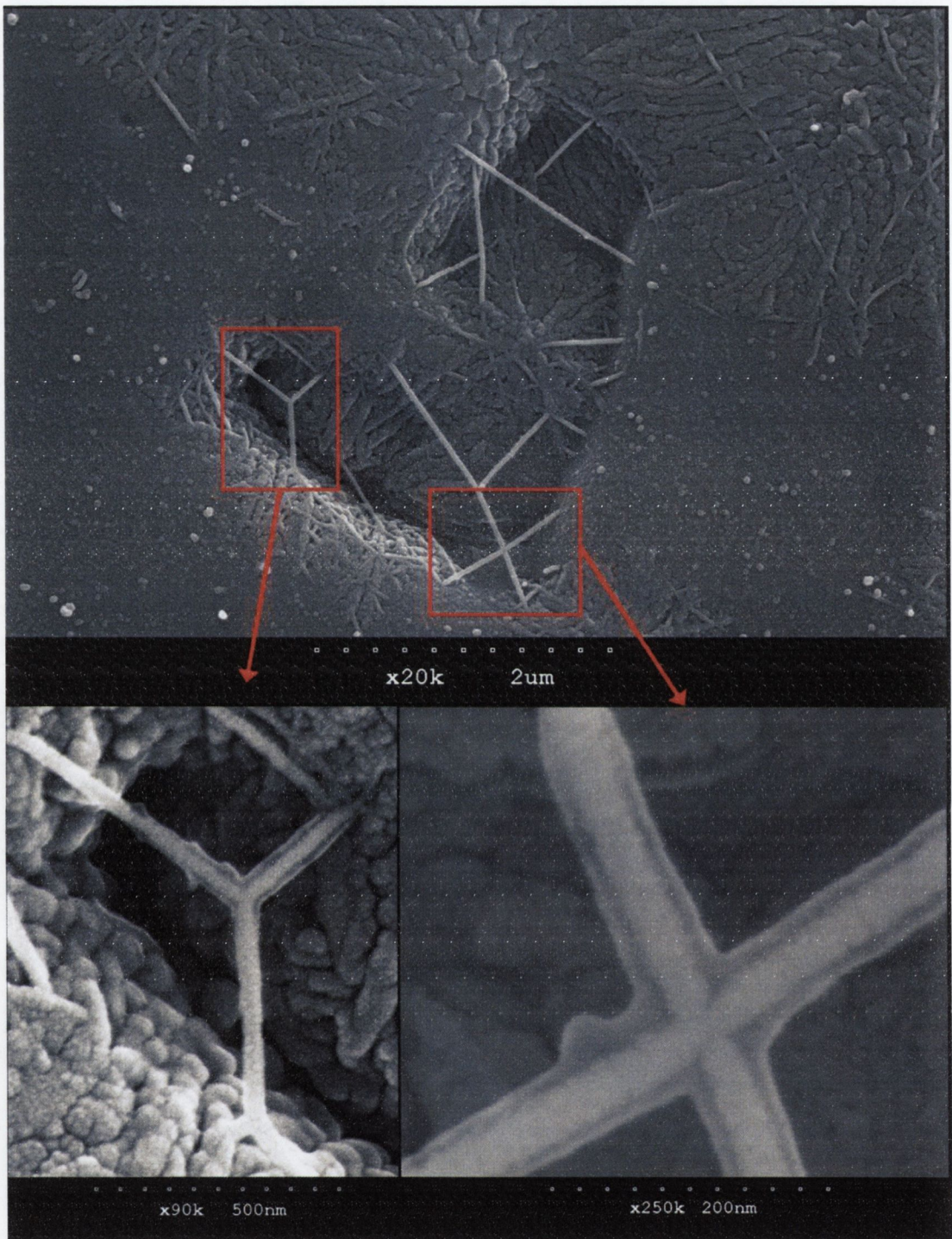
Figure 6-1 SEM micrograph of CNT junctions grown on a PAM substrate. The insets show a CNT Y-junction and four-way cross respectively. The tubes were grown under the following conditions: Temp= 800°C, Ar flow= 50 sccm, C_2H_2 flow = 500 sccm, time= 60 minutes.
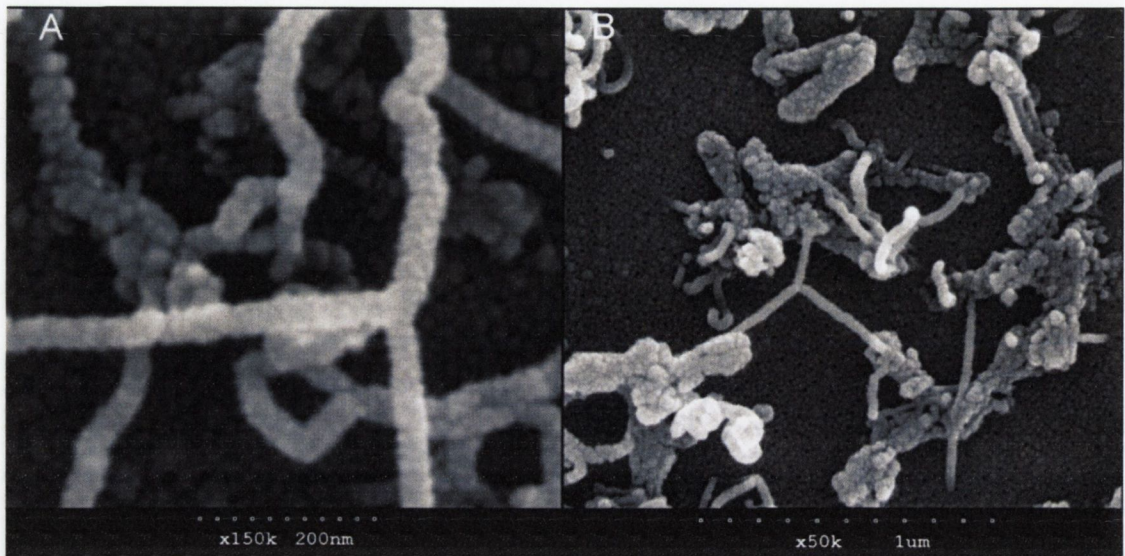
Figure 6-2 SEM image showing two separate Y-junctions grown from raised areas of PAM surface. The tubes were grown under the following conditions: Temp= 800°C, Ar flow= 80 sccm, C₂H₂ flow = 800 sccm, time= 60 minutes.
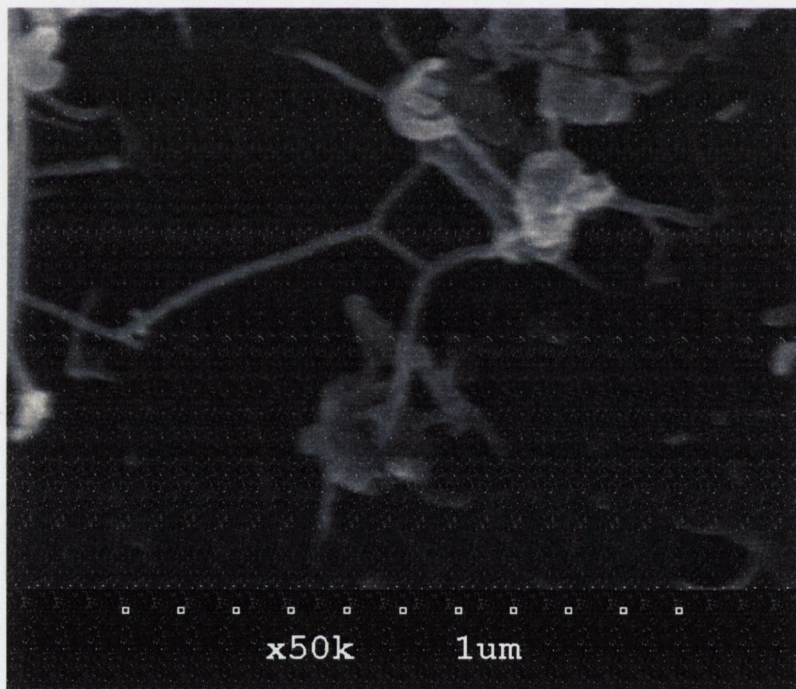
Figure 6-3 SEM Micrographs showing a CNT double-Y-junction grown from raised regions on the surface of mesoporous silica. In this case the catalyst is Co which has leaked onto the surface (see chapter 5, section 5.2.3). The tubes were grown under the following conditions: Temp= 800°C, Ar flow= 50 sccm, C₂H₂ flow = 500 sccm, time= 60 minutes.
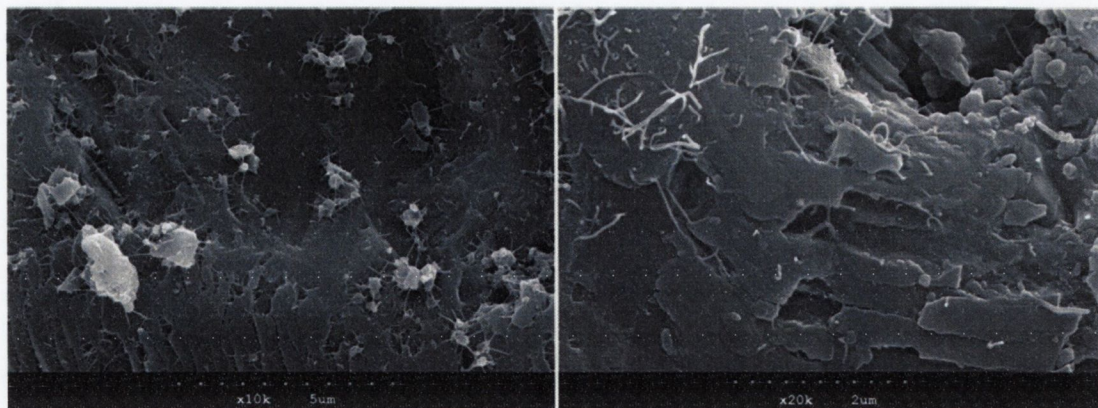
Figure 6-4 SEM micrograph showing interconnecting and junction-type structure tubes grown on a roughened silicon surface.

6.3 Growth of CNT arrays on patterned silicon

Tests were carried out on trench etched Si substrates treated with either evaporated catalyst or drop-cast with high concentrations of PS-PVF catalyst solution. Experiments yielded mixed results. While MWNTs were observed to span the trenches they were randomly aligned and no junction-structures were found after thorough SEM examination. It appeared that a lower yield of nanotubes was required. As a result the following experiments were carried out using low concentrations of catalyst solution (<0.5%).

After an in-depth, systematic study of the effects of CVD conditions it became possible to produce dense arrays of MWNT "interconnects" (Section 6.4). These interconnects form as bridges across the etched trenches. The arrays were seen to have relatively high proportions of junction-structure CNTs. Figure 6-5 shows an SEM image of a trench etched region after CVD, the bright lines are the ridges between the trenches while the darker lines are the bottom of the trenches. As can be seen both straight and branched CNTS grow across the trenches as interconnects, with a relatively high proportion being branch-type tubes. The CNTs shown in Figure 6-5 were grown through thermal decomposition of acetylene with a flow rate of 500 sccm for 60 minutes at 800°C mixed with argon flowing at 5000 sccm. The sample was left in the reaction chamber for 120 minutes at 800°C in an argon atmosphere. The trenches in the region measured were 420 nm wide, and a 0.1% catalyst solution was drop cast and dried on the substrate surface prior to the experiment. This resulted in an average interconnect growth density of ~0.6 interconnects per micron of trench length with 18% of the total interconnects being of junction-structures.

The majority of the branch-structure MWNTs grown during these experiments are Y-junctions similar to those shown in the insets of Figure 6-5. However in many cases

structures with multiple junctions and branches have been recorded (Figure 6- 6), though they occur much less frequently.

While the study of CVD conditions did concentrate on growth over equally spaced trenches, other substrate morphologies were attempted. Bridging CNT structures were grown from raised pillars (Figure 6-7) similar to those used by Hongjie Dai's Stanford group.[23, 3] However the CNT production method presented here produces nanotubes that grow exclusively from the edges of the raised features. A number of branched structures with each branch terminating on a separate pillar were seen on these samples (Figure 6-7, inset).

Figure 6-8 shows CNTs bridging gaps ranging from 170 nm to 1.5 µm in width. This image demonstrates that tubes can bridge a range of widths, edge to edge, with the tube length being controlled by the width of the gap. However, wide trench of ~1µm and above tend to yield lower numbers of bridging tubes. In these cases, a significant number of tubes can be seen to incompletely bridge the gap, terminating on the lower level of the trench. This is seen in the right hand section of Figure 6-8. To avoid this effect the study of input conditions focused on trench widths of ~500 nm and below.
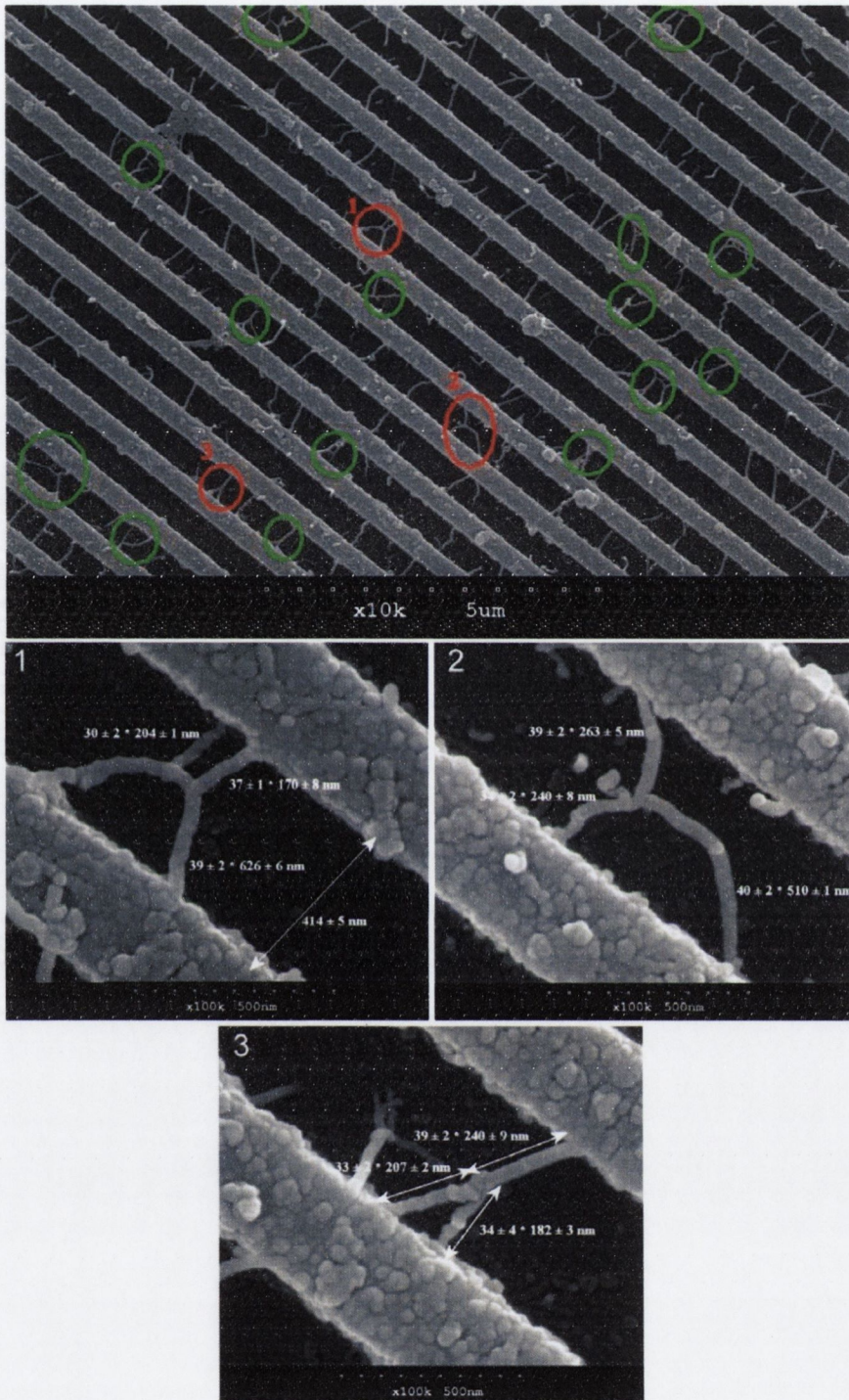
Figure 6-5 SEM showing an array of CNTs growing from the edges of trenches. Junction-structure interconnects are highlighted with circles, and selected junctions (1-3) are shown below the main image. The tubes were grown under the following conditions: Temp= 800°C, Ar flow= 50 sccm, C₂H₂ flow = 500 sccm, time= 60 minutes.
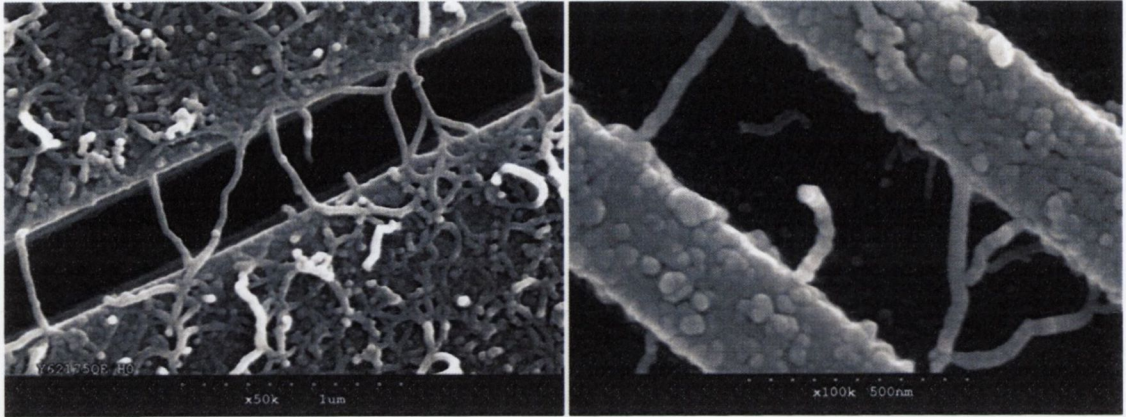
Figure 6-6 SEM micrographs showing examples of multiple-junction CNTs bridging trenches.
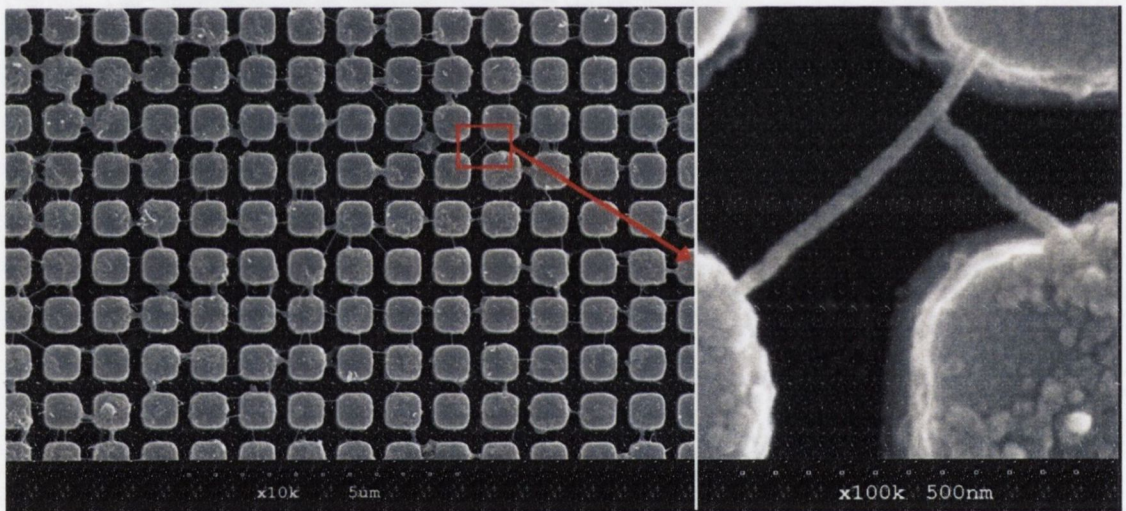
Figure 6-7 SEM micrograph showing an array of connecting tubes which bridge raised SiO₂ islands (on an Intel® test-chip). The Inset shows a Y-junction straddling three separate islands. The tubes were grown under the following conditions: Temp= 600°C, Ar flow= 500 sccm, C₂H₂ flow = 50 sccm, time= 30 minutes.
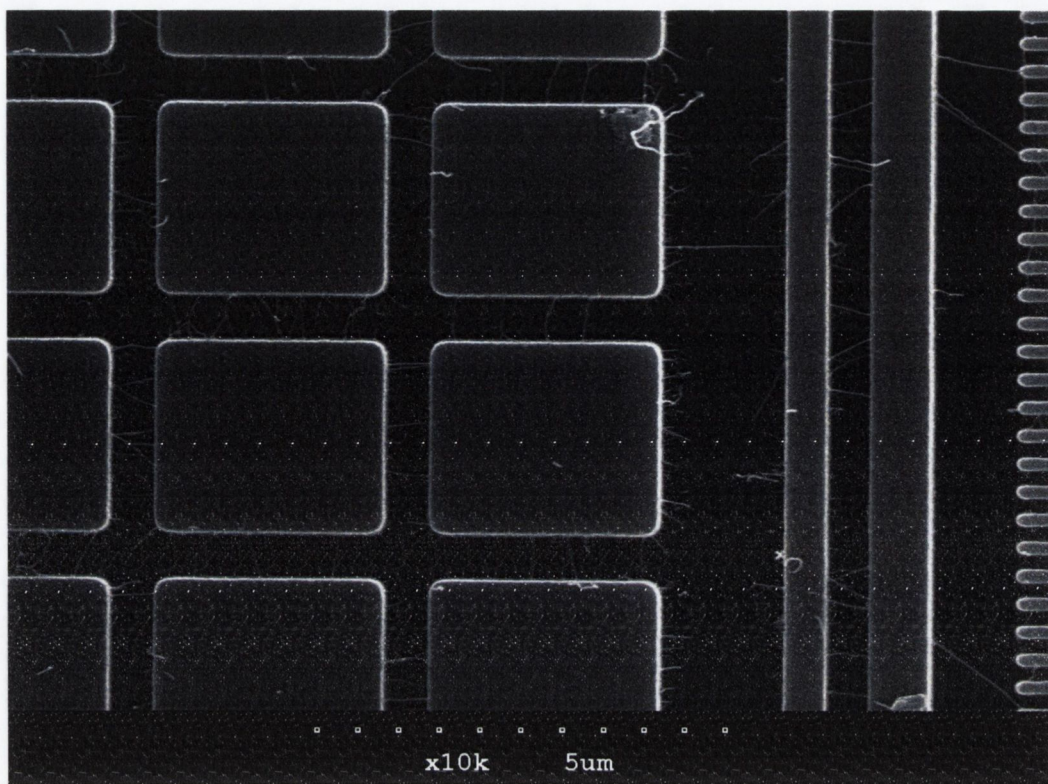
*Figure 6-8 SEM micrograph showing an array of connecting tubes on an Intel® die. Tubes bridge a variety trench widths ranging from 170nm to 1.5μm. The tubes were grown under the following conditions: Temp= 600°C, Ar flow= 500 sccm, C_2H_2 flow = 50 sccm, time= 30 minutes.*

It can be seen from Figure 6-9 that with correct catalyst patterning, multi-level arrays of bridging nanotubes are possible. This broadens the range of possible applications beyond that of simple 2-D arrays.
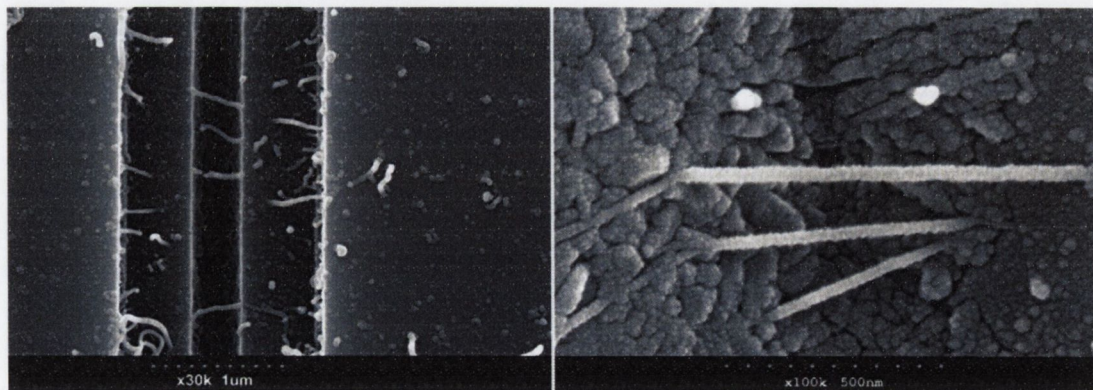
Figure 6-9 SEM micrographs showing examples of multi-level growth. Three-dimensional arrays of straight bridging carbon nanotubes on etched Si (left) and PAM (right) can be grown.

6.4 A systematic study of the effects of initial conditions on CNT array characteristics

In order to understand the growth mechanisms of CNT interconnect arrays and ascertain optimum growth conditions a systematic study was carried out. Each of the controllable test conditions (trench width, C_2H_2 flow rate, C_2H_2 flow time, catalyst solution concentration; and reaction temperature) were varied and the effects on the resultant CNT arrays (diameter, junction-angle, overall interconnect density per unit trench length and percentage branch-structure tubes) were measured. This analysis yielded several notable results.

A correlation of all data collected for CNT diameters and junction-angles (Figure 6-10) shows that over all conditions the average tube diameter as measured in the high resolution SEM is $30 - 45$ nm. However when one accounts for the gold layer sputtered onto counteract charging effects during electron microscopy the average diameter is reduced to be between $20 - 35$ nm. This is in agreement with TEM investigations of MWNTs grown in the custom built CVD system. The overall trend for junction-structure angles is not as sharp but shows that the majority are between $60 - 90°$, which correlates well with what is reported elsewhere.[26, 1, 4]

The matrix graph shown in Figure 6-11 plots each of the conditions: flow time, reaction temperature, acetylene flow rate, catalyst concentration, and trench width, along with the measured results: linear density of bridging CNT structures and proportion of branched CNT structures against each other. The latter two characteristics are used to define a qualitative feel for the quality of the CNT array. This method of displaying data allows one to get an overview of the impact of each component. From this starting point any individual relation ship can then be examined in more detail.

A simple plot of the linear density of all bridging structures per unit length of trench against the proportion of the structures that display branching shows a positive slope (Figure 6-12). In other words: as the percentage of junction-structure MWNTs in the array increases, so too, does the total number of bridging MWNT structures. This is in agreement with the intuitive reasoning that the more CNTs there are in the array the more possibilities for having branched structures exist.
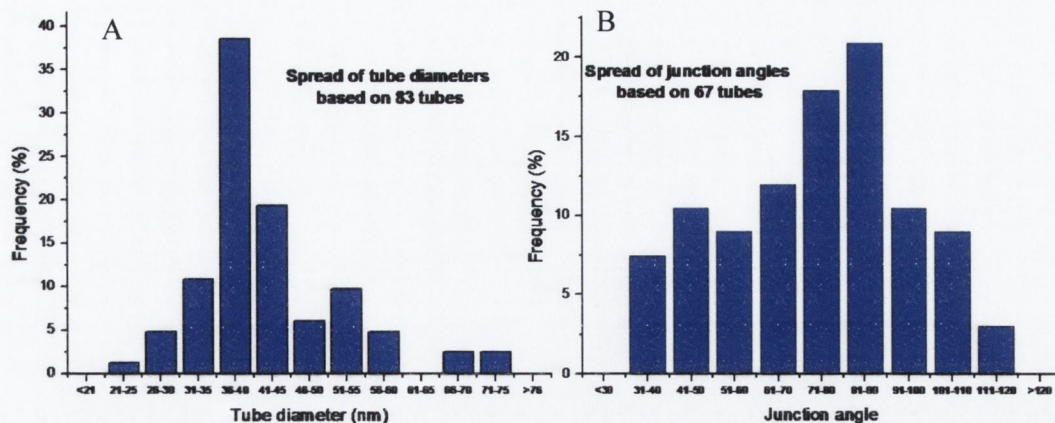
Figure 6-10 Statistical frequency of A) MWNT diameter (including gold coating (10 nm) to prevent charging effects during SEM) and B) junction-angle, taken for a variety interconnects over all tested growth conditions.

Temperature was found to have a strong affect on the CNT arrays. It was noted that both the number of interconnects per μm and the proportion of branch-structures increased with decreasing temperature over the range measured (Figure 6-13).

At lower temperatures the carbon feedstock molecules (C_2H_2) will not disassociate as readily as at higher temperatures. Combined with this the mobility of catalyst islands will be reduced so that they cannot form iron carbide solution as easily. This leads to a slower growth rate for the CNTs and will result in a greater amount of kinking and bending. Since the probability of having defects in carbon nanotubes increases with decreasing temperature, so too does the probability of forming junctions (see the proposed growth mechanism in section 6.5).
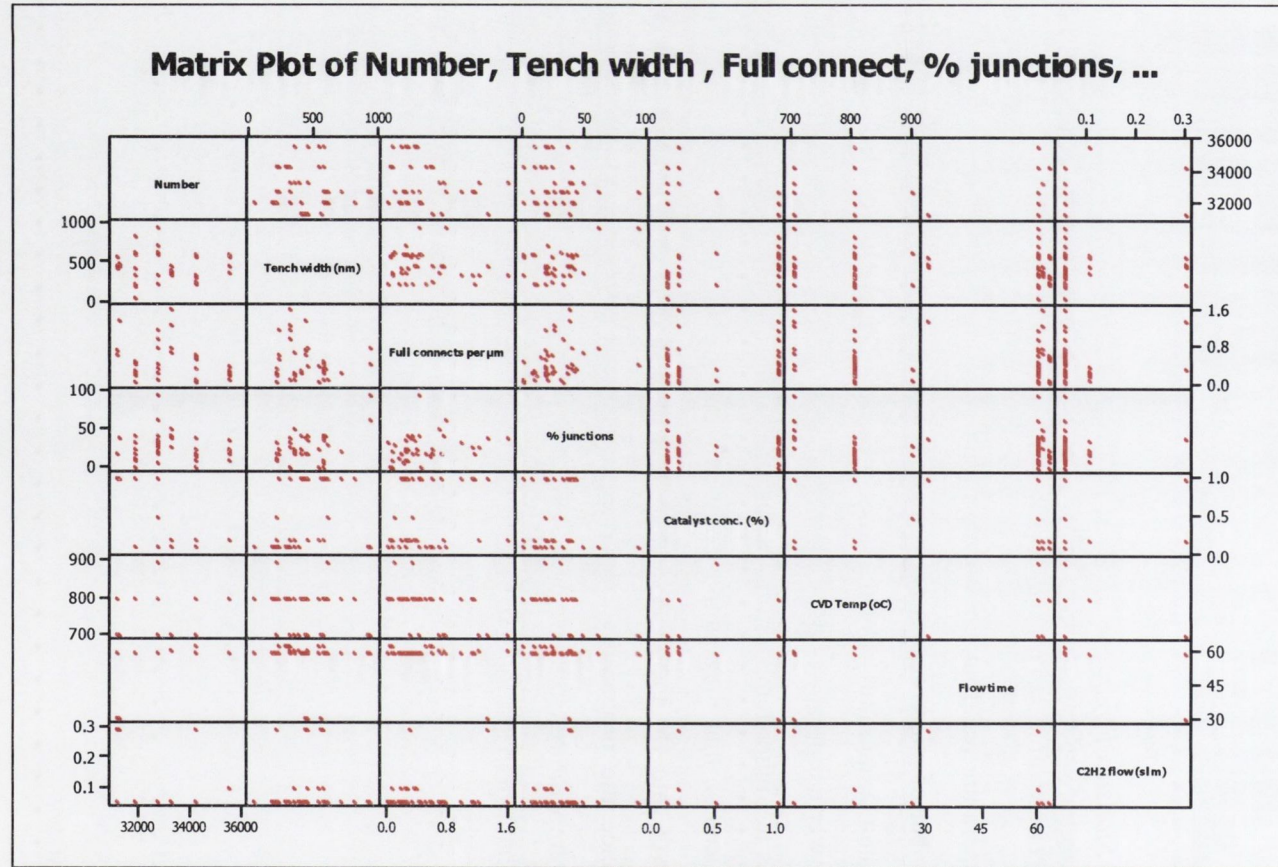
Figure 6-11 Matrix plot of all initial conditions and measured array characteristics used during the systematic study.

Figure 6-12 Scatter plot of the linear density of the total number bridging interconnects per unit length of trench against the proportion of them that are branched, junction-structure CNTs.

The decrease in growth rate with decreasing temperature may also account for the increase in the number of bridging CNT structures per unit length. The slower the tubes grow, the more time it has to anchor to the opposite side of the trench. The decrease in decomposition of the acetylene could also lead to lower rates of premature termination of CNT growth due to carbon poisoning.[5]
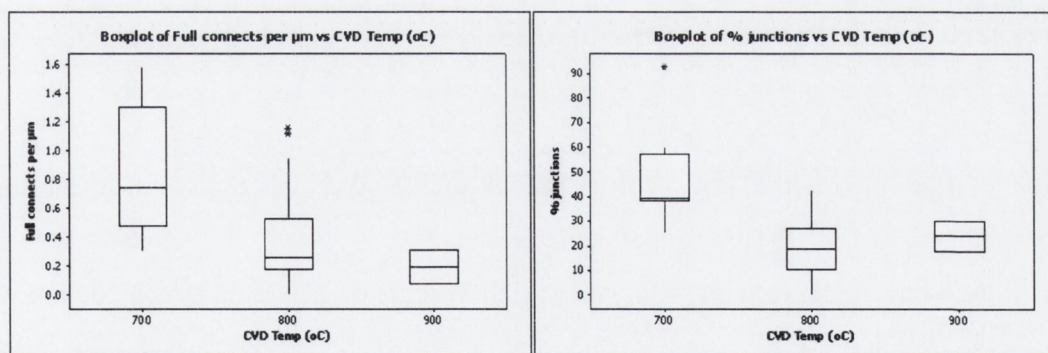
Figure 6-13 Statistical plots over all conditions of the linear density of the total number bridging interconnects per unit length of trench (left) and the proportion of them that are branched, junction-structure CNTs (right) with respect to CVD temperature.

One of the qualitative findings of this study is that trench width was seen to play a role in positioning of the grown tubes, for the larger widths (above about 500 nm) a substantial number of MWNTs were found on the floor of the trench and spanning from

trench top to trench floor. However, for trenches below about 500 nm wide it was observed that there is relatively sparse growth at the bottom of the trenches and that the vast majority of tubes grow on the tops of the trenches. The study also showed that while overall density of bridging tubes increased with decreasing trench width, the percentage of junction-structure CNTs is unaffected (Figure 6-14).
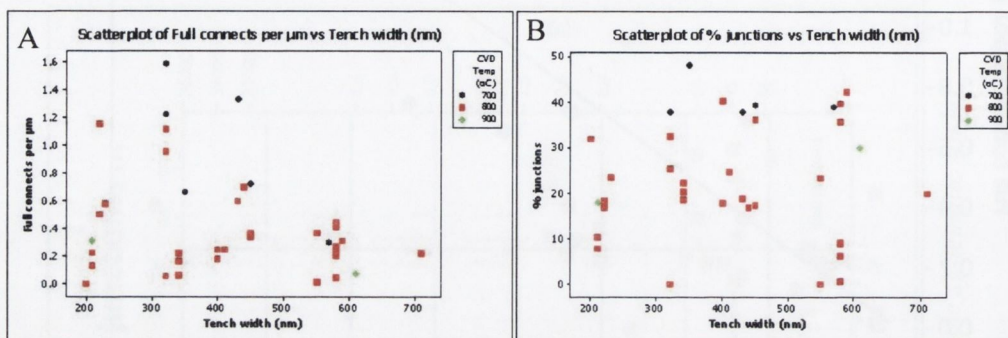
Figure 6-14 Scatter plots of trench width with respect to: (A) the linear density of total bridging interconnects per unit length of trench, and (B) the proportion of them that are branched.

The increase in the linear density of bridging CNT structures with decreasing trench width can be explained using simple geometry. Due to the non-laminar nature of the gas flow through the reaction chamber, there can often be a slight deviation in the growth direction from one CNT to the next. As can be seen in Figure 6-8 the bridging nanotubes are often not perpendicular to the walls of the trench, but lying diagonally across the trench. This results in the bridging tube structure having a length greater than the width of the trench. The length of a straight CNT growing diagonally across a given trench can be given as:

$$L_{tube} = W_{trench} \Big/ Sin\vartheta_{dev}$$

Where, L_{tube} is the length of the bridging CNT, W_{trench} is the width of the trench being bridged, and θ_{dev} is the angle of deviation.

As an example, consider a typical deviation angle of $30°$. For a trench 100 nm wide, the CNT would need to grow to 15.5 nm longer than the trench width in order to successfully bridge it, however for a trench 1 μm wide, a CNT deviated by the same angle would need to grow an additional 155 nm longer than the trench width. Thus it becomes clear that as the wider the trench is, the greater the increase in additional distance the CNT must traverse with increasing θ_{dev}.

It was noted that within the limits of this study the effects of acetylene flow on the CNT arrays proved inconclusive (Figure 6-15). Similarly the concentration of the catalyst

solution dropped, showed no obvious effect on either overall density of the array, or the percentage of junction-structures. Intuitively one would expect the array density to increase with both catalyst solution concentration (more growth sites) and acetylene flow (more carbon feedstock). However, the criteria for the measurement of array characteristics required that CNTs bridge from one wall of an individual trench to its opposite wall. If one considers the overall CNT growth then both acetylene flow and catalyst solution concentration, especially in combination do have a dramatic effect on the resultant CNTs. This is demonstrated in Figure 6-16, both samples were run at 700°C for 60 minutes. The CNTs in Figure 6-16 (A), were grown using a catalyst solution concentration of 1% and a acetylene flow of 300 sccm, and those in Figure 6-16 (B) were grown using a catalyst solution concentration of 0.2% and a acetylene flow of 50 sccm. The CNTs in Figure 6-16 (A) form a dense and unaligned forest in which no bridging CNT structures were observed, the CNTs in Figure 6-16 (B) however are shown to form an array of interconnect type CNTs with a good proportion of junction-structures.

Although Acetylene flow and catalyst solution concentration do not have any notable effect on the characteristics of the arrays, the correct choice of each of these initial conditions is essential for the formation of ordered arrays as opposed to randomly aligned CNT mats.
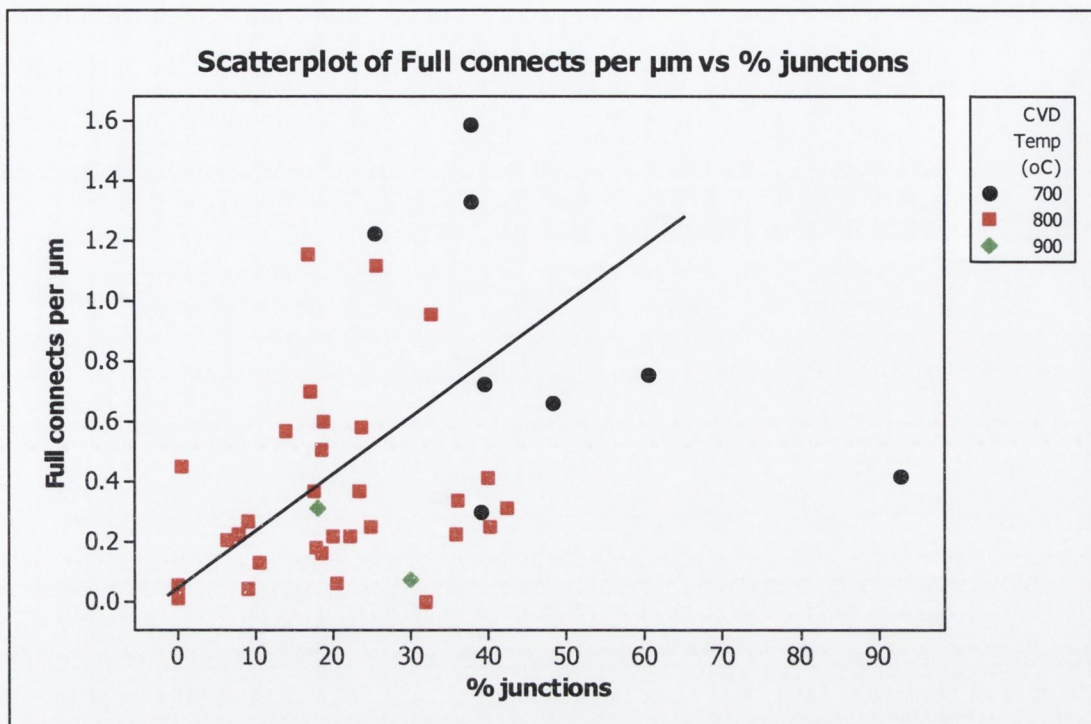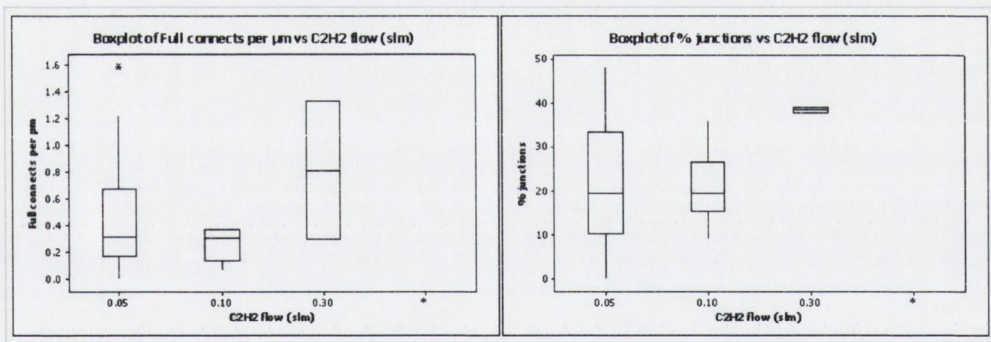

Figure 6-15 Box plots showing the effect of acetylene flow during CVD on the linear density of the total number bridging interconnects per unit length of trench (left) and the proportion of them that are junction-structure CNTs (right) .

As a result of this systematic study the optimum initial conditions were chosen to be flow rate of 50 sccm mixed with argon flowing at 500 sccm at 700°C for 60 minutes. These conditions lead to a good quality array which has both a high linear density of bridging CNT structures (~1.6 interconnects per μm of trench length) and a high proportion of branched interconnect CNT structures (~38%). Figure 6-17, shows an example of an array grown under these conditions: 199 interconnects were measured over

a total combined trench length of 125.4 µm. A total of 76 branched structures were observed.
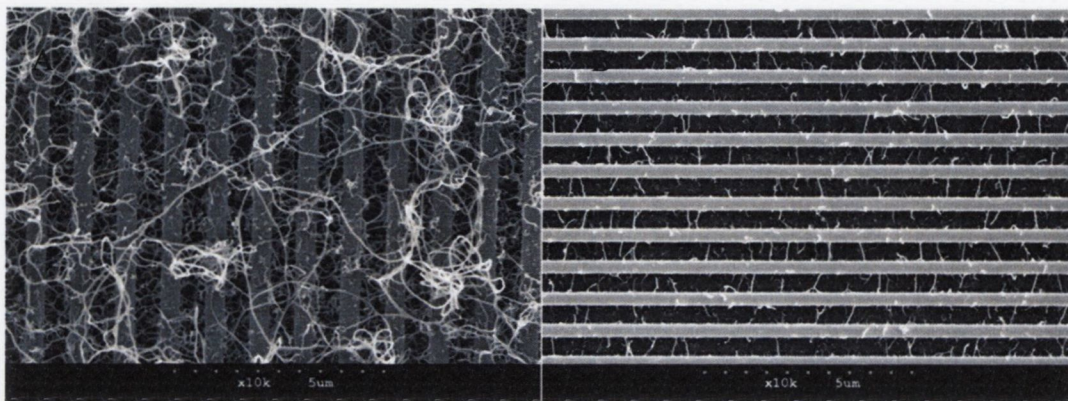
Figure 6-16 SEM micrographs of CVD grown CNTs. Both samples were grown at 700°C for 60 minutes. The CNTs in A) were grown using 1% catalyst solution and 300 sccm acetylene flow and those in B) were grown using 0.2% catalyst solution and 50 sccm acetylene flow.
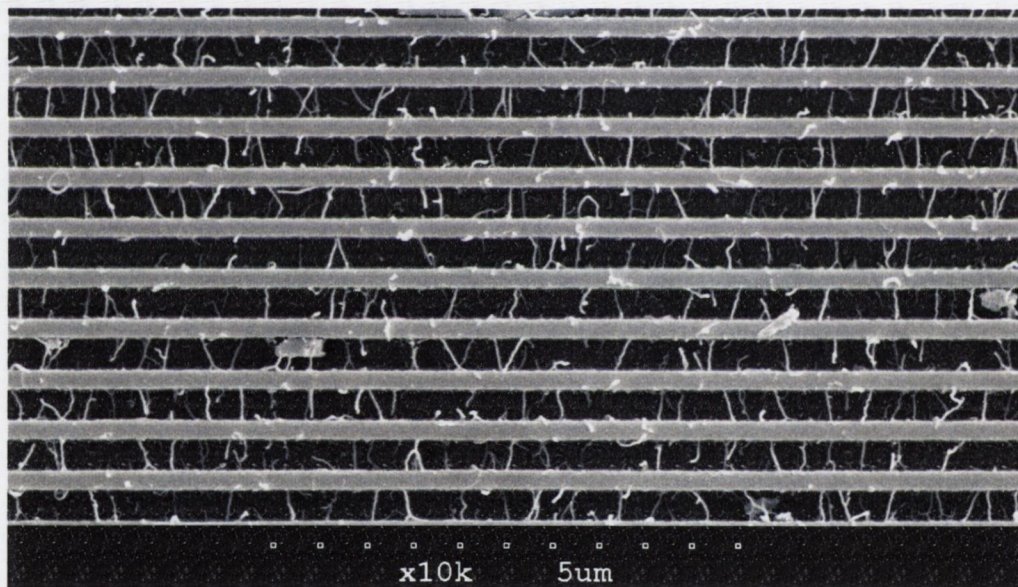
Figure 6-17 SEM image of an interconnect array grown under optimum conditions.

6.5 A model for the position and growth of arrays of straight and junction-structure bridging CNTs

In the following section the growth mechanism of the CNT arrays and specifically of the junction-structure CNTs will be outlined. The proposed mechanism consists of the following steps: Catalyst positioning, CNT initialisation, CNT growth, junction formation, and CNT growth termination.

6.5.1 Catalyst positioning

It can be clearly seen from the SEM micrographs shown in section 6.4 that CNTs in the arrays grow almost exclusively from the edges of trenches. This alignment of the CNTs arises from a self-positioning mechanism of the catalyst itself along the edges of the trench.

The self-alignment of the catalyst arises from the deposition method. The catalyst vehicle: PS-PVF is dissolved in toluene and simply drop cast onto the substrate surface. Toluene has a low surface tension and hence good wetting of the various substrate surfaces used. The contact angles for plain silicon with a native oxide, silicon with a thick oxide layer and silicon with silicon nitride layer (used in the Intel® test chips) (Figure 6-18) were measured as 4.2^{o}, 8.1^{o}, and 4.5^{o} respectively.
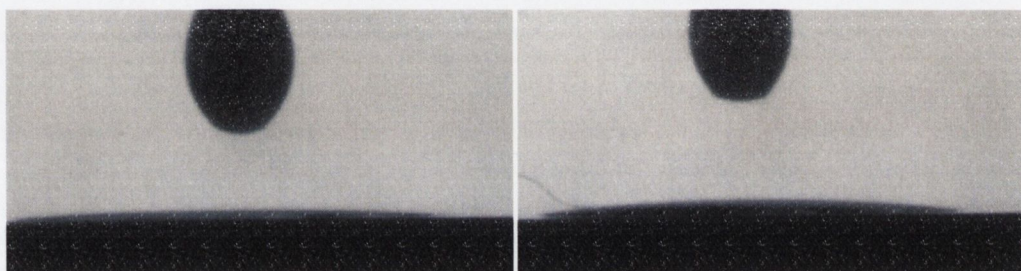
Figure 6-18 Optical images depicting the low contact angle and hence good wetting abilities of a drop of toluene on SiO$_2$ (left) and SiN (right).

A drop of catalyst solution placed on the surface of a smooth un-patterned substrate forms a circular bubble that is observed to dry from the centre out. This causes the catalyst dissolved in the toluene to be dragged towards the edge of the bubble, forming an iron-rich halo (Figure 6-19). EDX measurements on the outer ring show peaks for both iron and carbon, which are the heaviest and majority elements in PS-PVF respectively. The area within the halo shows negligible amounts of carbon and no noticeable iron peaks. The chlorine peak can be attributed to impurities in the toluene.

If CVD is carried out on a smooth substrate treated with catalyst in this manner the result is a black "coffee stain" effect of the same shape as the original catalyst halo. Raman measurements confirm the presence of CNTs in the outer ring. Significantly reduced or negligible CNT signals are measured from points within the circle (Figure 6-20).
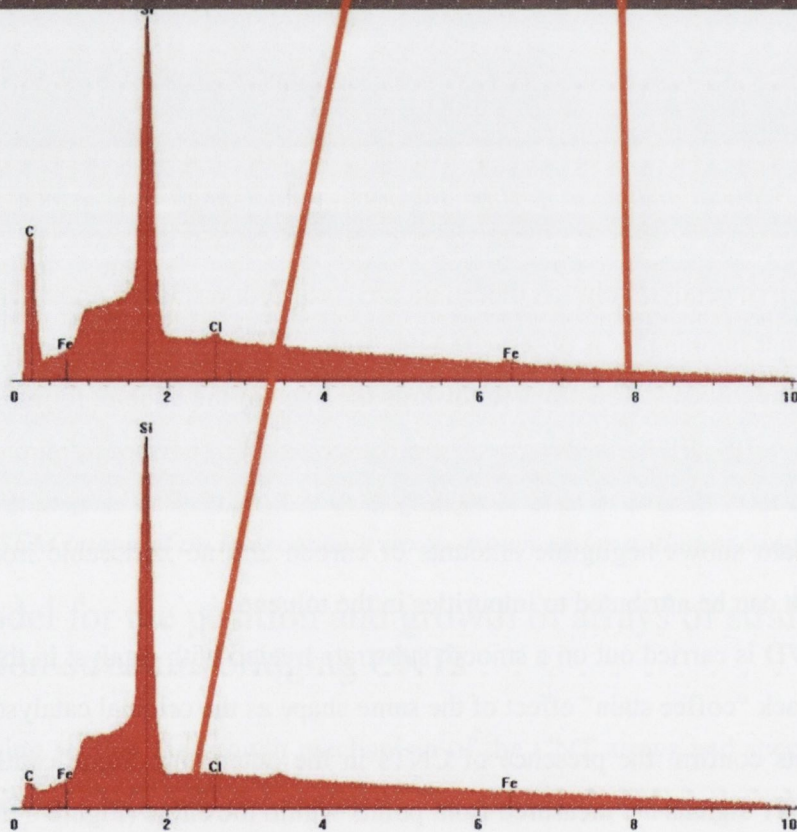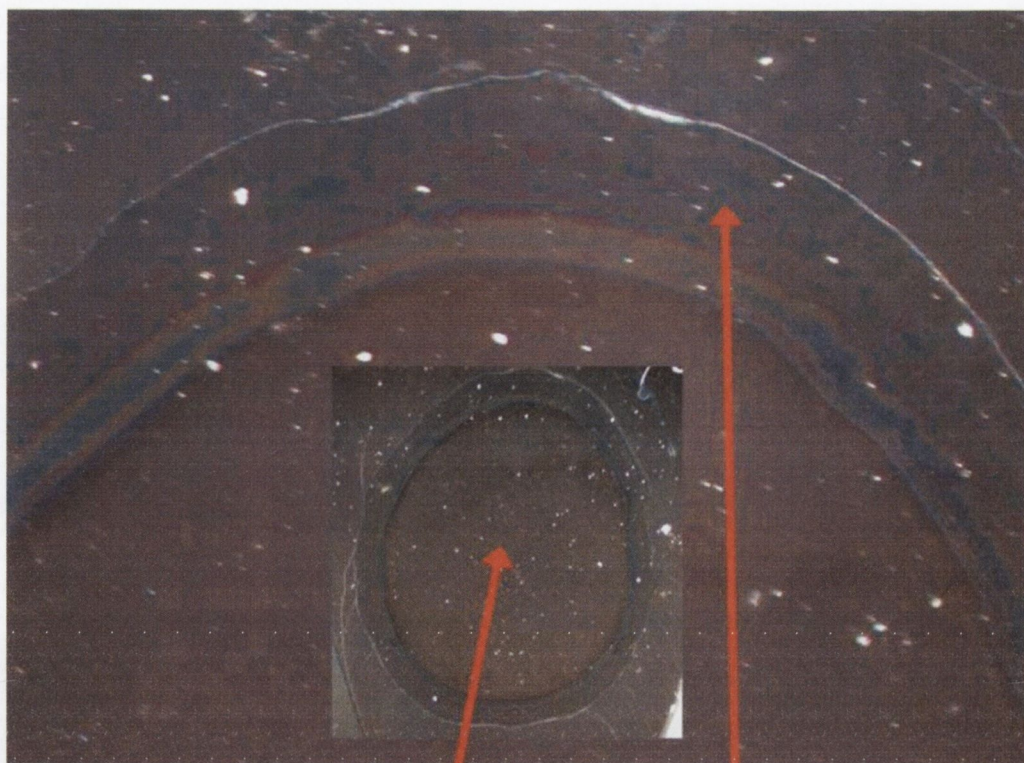
Figure 6-19 Optical micrograph showing the edge of "coffee-stain" pattern produced when the catalyst solution is drop-cast onto a silicon surface prior to CVD. EDX analysis shows that the edge of the ring contains Fe and C (from the polymer itself). These peaks are much weaker in the centre of the ring.

This self-positioning can be utilised in order to drag catalyst to specific sites on the substrate. The effect of placing a droplet of catalyst solution on a trench-etched substrate is to break the droplet up as it dries, with the result that each raised section acts as an independent substrate area. In this way, as the initial droplet dries it splits into smaller droplets, each of which dry on a separate raised section dragging the catalyst to the trench edge. A simple indication of this is that a ring shaped halo is not observed when catalyst is dropped on a patterned substrate as the splitting of the droplet causes the catalyst to be more evenly spread over the surface.
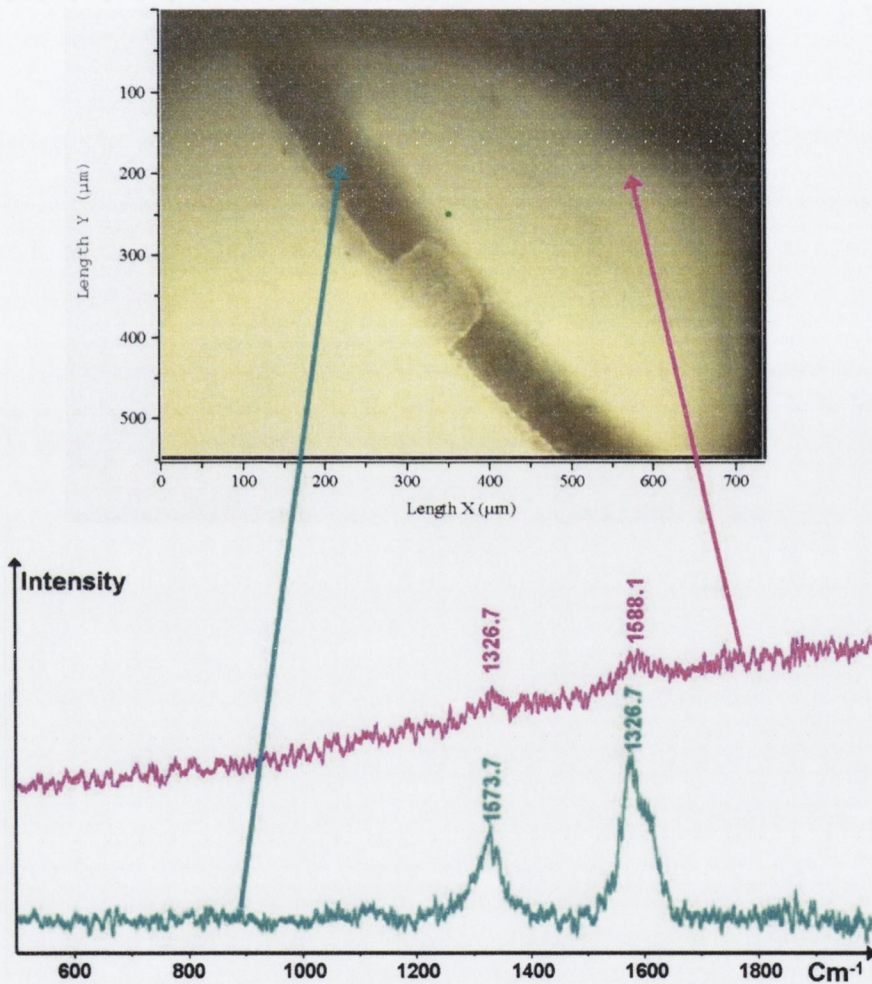
Figure 6-20 Optical micrograph depicting a section of the iron rich halo after CVD treatment. Raman analysis shows CNT peaks on the halo and greatly reduced peaks in the centre of the ring.

6.5.2 CNT growth

CNT growth occurs as the acetylene flows over the catalyst islands in the heated section of the CVD chamber.

At temperatures above ~650°C acetylene will thermally decompose without the presence of oxygen, into carbon and hydrogen. Any liberated carbon atoms incident on the heated catalyst islands will diffuse into and across the surface of the iron. Any non-decomposed acetylene molecules incident on a catalyst island will decompose on contact with the metal surface,[6, 7] releasing the hydrogen as H_2 gas and allowing the newly freed carbon to diffuse across the surface.

The growth of the nanotubes in this study is seen to occur via a tip growth mechanism.[7-13] Tip-growth involves the CNT growing up from beneath the catalyst metal and dragging a portion of it away in the tip of the tube. Proof of this is seen in Figure 6-21, this TEM micrograph shows two individual MWNTs (180 and 105 nm in length, with diameters of 32 and 33 nm respectively). Each end of the tubes is capped and there are catalyst particles at or near the ends of each CNT, showing that each tube has grown out of the catalyst island and dragged some of the iron with it. The left inset of Figure 6-21 gives a clear demonstration of elongation of the catalyst metal that is drawn up the core of the CNT.[14]
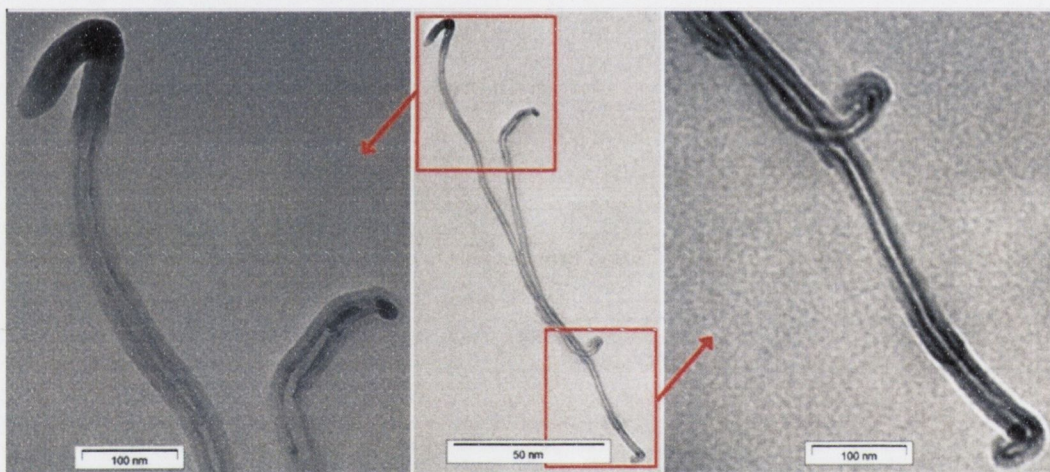
Figure 6-21 TEM micrographs of two individual MWNTs with insets (right and left) showing metal particles on both ends of the tubes suggesting a tip growth mechanism. Dark particles at the kinks suggest metal particles on the caught at the bend sites. The tubes were grown under the following the conditions: Temp= 700°C, Ar flow= 0.3 sccm, C_2H_2 flow = 1000 sccm, time= 60 minutes.

6.5.3 Junction formation

Kink formation

As can be seen from Figure 4.9 in Chapter 4 (section 4.2.2) the inlet pipes for each of the two gases used during CVD face each other, and both are perpendicular to the direction of the long furnace tube containing the samples to be treated. This set up leads to a non-laminar flow of gases through the reaction chamber.[25]

The chaotic flow of gases has several effects on the growing CNTs. Due to the positioning of catalyst material at the edge of trench the emerging CNT will grow out over the trench whereupon it will be suspended by the flow of gases though the chamber[32]. The gas flow will keep the tip of the tube suspended above the trench floor via a "kite mechanism".[10, 15]

While laminar flow of the carrier and reactive gases leads to long straight tubes[15-18] chaotic flow is more likely to lead to formation of kinked and bent CNTs.[25] The non-laminar flow can lead to an uneven mixing of gases giving rise to carbon-rich, and carbon deficient gas pockets. These in turn can lead to carbon under-supply and carbon over-supply on opposite sides of the CNT as it forms, inducing the formation of pentagon-heptagon kinks in the structure.[19]

As the nanotube grows, liquid metal from the catalyst island is drawn up inside the core by capillary forces which lead to elongation[14] of the particle (Figure 6-21, left inset). These metal particles within the CNT core can induce kinking.[20] The kinking or bending of the tubes can then lead to the splitting of the catalyst particle causing a portion of catalyst to be left lodged at the kink point.[14]

6.5.4 From kink to junction

Junction-structures branch out from kink points via two concurrent and related mechanisms:

Junction formation mechanism 1

The bonding of carbon at kink points is similar to that of fullerene type nanotube caps, and hence not as strong as bonding in the body of the CNT. As can be seen from Figure 6-22 the split catalyst particles at kink points can seed points for further growth. It is believed that these split particles then form the tip of the branch tube[24, 1, 2, 21, 22] and in the case of purely tip-growth mechanism are carried away leaving the junction free of catalyst metal (Figure 6-23).

Junction formation mechanism 2

The second mechanism for junction formation is through the creation of multiple cores[25] similar to that put forward by Hou et al. In this case the split particle affects only one side of the MWNT creating heptagons in the outer shells causing them to branch off and create a second inner core so that two hollow cores sit side by side separated by several grapheme sheets (Figure 6-24).
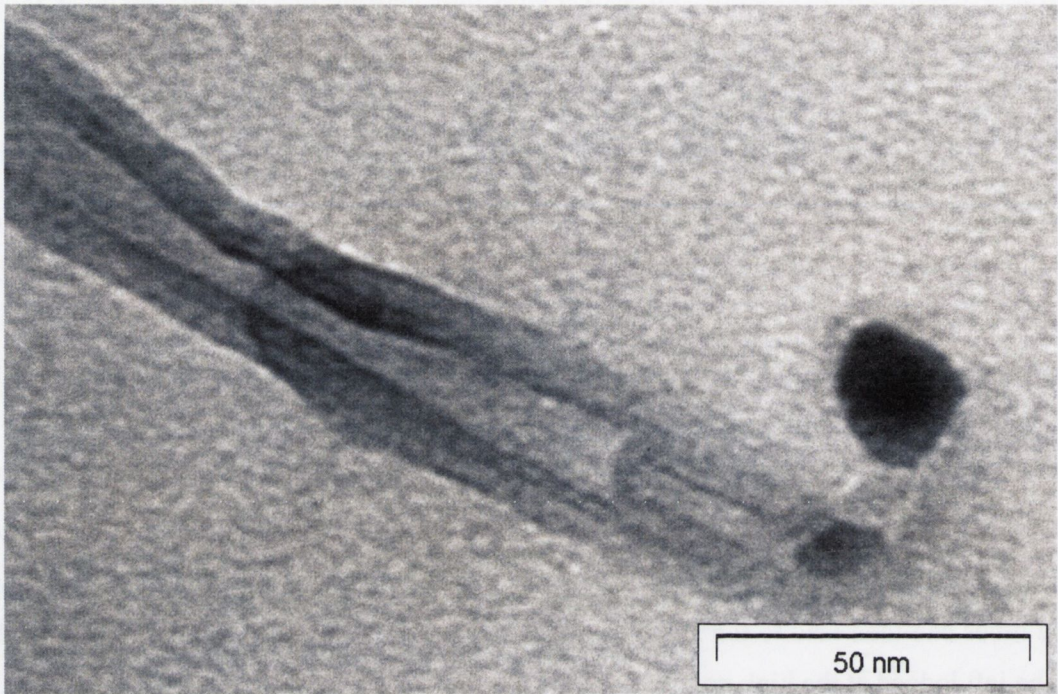
Figure 6-22 TEM micrograph showing metal particle caught at the kink point on a bent tube. This tube was grown under the following the conditions: Temp= 700°C, Ar flow= 1000 sccm, C_2H_2 flow = 0.3 sccm, time= 60 minutes.

6.5.5 Termination of growth

Termination of the growth of an individual bridging CNT or CNT branch occurs when it makes contact with opposite wall of the trench, or indeed the trench floor in the case of very wide trenches (Figure 6-8). When the tube tip makes contact with substrate the van der Waals interaction between the tube and substrate surface give rise to frictional forces. These forces are enough to overcome both the slow growth rate of the tube itself and the lifting force of the low flow of gas through the furnace tube.[15] It is likely that once CNT growth stops exposed catalyst particles are rendered inactive by catalyst poisoning due to a lack of a reducing agent in the system.[5] In other words the catalyst particle becomes oversaturated with carbon that cannot be expelled into the protruding CNT causing further incident carbon atoms to form an amorphous coating around the particle.
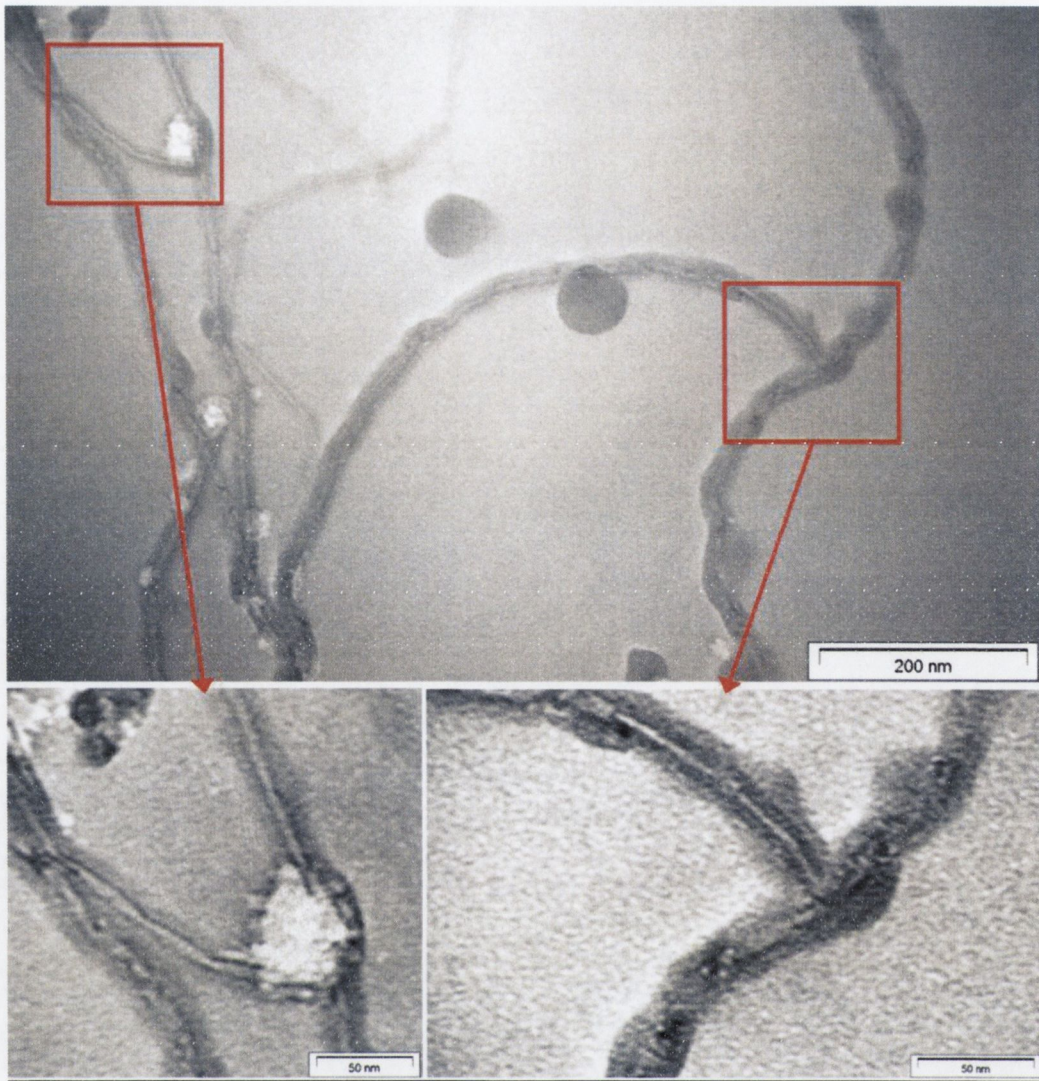
Figure 6-23 TEM micrograph showing two separate junctions. The tubes were grown under the following the conditions: Temp= 700°C, Ar flow= 1000 sccm, C_2H_2 flow = 0.3 sccm, time= 46 minutes. CNTs were grown on plain Si substrate and removed by sonication for analysis.
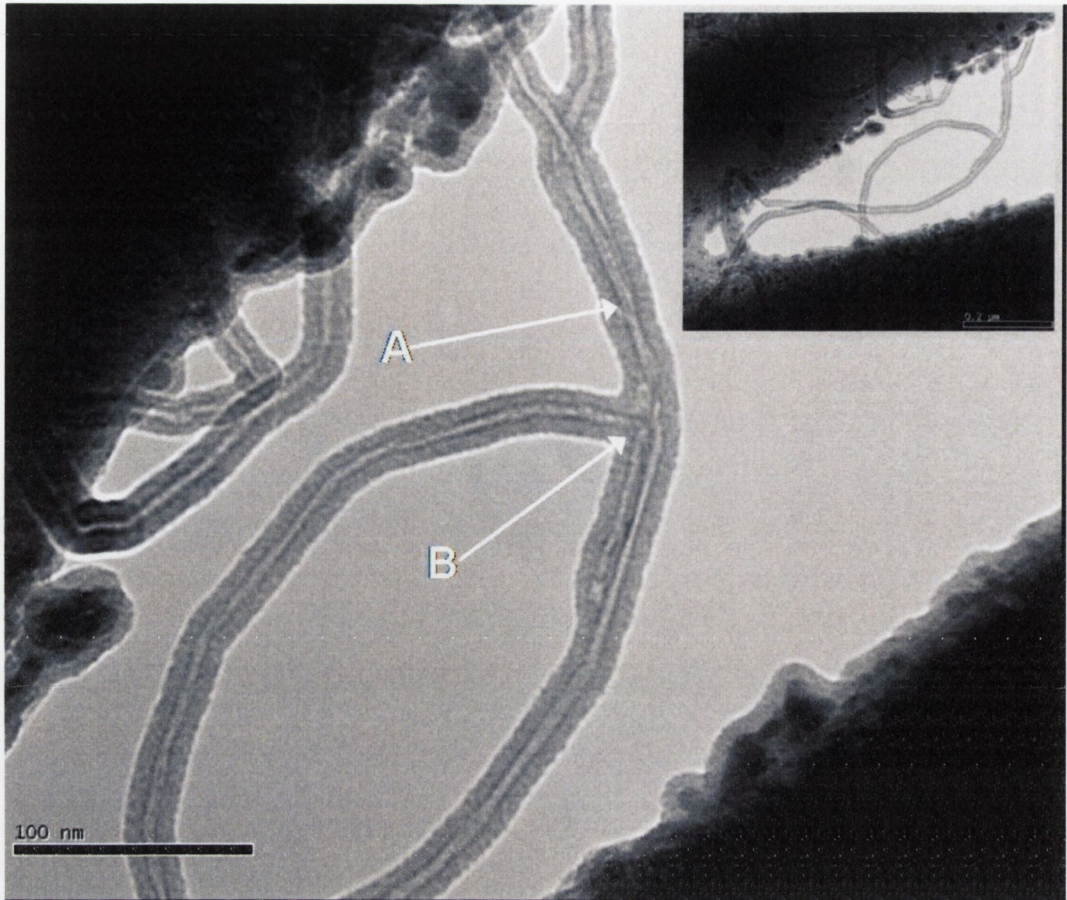
Figure 6-24 TEM micrograph showing A) a direct junction in a single nanotube arising from junction formation mechanism 1, and B) a multiple-core junction formed by mechanism 2. The CNTs are grown in-situ on a SiN membrane with trenches etched by FIB. Growth conditions were: Temp= 700°C, Ar flow= 500 sccm, C_2H_2 flow = 50 sccm, time= 68 minutes.

6.6 Raman spectroscopy

A Raman spectroscopy study was carried out on the samples after CVD. This showed that samples containing high proportions of junction-structure CNTs displayed a significantly larger D-band than samples containing a lower proportion of junction-structures. This again suggests that junction-structure CNTs tend to occur when there is a high degree of defects present in the tubes.

The slight up-shift in the position of the G-band for the samples containing junction-structures suggests also that these CNTs are less well graphitised; meaning that their outer shell can tend to be more amorphous in nature (Figure 6-25).
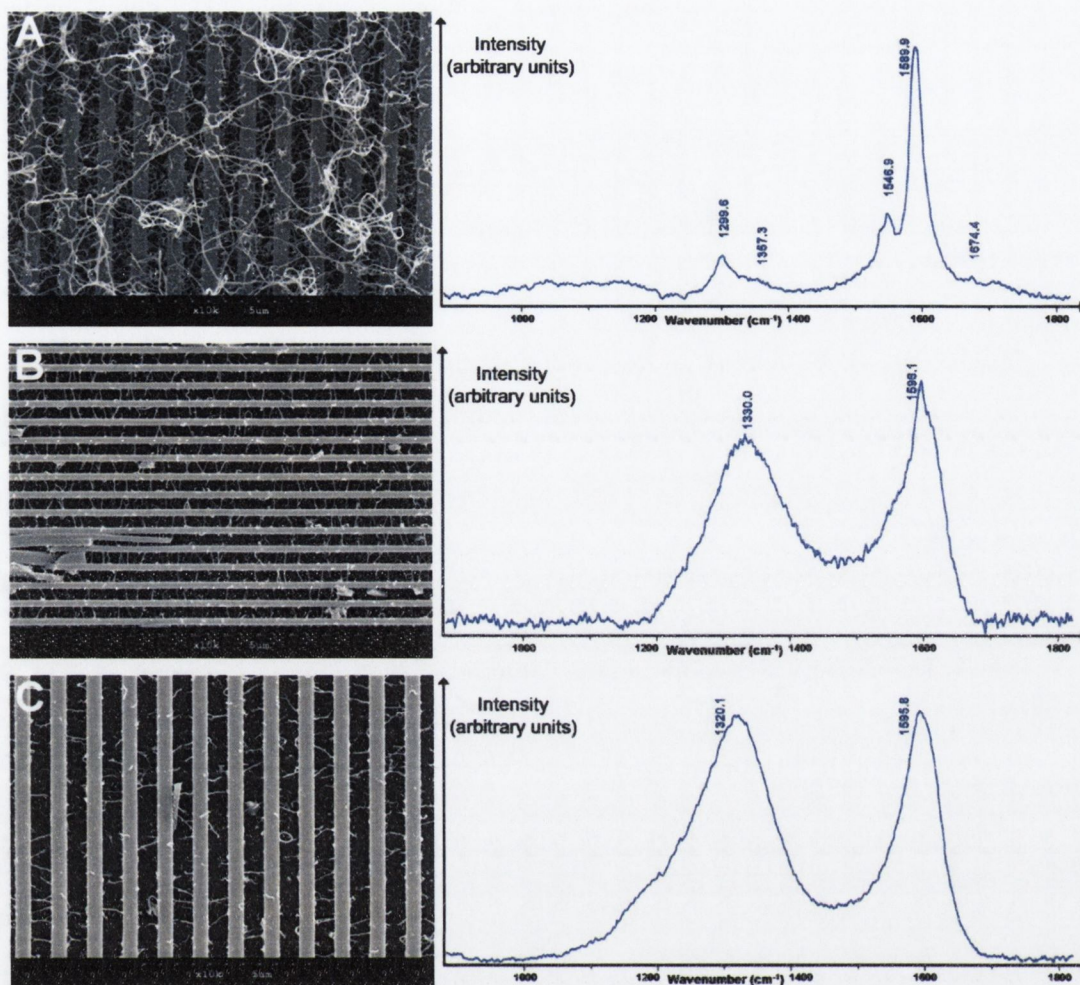
Figure 6-25 SEM micrographs with corresponding Raman spectra for A) heavy growth of CNTs with few junctions, B) an array of bridging CNTs with an intermediate proportion of junction-structure tubes, and C) an array of bridging CNTs with a high proportion of junction-structure tubes.

6.7 Conclusions

This chapter has presented a novel and simple method of catalyst self-alignment. This mechanism can be used to encourage the growth of bridging MWNTs between raised structures of various geometries.

A systematic study on the effects of CVD growth conditions resulted in the production of dense arrays of bridging nanotubes with 38% branched structures.

Growth mechanisms were suggested for the formation of the two forms of junction.

6.8 References

[1]   J.-M. Ting, T.-P. Li, and C.-C. Chang, Carbon **42**, 2997–3002 (2004).

[2]   J. M. Ting and C. C. Chang, Applied Physics Letters **80**, 324 (2002).

[3]   A. M. Cassell, N. R. Franklin, T. W. Tombler, et al., Journal of the American Chemical Society **121**, 7975 (1999).

[4]   L. P. Biro, Z. E. Horvath, G. I. Mark, et al., Diamond and Related Materials **13**, 241 (2004).

[5]   K. Hata, D. N. Futaba, K. Mizuno, et al., Science **306**, 1362 (2004).

[6]   L. Valentini, I. Armentano, J. M. Kenny, et al., Materials Letters **In Press, Corrected Proof**.

[7]   Y. H. Mo, A. K. M. F. Kibria, and K. S. Nahm, Synthetic Metals **122**, 443 (2001).

[8]   Y. C. Choi, D. W. Kim, T. J. Lee, et al., Synthetic Metals **117**, 81 (2001).

[9]   H. Ago, J. Qi, K. Tsukagoshi, et al., Journal of Electroanalytical Chemistry **In Press, Corrected Proof**.

[10]   S. K. Doorn, L. X. Zheng, M. J. O'Connell, et al., Journal of Physical Chemistry B **109**, 3751 (2005).

[11]   P. L. Chen, J. K. Chang, C. T. Kuo, et al., Diamond and Related Materials **13**, 1949 (2004).

[12]   M.-K. Li, M. Lu, L.-B. Kong, et al., Materials Science and Engineering A **354**, 92 (2003).

[13]   S. Fan, W. Liang, H. Dang, et al., Physica E: Low-dimensional Systems and Nanostructures **8**, 179 (2000).

[14]   C. H. Lin, H. L. Chang, M. H. Tsai, et al., Diamond and Related Materials **11**, 922 (2002).

[15]   S. M. Huang, M. Woodson, R. Smalley, et al., Nano Letters **4**, 1025 (2004).

[16]   B. H. Hong, J. Y. Lee, T. Beetz, et al., Journal of the American Chemical Society **127**, 15336 (2005).

[17]   S. M. Huang, B. Maynor, X. Y. Cai, et al., Advanced Materials **15**, 1651 (2003).

[18]   L. M. Huang, X. D. Cui, B. White, et al., Journal of Physical Chemistry B **108**, 16451 (2004).

[19]   S. Iijima, T. Ichihashi, and Y. Ando, Nature **356**, 776 (1992).

[20]   L. M. Dell'Acqua-Bellavitis, J. D. Ballard, R. Vajtai, et al., in *MRS*, edited by C.-J. Zhong, N. A. Kotov, W. Daniell and F. P. Zamborini (MRS, Boston, 2005), Vol. 900E, p. 0900.

[21]   F. L. DEEPAK, A. GOVINDARAJ, and C. N. R. RAO, journal of chemical science **118**, 9 (2006).

[22]   H. W. Zhu, L. J. Ci, C. L. Xu, et al., Diamond and Related Materials **11**, 1349 (2002).

[23]   N. Franklin and H. J. Dai, Advanced Materials **12**, 890 (2000).

[24]   S. Huang, L. Dai, and A. Mau, Physica B, 336–338 (2002).

[25]   P.-X. Hou, S. Bai, C. Liu, et al., Carbon **41**, 2477–2480 (2003).

[26]   B. Gan, J. Ahn, Q. Zhang, et al., Chemical Physics Letters, 23 (2001).

Chapter 7 Electrical measurements of individual CNTs

7.1 Introduction

In order to facilitate the integration of CNTs into current CMOS technologies their electrical properties must be fully understood.[1-4] Electrical testing of individual CNT devices is an important first step towards the creation of CNT circuits.[5]

In this chapter characterisation of the electrical properties of both straight and junction-structure CNTs is presented. Section 7.2 covers attempts to characterise straight CNTs via a focused ion-beam (FIB) deposited four-point probe technique. Section 7.3 outlines the strategies used and results obtained from in situ FIB deposited four-point probe characterisation of Y-junction CNTs. Section 7.4 presents results from atomic force microscopy (AFM) and conducting-probe AFM (CP-AFM) of junction-structures. The results of two- and four-probe measurements on two individual junction-structure CNTs are presented in section 7.5.

7.2 Probe deposition on individual, straight CNTs

Several attempts were made to deposit Pt contacts by focused ion beam (FIB) on individual, straight, multiwalled carbon nanotubes (MWNTs). The objective was to allow correlation of changes in resistance with desorption of gases from the MWNT surface during heating in vacuum (see Appendix A).

MWNTs were produced by CVD; suspended in isopropyl alcohol then dropped via needle tip into the centre of a silicon substrate with pre-deposited gold pads. Selected tubes were connected to the gold pads through FIB deposited Pt lines (Figure 7-1).
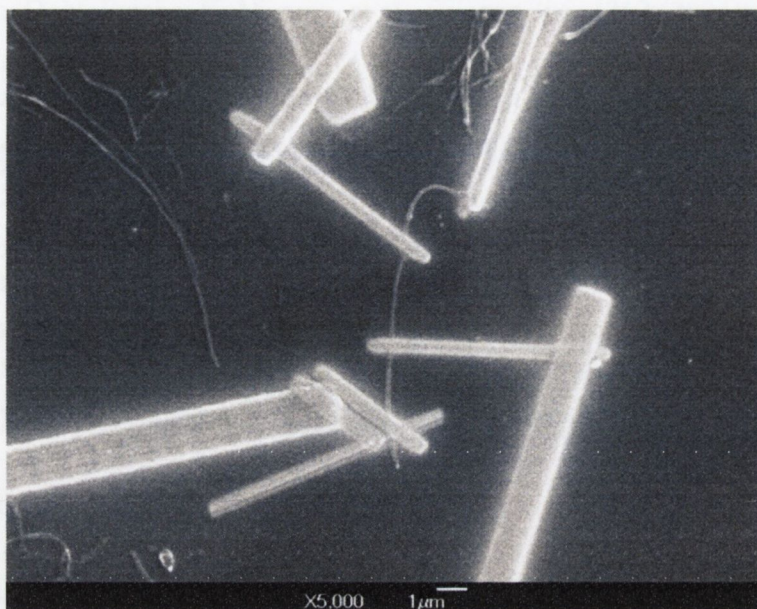
Figure 7-1 SEM micrograph showing an individual MWNT connected with four separate Pt connections.
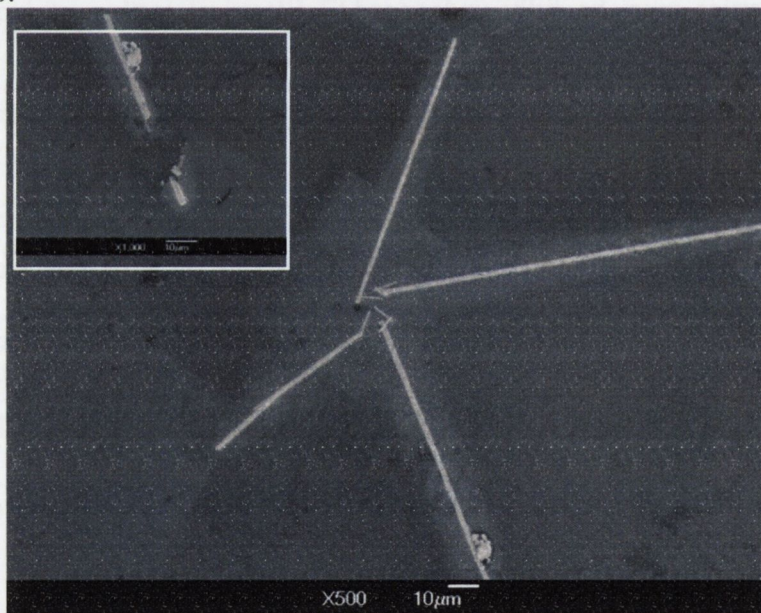
Figure 7-2 SEM micrograph showing a lower magnification of Figure 7-1. A halo of Pt and Ga⁺ ions deposited alongside the Pt connects (thinner brighter lines) which can cause shorting in any electrical measurement. The inset shows a mechanical break in a Pt connections caused by handling.

However, no functioning devices were achieved due to "spread" in the Pt contact lines and saturation of Ga^+ ions implanted by ion-beam during imaging with the ion beam (Figure 7-2). This leakage, visible above as a bright halo around the contacts, creates a

short circuit between the probes. All connections were made with the ion beam, and several attempts were needed to attach the CNT to the intermediate Pt lines. This resulted in the exposure of both CNT and surrounding area to the ion beam. Mechanical failure of the Pt contacts caused failure in several devices (Figure 7-2, inset) as larger Pt contacts connected directly to the pre-deposited gold pads tended to very fragile.

7.3 Electrical characterisation of MWNT Y-junctions

Several authors have reported electrical measurements on Y-junction MWNTs. The majority reporting rectifying behaviour.[6-11] Attempts were made to electrically test individual branched MWNT devices (Figure 7-3). The focus of these experiments was the measurement of as-grown MWNT junctions on trench-etched substrates. With such experiments it was hoped to discover the possible applications of such devices in interconnect applications. MWNT arrays were grown under a range of conditions on substrates containing both trench-etched areas and plain regions. For these samples greater care was taken not to over expose the targeted MWNT to Ga^+ ions from the ion-beam.

Junction-structures to be connected were never imaged with the ion beam itself. Instead, the electron and ion beams were aligned on a region of the surface far from the selected junction. The target area was imaged solely with the e-beam to minimise damage to the MWNT. Initial contacts to the MWNT itself were deposited using the e-beam. The lines were $1 - 3$ μm in length. These initial connections were subsequently extended using the ion-beam (with a beam current of 100 pA). In all cases it was ensured that the target junction was outside of the imaged field and that only the initial contacts remained inside the field. The surface was only imaged using the electron beam due to the alignment of the electron- and ion-beams. The only exposure the surface gets to the ion beam is during deposition of the Pt lines and pads. The larger lines and pads were deposited with ion beam currents up to 500 pA.

Electrical testing via four-point probe (4-PP) proved unsuccessful. All attempts showed an open circuit and subsequent SEM examination revealed that the MWNT had been destroyed. This was most likely the result of either the initial power surge during measurement or static discharge during handling.
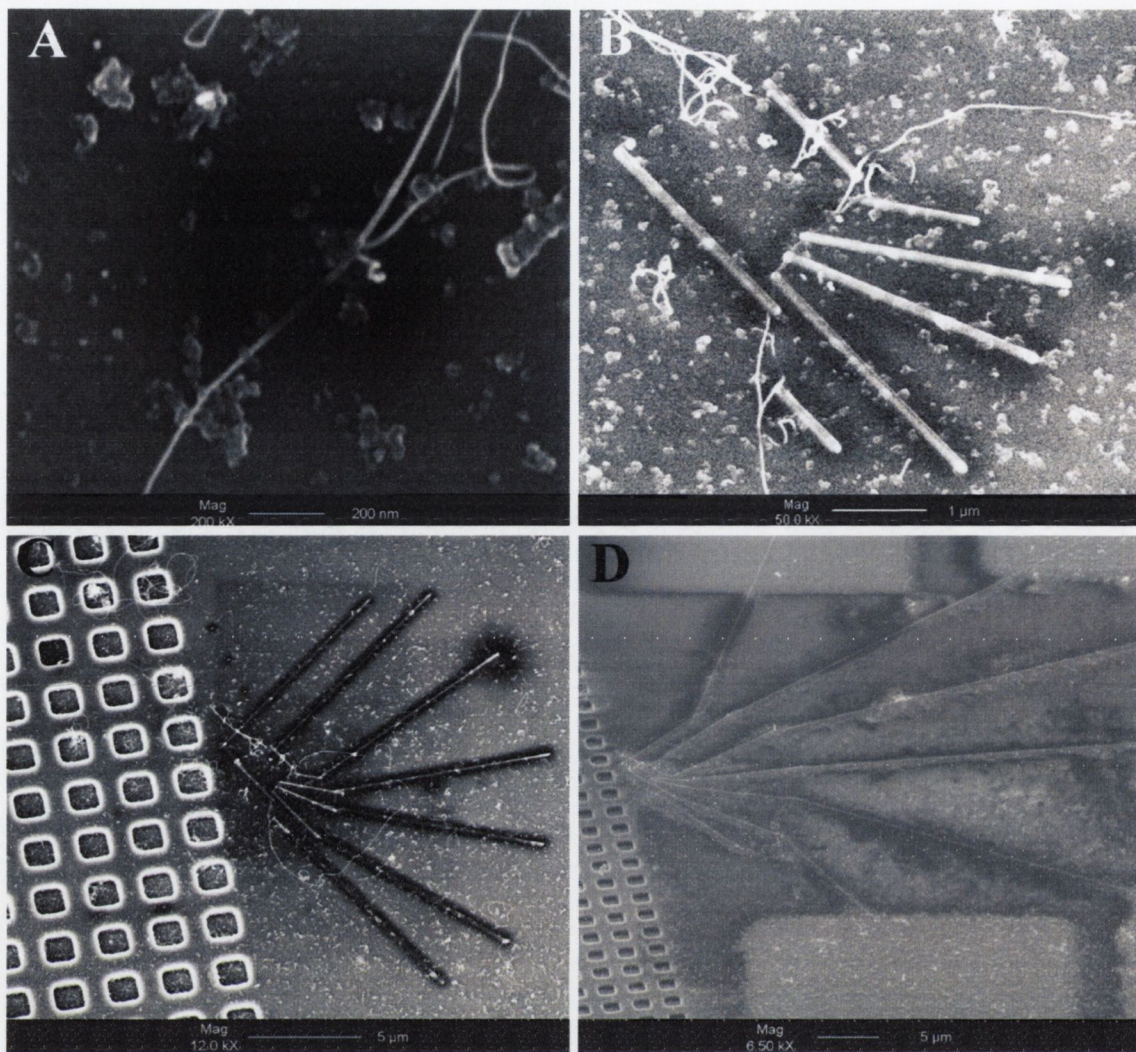
Figure 7-3 SEM micrographs showing A) a single Y-junction CNT lying on a plain Si surface, B) initial Pt lines deposited contacts deposited using the e-beam, C) intermediate Pt lines deposited by focused ion beam (FIB), and D) larger Pt lines and Pt contact pads deposited by FIB.

After several attempts a successful two-probe measurement was made on the stem of a single MWNT Y-junction. The I-V plot reveals Ohmic behaviour, with a resistance of 6.0 ± 0.6 MΩ. This value is very high compared to theoretical and experimental values measured for individual SWNTs[12] and MWNTs.[13] Resistances in the region of $100 - 400$ kΩ have been reported for individual MWNTs.[14] The discrepancy for this resistance measurement is most likely due to contact resistance between the MWNT and the deposited contacts.

The CNTs produced under the CVD conditions used in this thesis are expected to present Ohmic behaviour. The only gases present during the formation of the MWNTs are the Ar and C_2H_2, neither of which would be expected supply atoms such as N that could result in doped, semiconducting nanotubes.

Attempts to electrically measure junction-structures grown over trenches were difficult to achieve due to the small size of the trenches. Connecting these structures was difficult due their positioning on the very edge of the trench walls. On several occasions the deposited Pt lines bled into the trenches (which are in the region of 100 – 500 nm in width) covering the junction region or completely crossing the trench causing a short circuit.

Attempts were made using atomic force microscopy (AFM) and conducting-probe AFM (CP-AFM) to further characterise junction-structures grown across trenches. In both in tapping- and contact-modes the suspended nanotubes proved too flexible to allow for an accurate measurement.

7.4 Conducting-probe AFM measurements of junction structures

In order to get more accurate measurements CNTs were removed from the original trench-etched substrates and placed in suspension. N-methyl-2-pyrrolidone (NMP) was chosen as it has been shown to be an excellent solvent for the dispersion of CNTs.[15, 16] Several samples were prepared on Intel test-chips, as they have a high density of etched trenches of a wide variety of widths. These samples were submerged in ~ 1 ml NMP and gently agitated for several minutes taking care not to damage the fragile junctions while removing them from the surface. The NMP-CNT suspension was drop cast onto the centre of a substrate with pre-patterned gold contacts and dried in an oven at 60°C for several hours.

AFM imaging was carried out on a Dimension DI3100 utilising a hybrid scanner with a nanoscope 4A controller. CP-AFM was carried out using a degenerately-doped silicon cantilever tip. A small section of the oxide layer at the back of the cantilever etched away with a diamond scribe. An electrical connection was made using silver paste. The central region of the gold electrode pattern was searched. Scans were taken close to the gold electrodes where a good path exists through the CNTs under investigation.

A number of Y-junction CNTs were observed on the surface of the substrate close to the gold electrodes (Figure 7-4). The Y-junction MWNTs highlighted are approximately 335 nm and 950 nm in length, measured along the line of the stem (Figure 7-5), which corresponds well with trench widths on growth substrates. The branches of each tube are of similar diameter and show similar conductivity with currents of ~200 pA passing through each. This suggests that the junction-structures do not behave as transistors, rather as simple Ohmic conductors.
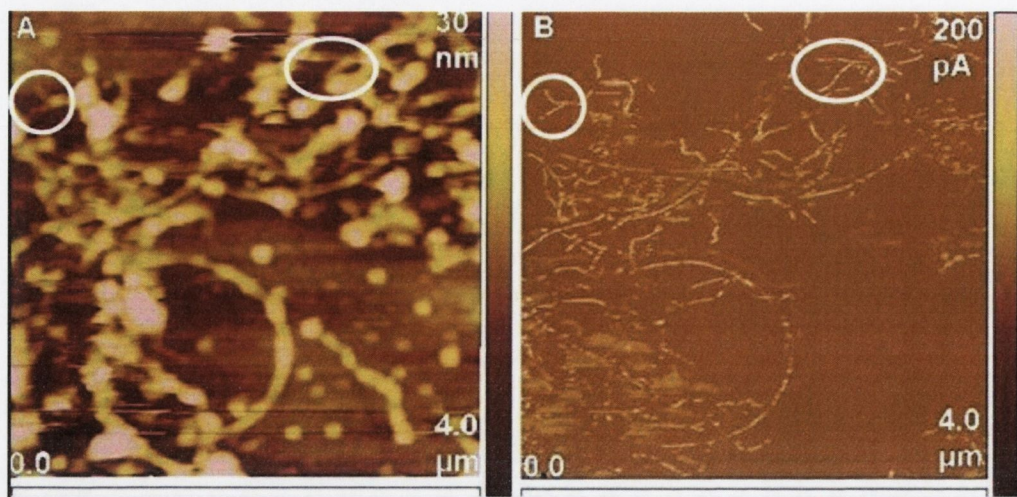
Figure 7-4 Set of micrographs showing an array of CNTs including two Y-junctions (highlighted) imaged in A) AFM and B) CP-AFM.
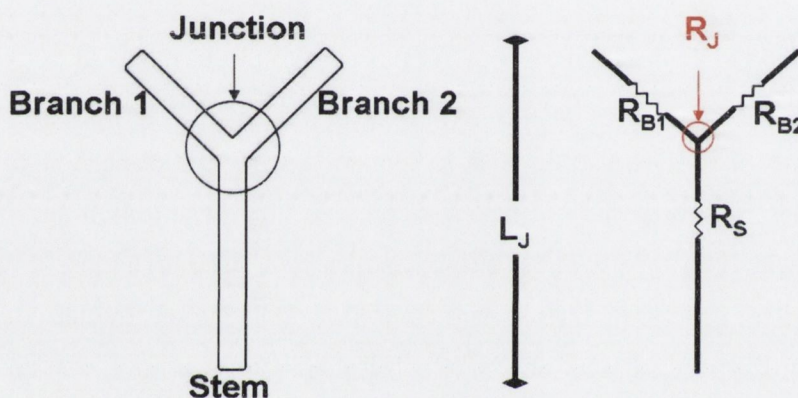
Figure 7-5 Schematic of Y-junction CNT "anatomy" showing (left) the stem, branches and junction itself, and (right) the simplified model of a MWNT Y-junction in a series of resistors.

7.5 4-PP measurements of Y-junctions

To avoid the problems of FIB deposited contacts (Section 7.3). Electrical contacts were deposited onto several isolated Y-junctions using metal-evaporation combined with electron beam lithography (Figure 7-6). This was carried out with a Carl Zeiss Evo electron column utilising a Raith Lithography system.

Drop cast samples were prepared as in section 7.4. The central region of the patterned substrate was imaged with the SEM beam. Large Y-junction CNTs were selected with branches several hundred nanometers long. Individual "beam-blank" patterns were designed for each chosen structure to allow for lithography and evaporation of conducting metal lines from the junction-structure to the conducting pads on the substrate. Samples were removed from the SEM chamber and spin-coated with a layer of photo-resist

(PMMA) for 40 seconds at 3000 rpm and baked at 200°C for two minutes. This processes results in a ~120 nm resist layer on the substrate. These samples were reintroduced to the SEM chamber and realigned so that the beam-blank pattern exposed the desired regions of resist to 15KeV electron-beam. The samples were once more removed from the SEM chamber, and the remaining resist developed. A sticking layer of 5 nm of Ti followed by a 35 nm layer of Au was evaporated onto the sample surface. The remaining photo-resist, and with it unwanted gold was removed by placing the sample in boiling acetone for several minutes.
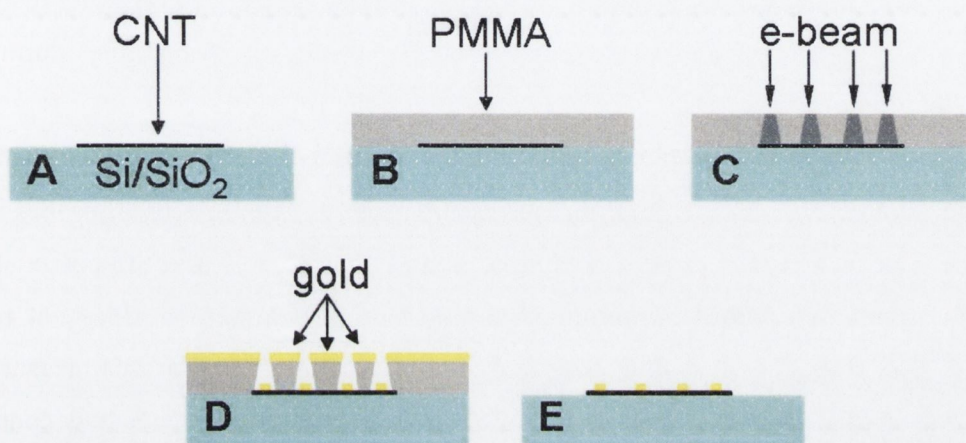
Figure 7-6 Schematic showing the fabrication of a contact array on an individual MWNT: A) an MWNT structure is located in an appropriate region of the substrate, and a beam-block pattern designed in the lithography software. B) A layer of resist is spin-cast over the sample surface. C) The resist is exposed to the e-beam as specified by the beam-block pattern. D) The metal contact layer is evaporated on the resist covered surface. E) Finally, the resist is removed leaving only metal contacts in the desired location.

Samples were then mounted on a microprobe station so that the gold pads could be individually connected to a circuit via microprobe pins. Two- and four-probe resistance measurements were made, with the current between the probes being swept from 0.1 to -0.1 nA.

Using such low levels of current can lead to some slight inaccuracies, however current size must be balanced with the delicate nature of the CNT devices. Samples were first examined using very low, "safe" currents before being tested to destruction with higher currents.

Two CNT Y-junction devices were fabricated in this manner. The first of these is represented in the SEM micrographs shown in Figure 7-7. The stem of the Y is approximately 6 μm long, with the left and right branches being 680 ± 10 nm and 1160 ± 30 nm in length respectively.

Five connections were deposited on the stem on the CNT. Of these, four connections (Figure 7-7, connections 3-6) made successful electrical contact with the CNT. Two-probe measurements were made for each combination of contacts (3-4, 3-5, 3-6…). Resistance were found to be >800 KΩ. Resistance with respect to probe separation was noted, and extrapolated back to zero probe-separation. From this the contact resistance was found to be ~100 - 200 kΩ. When the contact resistance is subtracted, the resistance of the stem is found to be between 100 – 800 kΩ. Contact resistivities of this magnitude are expected, and are in line with contact resistances measured for similar un-annealed contact systems.[19-21] It should be noted that Pd has been shown to have a lower contact resistance to CNTs[17,18]. Ti/Au contacts were chosen purely based on availability during the experimental timeframe.

These two-probe resistance values are in agreement with a 4-PP measurement along the stem of 240 ± 4 kΩ. 4-PP measurements consist of four electrical probes in line along the CNT. Current is passed though the outer two probes, while the potential drop across the inner two probes is monitored. Voltage drop measurement does not require current to be drawn, thus negating the effect of contact resistance. For this measurement current was applied between contacts 3 and 6, while the potential drop across contacts 4 and 5 was measured. Several other sources in literature report similar values for room temperature resistance measurements,[19, 22-25] however others report values several orders of magnitude ranging from ~10 kΩ[26, 27] and lower[21] with resistances of individual MWNTs of a few hundred Ohms.[20] Resistivities obtained from the 4-PP measurements are in the range 5 – 10 x 10^{-3} Ωcm, which is similarly several orders of magnitude higher than the lowest quoted values for individual straight nanotubes of ranging from 10^{-4} – 10^{-6} Ωcm.[28-30] These discrepancies are most lightly due to high contact resistances, and the inherent errors associated with using very low currents.

A second set of two-probe measurements were made across the across the junction from the stem to the right branch (3-8, 3-9, 4-8…). Resistance was plotted against probe-separation, and the resistance at zero separation was extrapolated to be 800 ± 300 MΩ. This can be taken to be the resistance of the junction plus the contact resistance. However, given the relative difference between it and value obtained for contact resistance, this value can be essentially taken to be the resistance of the junction itself. 4-PP measurements across the junction also yield resistance values of between 800 – 1000 MΩ.

To investigate the electrical function of the junction, the branches were shorted together (through contacts 8 and 12) and a set of two-probe I-V measurements taken across the junction (Figure 7-8).
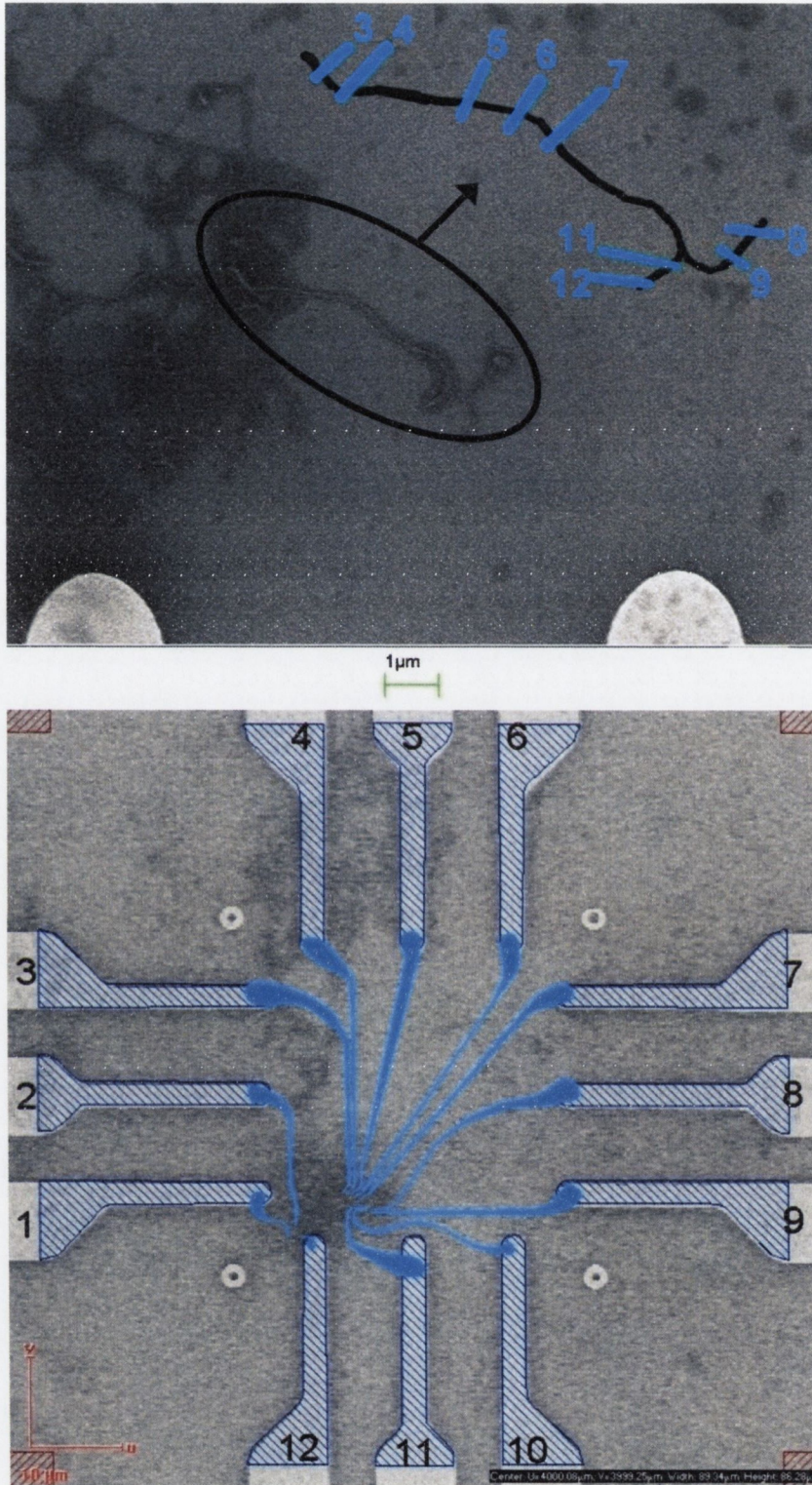
Figure 7-7 SEM micrographs showing the actual Y-junction with schematic showing metal contact locations (top) with an overlay of the lithography mask designed to allow the deposition of the actual metal contacts onto the CNT.

Rectifying behaviour of CNT Y-junctions has been reported elsewhere in the literature[6-9, 14]. However, in this case both stem and branches are MWNTs and hence it is

likely that all three are metallic. Added to this the majority of junction-structures observed tend to have both stem and branches of the same diameter. The curvature in the I-V plot most likely arises from hopping or scattering effects at the junction due to graphitic lattice mismatching. Similar I-V plots are seen in the literature at kink points resulting from pentagon-heptagon pairs introduced to the graphitic matrix.[31-33] Direct junctions between two different metallic CNTs can impede the flow of electrons,[34, 35] and have been described as displaying backscattering at the junction due to strong σ-π mixing.[36]
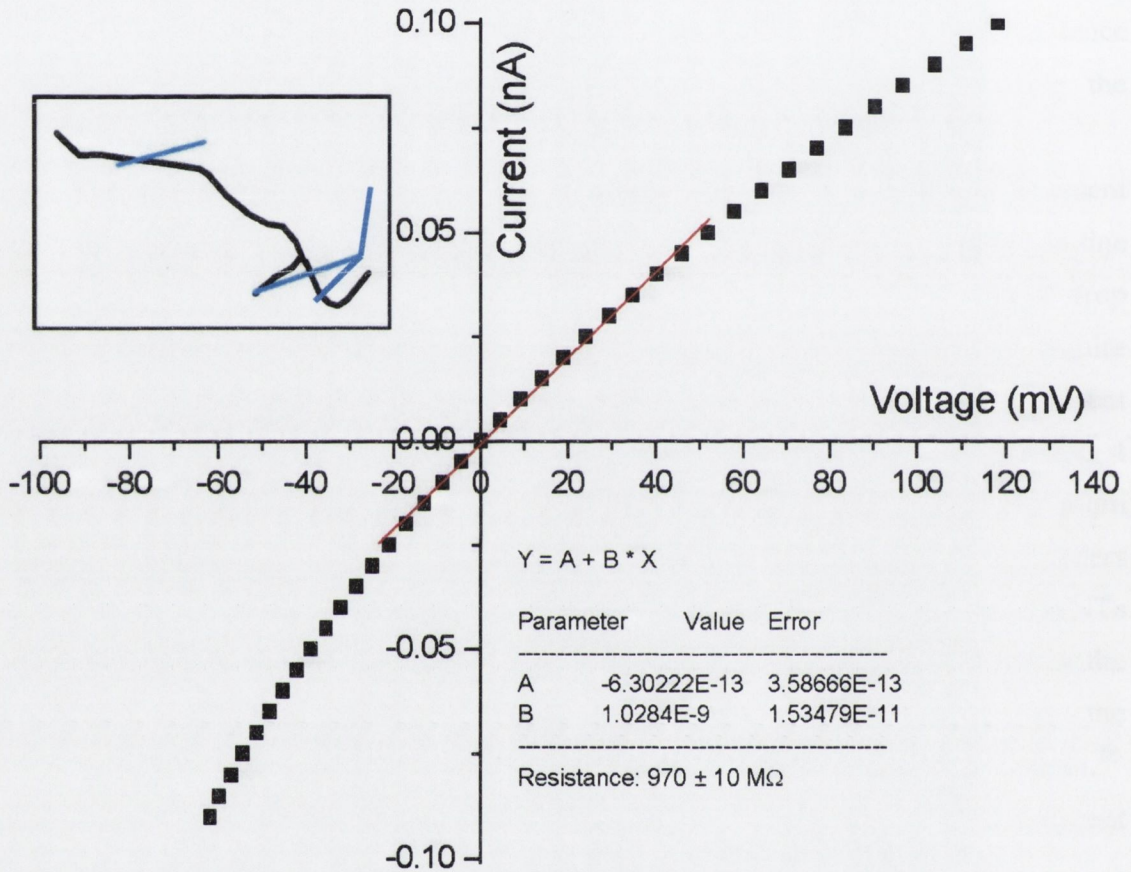
Figure 7-8 I-V curve of a two-probe measurement across the junction with the two branches shorted together. The schematic (top right) shows the position of the two electrical contacts: one on the stem, and the second contacted to both branches.

A second junction-structure was isolated on a separate substrate (Figure 7-9). The top branch, which lies over one of the pre-patterned contacts, is 2 μm long. The bottom branch was measured at 3.8 μm in length, and the stem at 620 nm.
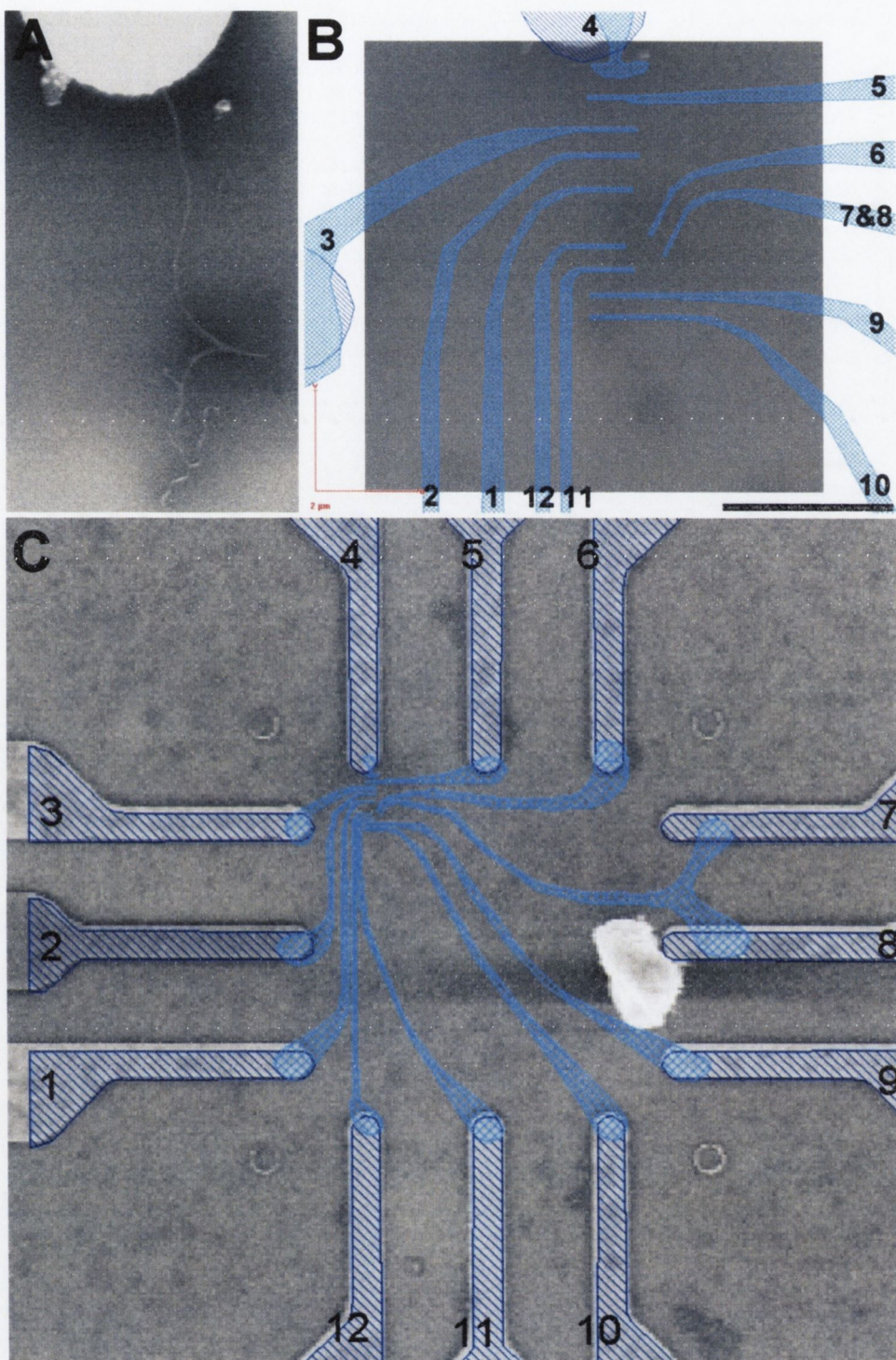
Figure 7-9 SEM micrographs showing A) the actual CNT Y-junction to be connected and B) & C) an overlay of the template allowing the deposition of Ti and Au lines to connect the CNT to the pre-patterned pads on the substrate (visible in C).

After the connections were made 4-PP measurements were made across the junction (Figure 7-10). Resistance values across the junction were measured as 158, 188, and 39 MΩ, in the directions of: 4 & 8, 4 & 10, and 7 & 10 respectively. The junction-

structure is again seen to exhibit Ohmic as opposed to rectifying behaviour. The high resistances are possibly due a junction structure such as that in Figure 6.24 B. This formation consists of the creation of a second core separated by several graphitic layers. The Raman analyses of similar MWNTs (Section 6.6) points to an amorphous carbon outer coating. This leads to an amorphous layer separating the two cores. Such an insulating layer of amorphous carbon separating the conducting well-graphitised walls of the two cores would set up a tunnelling barrier at the junction. Similar results are seen for interlayer conduction within individual MWNTs,[37, 38] junctions formed by frayed SWNT bundles[39] and crossed CNTs.[40, 41]
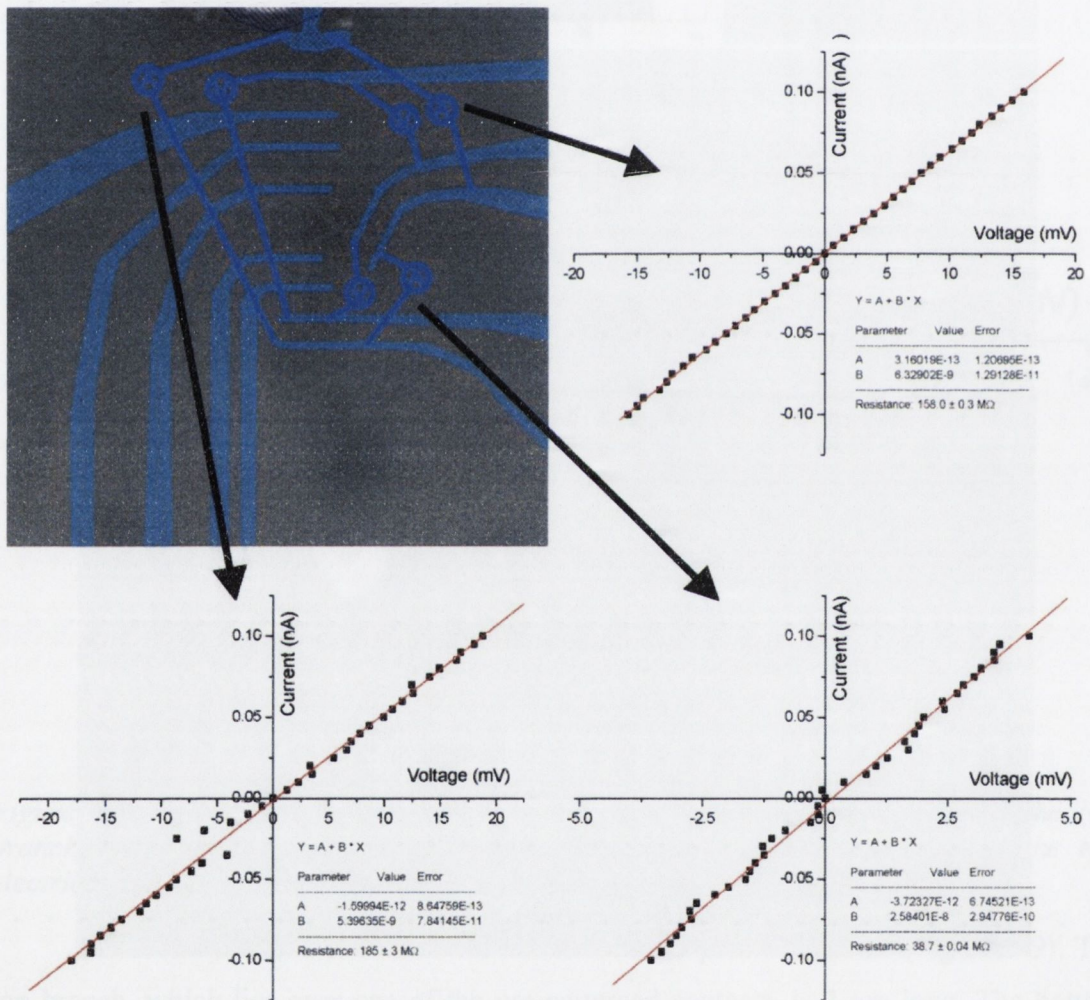
Figure 7-10 A selection of I-V plots representing the results of 4-PP resistance measurements across the join point in the Y-junction presented in Figure 7-9.

7.6 Conclusions

CP-AFM measurements on Y-junction CNTs display conduction paths through both stem and branches. Attempts made to deposit Pt co[21]nnections using FIB proved unsuccessful.

Successful depositions of gold wires (with a Ti sticking layer) to connect individual Y-junction CNTs to the conduction pads was achieved via e-beam lithography. Two devices were successfully fabricated and characterised by this method. Both devices display purely ohmic behaviour.

This ohmic behaviour combined with successful growth of aligned arrays of such devices opens up the possibility of their integration into a larger nano-electronic device as "interconnects" between nano-electronic logic devices.

7.7 References

[1]   M. Terrones, International Materials Reviews **49**, 325 (2004).

[2]   A. P. Graham, G. S. Duesberg, R. Seidel, et al., Diamond and Related Materials **13**, 1296 (2004).

[3]   P. G. Collins and P. Avouris, Scientific American **283**, 62 (2000).

[4]   H. Xu, Nature Materials **4**, 649 (2005).

[5]   Y. C. Tseng, P. Q. Xuan, A. Javey, et al., Nano Letters **4**, 123 (2004).

[6]   A. N. Andriotis, M. Menon, D. Srivastava, et al., Physics Review B **65**, 165416 (2002).

[7]   A. N. Andriotis, M. Menon, D. Srivastava, et al., Physical Review Letters **8706**, art. no. (2001).

[8]   A. N. Andriotis, M. Menon, D. Srivastava, et al., Applied Physics Letters **79**, 266 (2001).

[9]   C. Papadoupoulos, A. Rakitin, J. Li, et al., Physical Review Letters **85**, 3476 (2000).

[10]   B. C. Satishkumar, P. J. Thomas, A. Govindaraj, et al., Applied Physics Letters **77**, 2530 (2000).

[11]   J. Park, C. Daraio, S. Jin, et al., Applied Physics Letters **88**, 243113 (2006).

[12]   S. J. Tans, M. H. Devoret, H. J. Dai, et al., Nature **386**, 474 (1997).

[13]   L. Langer, V. Bayot, E. Grivei, et al., Physics Review Letters **76**, 479 (1996).

[14]   P. R. Bandaru, C. Daraio, S. Jin, et al., Nature Materials **4**, 663 (2005).

[15]   K. D. Ausman, R. Piner, O. Lourie, et al., J. Phys. Chem. B **104**, 8911 (2000).

[16]   S. Giordani, S. D. Bergin, V. Nicolosi, et al., Journal of Physical Chemistry B **110**, 15708 (2006).

[17]   Babic, *AIP conference proceedings*, 2004), Vol. 723, p. 574.

[18]   A. Javey, J. Guo, Q. Wang, et al., Nature **424**, 654 (2003).

[19]   M. Ahlskog, P. Hakonen, M. Paalanen, et al., Journal of Low Temperature Physics **124**, 335 (2001).

[20]   C. Schonenberger, A. Bachtold, C. Strunk, et al., Applied Physics a-Materials Science & Processing **69**, 283 (1999).

[21]   A. Bachtold, M. Henny, C. Terrier, et al., Applied Physics Letters **73**, 274 (1998).

[22]   A. Kanda, K. Tsukagoshi, S. Uryu, et al., Microelectronic Engineering **63**, 33 (2002).

[23]   P. G. Collins, A. Zettl, H. Bando, et al., Science **278**, 100 (1997).

[24]   J. E. Fischer, Physics Review B **55**, R4921 (1997).

[25]   A. Thess, Science **273**, 483 (1996).

[26]   T. Mihara, K. Miyamoto, M. Kida, et al., Superlattices and Microstructures **34**, 383 (2003).

[27]   T. Kanbara, T. Takenobu, T. Takahashi, et al., Applied Physics Letters **88**, 053118 (2006).

[28]   A. Bachtold, C. Strunk, J. P. Salvetat, et al., Nature **397**, 673 (1999).

[29]   H. Dai, E. W. Wong, and C. M. Lieber, Science **272**, 523 (1996).

[30]   T. W. Ebbesen, H. J. Lezec, H. Hiura, et al., Nature **382** (1996).

[31]   H. W. C. Postma, T. Teepen, Z. Yao, M. Grifoni, and C. Dekker, Science **293,** 76-79 (2001).

[32]   P. G. Collins, A. Zettl, H. Bando, A. Thess, and R. E. Smalley, Science **278,** 100-103 (1997).

[33]   Z. Yao, H. W. C. Postma, L. Balents, and C. Dekker, Nature **402,** 273 (1999).

[34]   L. Chico, L. X. Benedict, S. G. Louie, and M. L. Cohen, Physical Review B **54,** 2600 (1996).

[35]   M. S. Dresselhaus, G. Dresselhaus, and P. Avouris, *Carbon nanotubes* (Springer, Berlin, 2003).

[36]   A. Rochefort, P. Avouris, F. Lesage, and R. R. Salahub, Physical Review B **60,** 13824 (1999).

[37]   E. Watanabe, K. Tsukagoshi, D. Kanai, I. Yagi, and Y. Aoyagi, Applied Physics Letters **83,** 1429 (2003).

[38]   E. Watanabe, K. Tsukagoshi, I. Yagi, and Y. Aoyagi, Microelectronic Engineering **73-74,** 666-669 (2004).

[39]   D.-H. Kim, J. Huang, K. Bangalore, and W. Choi, Journal of Applied Physics **99,** 056106 (2006).

[40]   M. S. Fuhrer, J. Nygard, L. Shih, M. Forero, Y. G. Yoon, M. S. C. Mazzoni, H. J. Choi, J. Ihm, S. G. Louise, A. Zettl, and P. L. McEuen, Science **288,** 494-497 (2000).

[41]   J. W. Park, J. Kim, and K. H. Yoo, Journal of Applied Physics **93,** 4191-4193 (2003).

Chapter 8 Conclusions

8.1 Summary

A custom-built CVD system was designed and constructed specifically to grow CNTs on a small scale for research purposes. The system was intended to be space efficient, versatile, and robust. The carbon feedstock gas was chosen as acetylene which helps promote the growth of MWNTs, though any gaseous carbon feedstock can easily be used with this system.

Using this CVD system a variety of MWNT geometries have been produced including individual long tubes with lengths of up to 30 μm and aspect ratios of up to 1000. These long tubes were grown on a variety of substrates; the length was limited by the geometry of the gas inlet system which promotes chaotic flow within the furnace-tube.

CNT forests and mats were grown on silicon substrates. The iron catalyst was introduced onto the substrate either as an iron-containing bloc copolymer solution, or through evaporation of iron onto the surface. The highest quality CNT forests were grown on substrates that were pre-treated by evaporating 15 nm of iron through a simple mask fabricated from a sheet of aluminium foil designed to give islands of a variety of sizes.

An experiment was undertaken to grow CNTs in mesoporous silica. A study of the system with SEM, EDX and Raman spectroscopy showed that the MWNTs grew almost entirely on the surface. This surface growth resulted from the catalyst metal pooling on the surface during substrate heating.

An alternative catalyst delivery system based on an aqueous solution of $FeSO_4$ and PVP was studied. The crystalline nature of the $FeSO_4$ results in the amorphous skeletal

outline of the FeSO$_4$ crystals. In the centres of these outlines were "nests" of randomly orientated CNTs.

It has also been shown that the CVD system can be used as an annealing oven. FTIR shows that functionalised CNTs display significantly less functionalisation when annealed under argon at 500°C for 60 minutes.

MWNT Y-junctions were initially grown on the surface of porous alumina membranes. These branched structures were observed to span indents in the substrate surface or alternatively with each branch anchored to a raised particle.

Branched MWNT structures were grown on silicon substrates that had a variety of trench patterns etched into the surface. These structures have been fabricated over trench widths ranging from ~100 nm to several microns. Though Y-junctions were the predominant junction-structures formed, a number of multi-branched structures were recorded. Branch and bridging tubes have been grown on different levels, leading the way for 3-D alignment.

A systematic study was undertaken to ascertain the effect of the initial conditions on bridging MWNT array characteristics. The average CNT diameter was found to be between 20 – 35 nm and the average junction angle was found to be between 60 – 90°.

The study revealed that both the total number of bridging CNTs (both straight and branched CNTs) and proportion of branched CNTs increase with decreasing temperature. It was also noted that the total number of bridging CNTs increases with decreasing trench width while the proportion of branched tubes remains unchanged.

Neither flow rate nor catalyst solution concentration show any significant effect on array density or makeup within the parameters of the study. However, combining an increase in both these parameters to values beyond the scope of the study causes a dramatic change from arrays of bridging MWNTs to long randomly aligned MWNTs that do not bridge trenches edge to edge.

As a result of this systematic study the optimum initial conditions were chosen as: acetylene flow rate of 50 sccm mixed with argon flowing at 500 sccm at 700°C for 60 minutes. These conditions lead to a good quality array which has both a linear density of bridging CNT structures (~1.6 interconnects per μm of trench length) and a high proportion of branched interconnect CNT structures (~38%).

A combination of EDX, optical microscopy and contact angle analysis show that the catalyst material is pulled to the edges of the substrate area wetted by the solution. This leads to self-alignment of the catalyst (and consequently CNTs) along the edges of trenches.

CNTs in this system appear to grow via tip growth mechanism. The chaotic flow and low temperature of the CVD are conducive to the formation of kinks. It is from these kinks that junctions form.

The growth of the stem and its branches continues across the trench as long as it is unimpeded by surface interactions. Growth termination occurs when the tube tip makes contact with the opposing trench wall.

Raman spectroscopy shows an increase in the relative size of the D-band with respect to the G-band for increasing proportions of branched structures within an array. This reveals that the amount of sp^3 carbon bonding (such as that at kink and junction sites) within the system increases with increasing percentage of branched structures.

Two individual, isolated junctions were examined with two and four point probe conductance measurements. In-line resistances of the individual branches are in line with experimental values presented in literature. The resistances of the junctions themselves are seen to be several orders of magnitude higher, yet still demonstrate purely Ohmic responses.

8.2 Conclusions

Results presented in this study show that it is possible to grow arrays of straight and branched CNTs. It can be seen that these interconnecting tubes position themselves along the edges of trenches and show alignment based on trench geometry. The method described allows for the growth of ordered arrays of tubes grown at relatively low temperatures containing high percentages of branched CNT structures. Catalyst positioning employs an inherent self-alignment mechanism that is both simple and scalable in nature. The dimension and aspect ratios of these CNT structures are similar to those required for such silicon technologies as IC circuits. This control over the arrays in combination with the demonstrated metallic behaviour represents the possibility of integration into nano-electronic architectures.

In summary this thesis presents an entire process: from fabrication of a CNT production method, through optimisation of CNT arrays to characterisation of individual CNT devices.

Appendix A Gas desorption in single wall Carbon nanotube mats during vacuum annealing

A.1 Introduction

The following section is based on research carried out in 2000/2001.[1] Many applications of CNTs such as hydrogen storage for fuel cells, and chemical sensing, are sensitive to gas adsorption/desorption processes, which in turn depend on the type and distribution of adsorption sites (e.g., inter-tube channels, intra-tube pores). This is particularly so for carbon-nanotube-based chemical sensors[2-4] where residual gases present on the SWNT surface can impact the type, extent, and kinetics of the response. For instance, it has been shown that residual gases such as O_2, He and N_2 can cause dramatic changes in the thermoelectric power of SWNTs.[5] A detailed understanding of the gas adsorption/desorption mechanisms and kinetics at these sites is therefore essential.

Despite the above significance, only limited studies are available on the adsorption-desorption behaviour of SWNTs. For example, although the effects of adsorption of gases to the surface of carbon nanotubes in various forms have been studied both experimentally and theoretically,[3-7] a quantitative analysis of the gas desorption using mass spectroscopy is missing. More significantly, the variation of resistance with gas adsorption primarily aimed towards the elucidation of gas sensing mechanism, by Ichimura et. al. needs indirect confirmation.[8-10] Since their work focuses on desorption of various gases from C_{60} and multiwalled carbon nanotubes, it is important to verify these results for SWNTs using similar experimental methods.

Earlier studies have reported the changes in resistance of SWNTs during gas adsorption[4]. In this study the variation of electrical resistance of SWNT mats with temperature during gas desorption, and subsequent air exposure was examined. Oxygen atoms appear to desorb as CO_2 rather than O_2 at well-defined temperatures, indicating a chemical interaction between carbon and oxygen.

A.2 Experimental

Nanotube mats procured from Carbolex Inc, prepared from SWNTs produced by the arc-discharge method were used for these experiments. The as-received SWNT mats are ~95% pure, but contain some non-carbonaceous impurities including residual Ni and Y catalysts. These mats were cut into 5 mm x 10 mm sections to fit with probe geometry. The mats were mounted in a computer-interfaced ultra-high-vacuum tube furnace equipped with an SRS RGA200 mass spectrometer, and pressed onto an Al_2O_3 block by four spring-loaded Mo probes in the Van der Pauw geometry. Electrical resistance measurements and mass spectra were obtained at periodic intervals during controlled heating and cooling at 2 K min^{-1} from 295 to 873 K. The starting pressure at 295 K, prior to annealing, was ~ 10^{-8} Torr. The HOPG samples (grade SPI 3) used were obtained from SPI Supplies and tested in the same manner as the SWNT mats.

A.3 Results and discussion

SWNT mats exhibit irreversible resistance changes when heated from room temperature to 873 K, as shown in Figure A-1. Curve A shows resistance (R) vs. temperature (T) characteristics of mat during the first heating and cooling cycle. Mat-resistance remains at 1 Ω (room temperature) up to ~333 K. Above this temperature, R increases rapidly at the rate of ~0.2 $m\Omega K^{-1}$, and reaches a maximum of 1.027 Ω at a temperature of ~473 K. Further increases in temperature, up to 875 K, result in a resistance decrease with two distinct steps at ~563, and 663 K respectively. Cooling to the room temperature at the same rate results in a sigmoidal R-T curve that is essentially reversible upon reheating, and invariant with repeated number of heating and cooling cycles, provided UHV is maintained (curve B).

In contrast, the R-T characteristics obtained from samples exposed to ambient atmosphere for several hours (after cycles A and B) have an intermediate resistance curve

that depends on the exposure time. Curve C is an example of the R-T characteristics observed after 9 hours exposure to atmosphere.
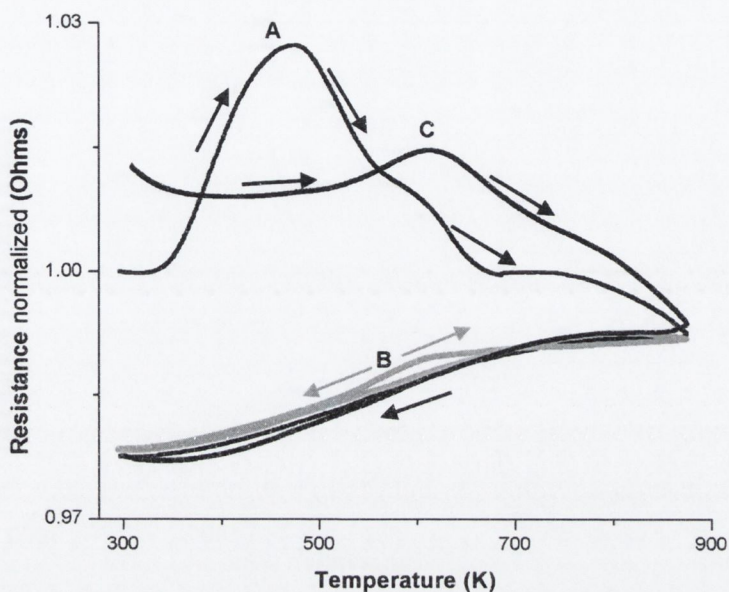

Figure A-1 Temperature dependence of resistance of the SWNT mat during heating to 873 K and cooling in UHV for A) annealing after exposure to atmosphere for a long time, B) annealing immediately after run A without breaking vacuum. All subsequent measurements made without breaking vacuum follow the same curve. C) Annealing after re-exposure to atmosphere for 9 hours.

Figure A-2 shows the partial pressure of desorbed H_2O, H_2, CO_2, and O_2 measured as a function of temperature during a primary annealing (as in curve A of Figure A-2). While all the species begin to desorb at ~430 K, both the extent of desorption and the shape of the pressure-temperature characteristics differ significantly for each species. The observed order of the major desorption maxima is: H_2O, CO_2, and H_2. The temperature ranges in which these species desorb correlate to within ~50 K with irreversible resistance changes. Multiple desorption peaks observed for H_2O at ~503, 613 and 733 K, and for CO_2 at ~623 and 713 K are likely due to different types of adsorption sites. The simultaneous desorption of CO and CO_2 indicates the formation of intermediate moieties by surface fragmentation and reorganization. Similar areas (~6 x 10^{-5} Torr K) of desorption peaks corresponding to the various species also suggest intermediate reaction steps. The relatively high temperature (773 K) for H_2 desorption is attributed to strong adsorption, possibly due to the presence of –COOH groups on SWNT surfaces.[10,11] It was noted that O_2 desorption is negligible throughout the temperature regimes explored. The desorption spectra for H_2O, H_2, CO_2, and O_2 during a subsequent anneal, without breaking vacuum (as in curve B of Figure A-1) are shown in Figure A-3. All curves peak at ~600K, though the

heights of the peaks are almost an order of magnitude lower than for a primary anneal, indicating that the majority of the adsorbed gases are desorbed during the primary anneal.
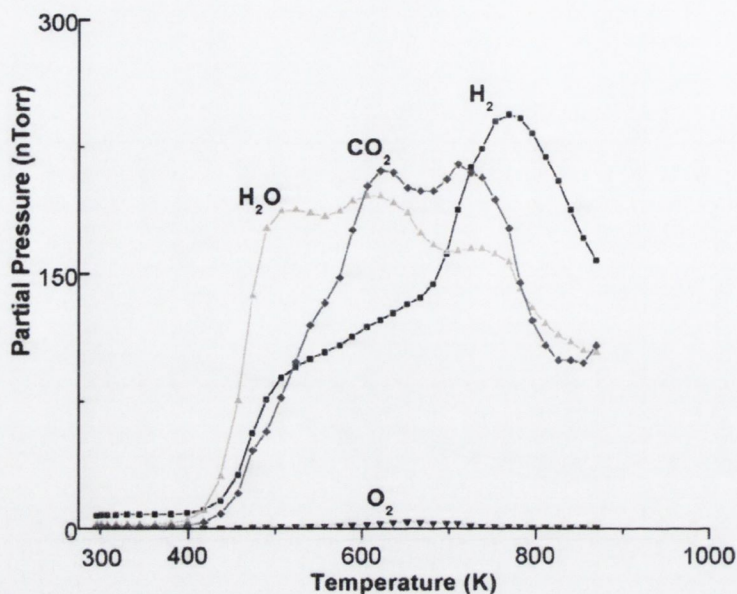

Figure A-2 Temperature dependence of partial pressures for various gases: 2 amu (H_2), 18 amu (H_2O), 32 amu (O_2), and 44 amu (CO_2) desorbed from the SWNT mat during run A of Figure A-1.

The desorption plots for the case of curve C in Figure A-1 is similar in shape to those obtained from primary anneals of as-received samples though of smaller magnitude (larger than previous subsequent anneals as in curve B of Figure A-1). Subsequent anneals without breaking vacuum after that of curve C, revert to the desorption spectra similar to those for curve B.

Annealing experiments carried out on highly oriented pyrolytic graphite (HOPG) samples reveal qualitatively similar desorption characteristics to those observed for SWNT mats, indicating that the desorption processes monitored occur at sp^2-bonded carbon sites. Figure A-4 shows the signature desorption spectra for a primary anneal of a HOPG sample.
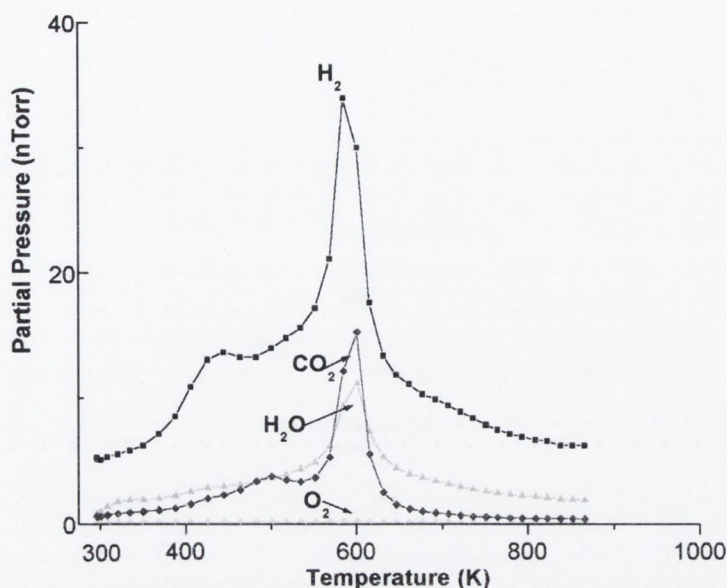
Figure A-3 Temperature dependence of partial pressures for various gases: 2 amu (H_2), 18 amu (H_2O), 32 amu (O_2), and 44 amu (CO_2) desorbed from the SWNT mat during run B of Figure A-1.
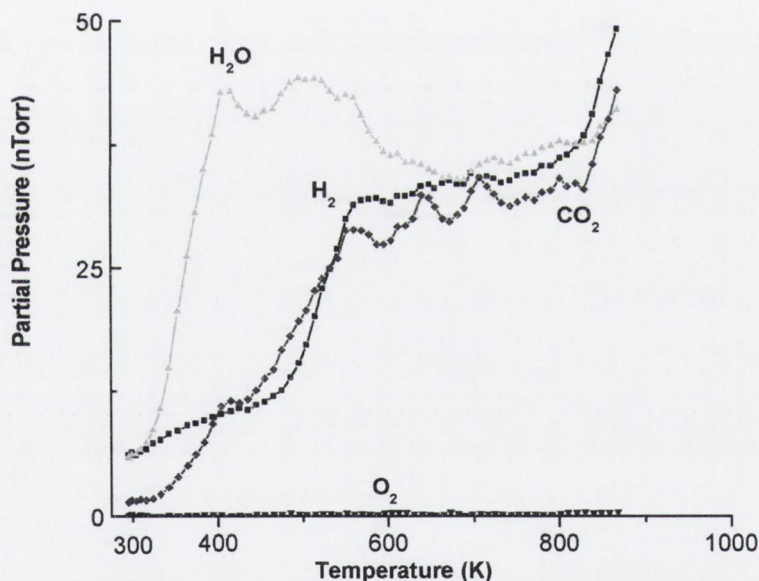
Figure A-4 Temperature dependence of partial pressures for various gases: 2 amu (H_2), 18amu (H_2O), 32 amu (O_2), and 44 amu (CO_2) desorbed from a highly ordered pyrolytic graphite (HOPG) sample during an anneal of similar conditions to that of run A in Figure A-1

The lack of observable O_2 desorption, and the relatively high temperatures of CO_2 desorption, suggest that oxygen is chemisorbed to the SWNTs. In order to determine whether or not CO_2 desorption peaks are signatures of oxygen chemisorption, desorption characteristics of a SWNT mat after exposure to ~350 Torr of N_2 (Figure A-5), and O_2 for 9 hours respectively were measured (Figure A1-6). O_2 desorption characteristics for both

A-5

annealed samples are similar, the CO_2 peak is ~2.5 times larger for those annealed after exposure to O_2.

There were only trace amounts of O_2 desorption in each case. These results not only confirm a strong chemical coupling between carbon and oxygen on the surfaces of the SWNT mats, but also indicate that oxygen incorporation is reversible.

Figure A-5 Variation of partial pressures with respect to temperature for the same set of gases mentioned above: 2 amu (H_2), 18 amu (H_2O), 32 amu (O_2), and 44 amu (CO_2) during heating to 873K in UHV after exposure to N_2 for nine hours.

In summary, the changes in electrical resistance of SWNT mats during annealing between 470 and 873 K are closely related to desorption of H_2O, CO_2, and H_2. Oxygen is strongly chemisorbed to SWNT surfaces, and desorbs primarily as CO_2. These results are significant for tailoring SWNT based nanostructures for a variety of applications like hydrogen storage, chemical sensors and molecular electronics, where the resistance-temperature interdependence and performance are intimately related.
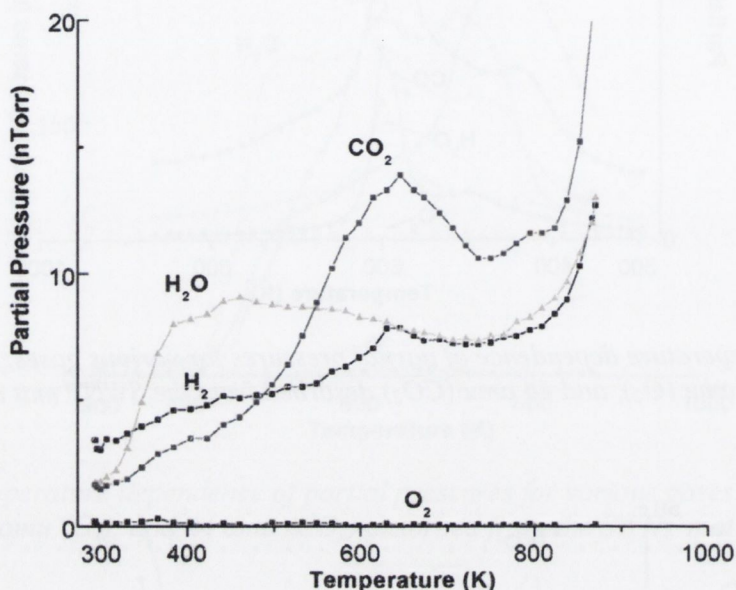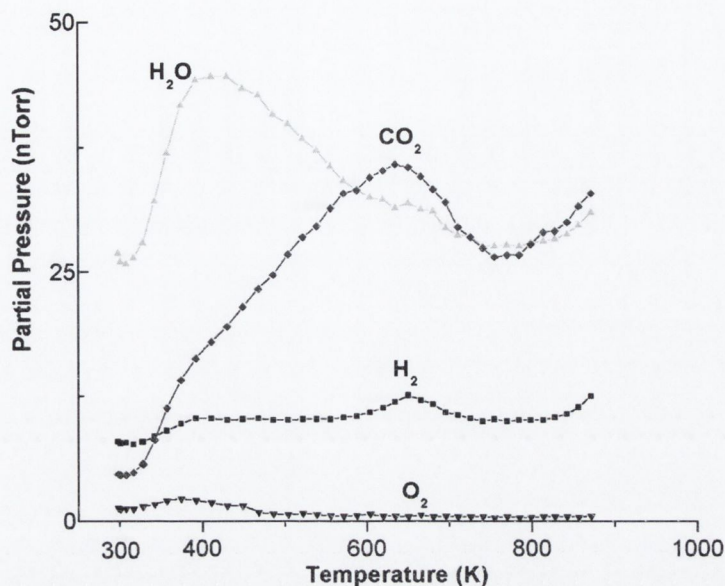
Figure A-6 Variation of partial pressures with respect to temperature for the same set of gases mentioned above: 2 amu (H_2), 18 amu (H_2O), 32 amu (O_2), and 44 amu (CO_2) during heating to 873K in UHV after exposure to O_2 for nine hours.

A.4 References

[1] R. Leahy, K. Vijayamohanan, P. M. Ajayan, G. Ramanath, and W. Blau, in *Gas desorption in single-wall carbon nanotube mats during vacuum annealing*, Galway, Ireland, 2003 (SPIE-Int. Soc. Opt. Eng), p. 783-7.

[2] R. G. Ding, G. Q. Lu, Z. F. Yan, and M. A. Wilson, Journal of Nanoscience and Nanotechnology **1,** 7-29 (2001).

[3] B. K. Pradhan, G. U. Sumanasekera, C. K. W. Adu, H. Romero, and P. C. Eklund, in *Single walled carbon nanotubes (SWNTs) as a gas sensor*, Boston, MA, 2001 (Materials Research Society), p. 14201-14206.

[4] P. G. Collins, K. Bradley, M. Ishigami, and A. Zettl, Science **287,** 1801-1804 (2000).

[5] G. U. Sumanasekera, C. K. W. Adu, S. Fang, and P. C. Eklund, Physical Review Letters **85,** 1096-1099 (2000).

[6] J. Kong, N. R. Franklin, C. Zhou, M. G. Chapline, S. Peng, K. Cho, and D. Hongjie, Science **287,** 622-625 (2000).

[7] S. Peng and K. Cho, Nanotechnology **11,** 57-60 (2000).

[8] K. Ichimura, K. Imaeda, and H. Inokuchi, Chemistry Letters, 196-197 (2000).

[9] K. Ichimura, K. Imaedab, and H. Inokuchi, Synthetic Metals **121,** 1191-1192 (2001).

[10] C. W. Jin, K. Ichimura, K. Imaeda, and H. Inokuchi, Synthetic Metals **121,** 1221-1222 (2001).

[11] K. F. Fu, W. J. Huang, Y. Lin, L. A. Riddle, D. L. Carroll, and Y. P. Sun, Nano Letters **1,** 439-441 (2001).

Appendix B Raman spectroscopy of Soy-oil/CNT composite

B.1 Raman spectroscopy

CNTs were noncovalently functionalised with chemically modified soybean oil, Acrylated epoxidized soybean oil (AESO).[1] The result was a bio-based carbon nanotube composite. Raman spectroscopy was carried out on this composite using a Horiba Jobin Yvon Labram on both 632.8 nm and 514 nm laser excitation lines.

Raman spectroscopy was used to characterise the interaction of CNTs with their environment. In Raman spectra of single walled carbon nanotube (SWNT), three prominent features can be observed: radial breathing modes (RBM), D-line and G-line, which are well documented in the literature.[2, 3] The RBM frequencies (125 – 300 cm^{-1}) can be related to nanotube diameter, and changes in the nanotube environment can be directly linked to shifts in frequency of the various RBM peaks.[4]

The RBM region in the Raman spectra of Nanocyl, HiPco SWNTs and their AESO composites using the 632.8 nm laser are shown in Figure B-1. Nanocyl SWNTs (Figure B-1 A) contain CNTs with diameters between 0.9 and 2.0 nm while the HiPco SWNTs (Figure B-1 C) have diameters ranging between 0.7 and 1.4 nm. As expected, the RBMs of the Nanocyl SWNTs are distributed over a broader frequency range than HiPco SWNT. This Raman RBM data is in excellent agreement with previous studies on HiPco[5] and Nanocyl SWNT.[6] Similar Raman feature observations were made with 514 nm laser excitation (not shown).

After low power sonication (60 W) of the HiPco/Nanocyl SWNTs with AESO for several hours, an up-shift in the RBMs to higher frequencies were recorded in the Raman

spectra of the composites (Figure B-1 B and D). The HiPco/AESO composite showed small up-shifts (1.4 – 2.6 cm^{-1}) in the RBMs compared to the larger up-shifts (3.5 – 6.4 cm^{-1}) seen for the Nanocyl/AESO composite.

The distribution of HiPco RBM peaks remains largely unchanged upon interaction with AESO (Figure B-1 A and B), suggesting that the interaction is not diameter specific within the diameter range present in the sample. The tangential feature (G-band) of HiPco/AESO increases in frequency by 5 cm^{-1}, but the full width at half maximum remains unchanged (not shown). These up-shifts would point a wrapping of the AESO around the CNTs, damping the RBMs and the radial portion of the G-band vibrations by effectively increasing the Young's modulus of the vibrations.

The frequencies of the Nanocyl RBMs also increase upon interaction with AESO (Figure B-1 C and D). The pristine SWNT peak at 190.9 cm^{-1} is upshifted by 6.4 cm^{-1}. In addition, the tangential mode (G-line at 1581 cm^{-1}) shows narrowing and an increase in frequency of 5 cm^{-1} (not shown).

The upshift in the RBM modes (6 – 9 cm^{-1}), combined with the narrowing of the G-line and the 4 cm^{-1} increase in frequency, have been previously attributed to debundling of nanotubes by conjugated polymers[7] and peptides.[5] However, it has been reported that debundling of SWNT into individual tubes will change the resonant absorption conditions of SWNT.[4] In bundled nanotubes, the energy loss due to van der Waals binding can be expected. This suggests, that for debundled nanotubes, the same laser excitation wavelength probes different nanotubes compared to bundled nanotubes. Therefore the net result of debundling is an apparent upshift in RBM using the same laser excitation.[4]

Therefore, the data suggests that AESO intercalates/coats a large percentage of nanotubes in Nanocyl bundles. Whereas, no such evidence could be found for HiPco/AESO samples, thereby suggesting that AESO coats HiPco bundles and does not intercalate. Microscopy data appears to be in agreement with these observations. TEM on Nanocyl revealed individually coated nanotubes, whereas AFM on HiPco/AESO showed larger aggregates.
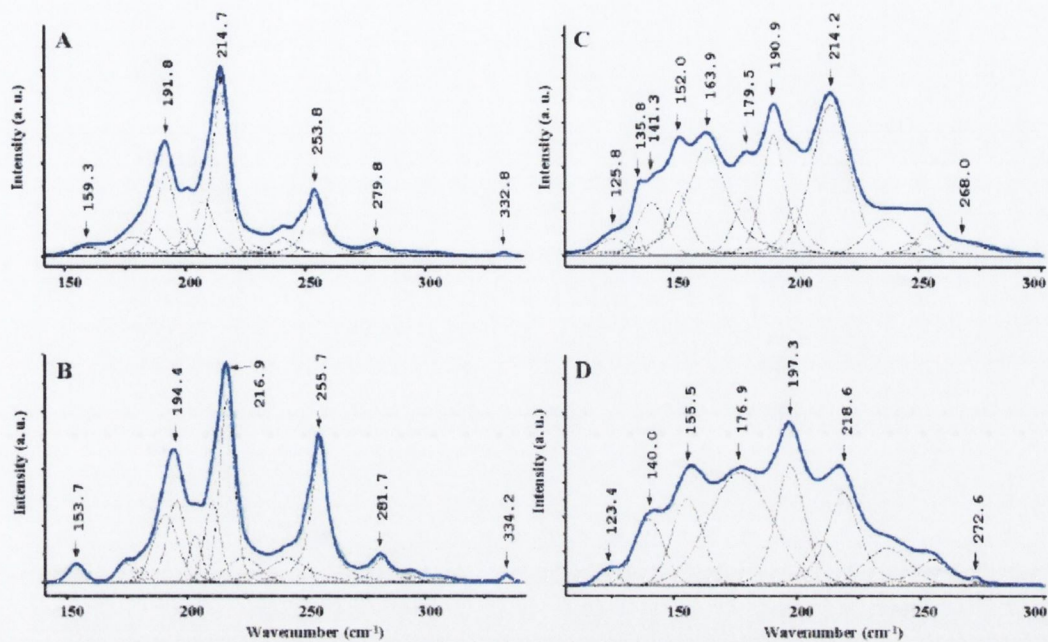
Figure B-1 Radial breathing mode (RBM) analysis of Raman spectra (633 nm excitation); (A) HiPco SWNT, (B) HiPco/AESO composite, (C) Nanocyl SWNT and (D) Nanocyl/AESO composite. The spectra were fitted by searching the minimum number of frequencies that fitted the different RBMs without fixing individual peak widths or positions. The numbers indicate the components of the RBM.

B.2 References

[1]   M. I. H. Panhuis, W. THIELEMANS , A. I. Minett, et al., International Journal of Nanoscience **2**, 185 (2003).

[2]   M. S. Dresselhaus, *Science of fullerenes and carbon nanotubes* (Academic Press, San Diego ; London 1996).

[3]   M. S. Dresselhaus, G. Dresselhaus, A. Jorio, et al., Carbon **40**, 2043 (2002).

[4]   A. M. Rao, J. Chen, E. Richter, et al., Physical Review Letters **86**, 3895 (2001).

[5]   G. R. Dieckmann, A. B. Dalton, P. A. Johnson, et al., Journal of the American Chemical Society **125**, 1770 (2003).

[6]   M. I. H. Panhuis, C. Salvador-Morales, E. Franklin, et al., Journal of Nanoscience and Nanotechnology **3**, 209 (2003).

[7]   A. B. Dalton, C. Stephan, J. N. Coleman, et al., Journal of Physical Chemistry B **104**, 10012 (2000).

Appendix C Publications list

Gas desorption in single-wall carbon nanotube mats during vacuum annealing

R Leahy, K Vijayamohanan, P M Ajayan, G Ramanath, W Blau

Proceedings of SPIE- The International Society for Optical Engineering, Galway, 2003

Controlled growth of arrays of straight and branched carbon nanotubes

Rory W. Leahy, Emer Lahiff, Andrew I. Minett, Werner J.Blau

Proceedings of SPIE- The International Society for Optical Engineering, Dublin, 2005

Chemical Vapour Deposition grown carbon nanotubes for interconnect technology

Rory W. Leahy, Emer Lahiff , Andrew I. Minett, Werner J. Blau

Submitted to Journal of Nanoscience and Nanotechnology

A composite from soy oil and carbon nanotubes

Marc in het Panhuis, Andrew I. Minett, Rory Leahy, Werner J. Blau, Baptiste Le Foulgoc, Wim Thielemans and Richard P. Wool

International Journal of Nanoscience 2 (3) 185 - 194 2003

Controlling the position and morphology of nanotubes for device fabrication

E. Lahiff, R. Leahy, A. Minett, W. Blau

AIP, Tirol, Austria, 2004

Growth of carbon nano-structures in ceramic materials

C. Kufazvinei, R. W. Leahy, S. M. Lipson, W. J. Blau, F. C. Dillon, T. R Spalding, M. A. Morris, J. D. Holmes, G. Allan, J. Patterson

Proceedings of SPIE- The International Society for Optical Engineering, Dublin, 2005

Physical properties of novel free-standing polymer-nanotube thin films

E. Lahiff, R. Leahy, J.N. Coleman, W. Blau

Carbon 44, 8 1525-1529 2006

Comparison of different methods to contact to nanowires

R. M. Langford, T.-X. Wang, M. Thornton, A. Heidelberg and J. G. Sheridan, W. Blau and R. Leahy
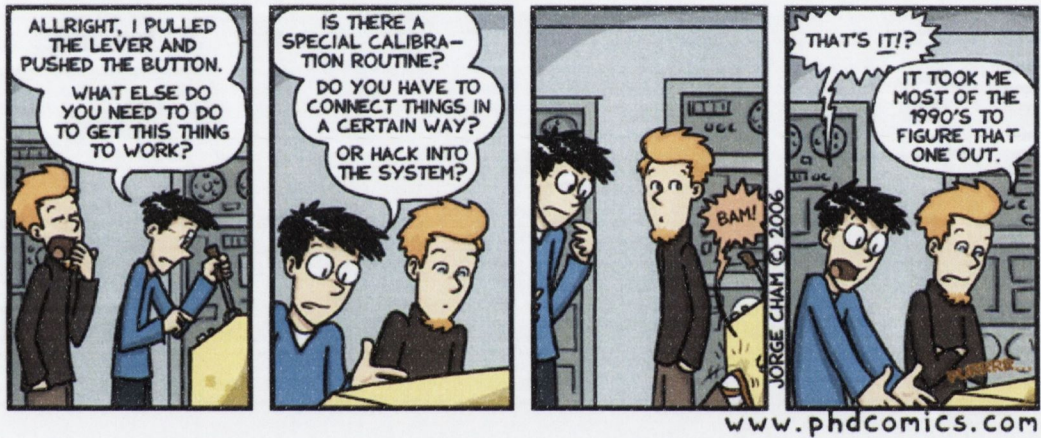
Jornal of Vacuum Science and Technology B 24 (5) 2006

"It's a trick. Get an axe."

Ash,
Army of Darkness.

"Duct tape is like the force. It has a light side, a dark side, and it holds the universe together."
- Oprah Winfrey

"In experimental science be prepared to give one week of every month away to plumbing."

Matt "Grumpy" Frederick